A thermo-mechanically-coupled large-deformation theory for amorphous polymers in a temperature range which spans their glass transition

A thermo-mechanically-coupled large-deformation theory for amorphous polymers in a temperature range which spans their glass transition

Vikas Srivastava, Shawn A. Chester, Nicoli M. Ames, and Lallit Anand*
Department of Mechanical Engineering
Massachusetts Institute of Technology
Cambridge, MA 02139, USA

July 26, 2011

Abstract

Amorphous thermoplastic polymers are important engineering materials; however, their nonlinear, strongly temperature- and rate-dependent elastic-viscoplastic behavior is still not very well understood, and is modeled by existing constitutive theories with varying degrees of success. There is no generally agreed upon theory to model the large-deformation, thermo-mechanically-coupled, elastic-viscoplastic response of these materials in a temperature range which *spans* their glass transition temperature. Such a theory is crucial for the development of a numerical capability for the simulation and design of important polymer processing operations, and also for predicting the relationship between processing methods and the subsequent mechanical properties of polymeric products. In this paper we extend our recently published theory (Anand et al., 2009, IJP 25, 1474-1494; Ames et al., 2009, IJP 25, 1495-1539) to fill this need.

We have conducted large strain compression experiments on three representative amorphous polymeric materials — a cyclo-olefin polymer (Zeonex-690R), polycarbonate (PC), and poly(methyl methacrylate) (PMMA) — in a temperature range from room temperature to approximately 50C above the glass transition temperature, ϑ_g, of each material, in a strain-rate range of $\approx 10^{-4}$ to $10^{-1}\,\mathrm{s}^{-1}$, and compressive true strains exceeding 100%. We have specialized our constitutive theory to capture the major features of the thermo-mechanical response of the three materials studied experimentally.

We have numerically implemented our thermo-mechanically-coupled constitutive theory by writing a user-material subroutine for a widely-used finite element program. In order to validate the predictive capabilities of our theory and its numerical implementation, we have performed the following validation experiments: (i) a plane-strain forging of PC at a temperature below ϑ_g, and another at a temperature above ϑ_g; (ii) blow-forming of thin-walled semi-spherical shapes of PC above ϑ_g; and (iii) microscale hot-embossing of channels in Zeonex and PMMA above ϑ_g. By comparing the results from this suite of validation experiments of some key features, such as the experimentally-measured deformed shapes and the load-displacement curves, against corresponding results from numerical simulations, we show that our theory is capable of reasonably accurately reproducing the experimental results obtained in the validation experiments.

1 Introduction

Amorphous thermoplastic polymers are important engineering materials which are widely used in a variety of applications. Over the past thirty years considerable effort has been devoted to develop constitutive models

*Corresponding author. Tel.: +1-617-253-1635; E-mail address: anand@mit.edu. A plenary talk titled "Plasticity of Amorphous Polymers: A Thermo-mechanically-Coupled Finite Deformation Theory," which forms the theoretical basis of this paper, was first given by Lallit Anand as his **Khan International Medal** lecture at the *Plasticity 2007* conference in Alaska.

to represent the large deformation elastic-viscoplastic behavior of these materials (e.g., Parks et al., 1985; Boyce et al., 1988; Govaert et al, 2000; Anand and Gurtin, 2003; Anand and Ames, 2006). These models have been primarily used to describe the *isothermal* deformation of polymers below their glass transition temperatures. In a recent pair of papers we have developed a *thermo-mechanically-coupled* large-deformation theory (Anand et al., 2009; Ames et al., 2009); however, this theory, like the others listed above, is also limited to a temperature range below the glass transition temperatures of such materials. There exists a major need to develop a thermo-mechanically-coupled theory which extends to a temperature range which includes temperatures above the glass transition temperature of these materials — a range typically $\lessapprox 50\,\mathrm{C}$ above the ϑ_g of the material, where the material response still has some "solid"-like characteristics, and is not quite yet a viscoelastic fluid. Such a theory would be useful, for example, for modeling certain important polymer processing operations, such as micro-hot-embossing for the manufacture of microfluidic devices, hot-drawing of fibers and films, and thermoforming and blow-molding for manufacture of various thin-walled containers and bottles.

Constitutive theories aimed at this class of applications have been proposed by Buckley and co-workers (e.g., Buckley and Jones, 1995; Dooling et al., 2002), as well as Boyce and co-workers (e.g., Boyce et al., 2000; Dupaix and Boyce, 2007). Guided by the work of Buckley, Boyce, and their co-workers, and our own recent papers on the mechanical behavior of polymers below ϑ_g (Anand et al., 2009; Ames et al., 2009), it is the purpose of this paper to:

1. Outline a reasonably general thermo-mechanically-coupled, large-deformation, elastic-viscoplastic theory to model the response of amorphous polymers in a temperature range which spans their glass transition temperature.

2. Specialize the new theory and apply it to model the response of three representative amorphous polymeric materials — a cyclo-olefin polymer (Zeonex-690R),[1] polycarbonate (PC), and poly(methyl methacrylate) (PMMA) — in a temperature range from room temperature to approximately $50\,\mathrm{C}$ above the glass transition temperature of each material, in a strain rate range of $\approx 10^{-4}$ to $10^{-1}\,\mathrm{s}^{-1}$, and compressive true strains exceeding 100%.

The experimental and modeling work on the response of Zeonex, PC, and PMMA reported in this paper, represents an *important extension* of our recently reported work on the response of these materials for temperatures *below* ϑ_g (Anand et al., 2009; Ames et al., 2009), to a temperature range which includes temperatures up to $\approx 50\,\mathrm{C}$ *above* the glass transition temperature. Apart from its intrinsic theoretical importance from the viewpoint of mechanics and physics of materials, we shall show that our new theory is practically useful for modeling important polymer processing operations, such as micro-hot-embossing for the manufacture of microfluidic devices, and blow-molding of thin-walled semi-spherical shapes.

The plan of the paper is as follows. In §2 we briefly describe our simple compression experiments on Zeonex, PC, and PMMA. In §3 we detail the major constitutive and field equations of our new theory, and in §4 we specialize the theory so that it is capable of reproducing the salient features of the experimentally-measured mechanical response of the amorphous polymers under study. In an Appendix, §8, we describe in reasonable detail our method to calibrate the (numerous) material parameters/functions appearing in our constitutive theory. The quality of the fit of the specialized model to the experimentally-measured stress-strain curves is discussed in §5, where we show that the model reproduces the major features of the macroscopic response of these materials in a reasonably acceptable fashion.

We have implemented our thermo-mechanically-coupled constitutive theory by writing a user material subroutine for the finite element program ABAQUS/Standard (2009). In §6, we present results of a suite of experiments that we have conducted in order to validate the predictive capabilities of our constitutive theory and its numerical implementation. By comparing the results of some key macroscopic features from this set of validation experiments, such as the experimentally-measured deformed shapes against corresponding results from numerical simulations, we show that our theory is capable of reasonably accurately reproducing the experimental results obtained in the validation experiments. We close in §7 with some final remarks.

[1] From Zeon Chemicals; henceforth, simply called Zeonex in this paper. Relative to PMMA and PC, Zeonex is biocompatible, has lower moisture uptake, has better light transmittance characteristics, and it is also chemical resistant to a wider variety of solvents. These characteristics make Zeonex an attractive material for manufacture of microfluidic devices.

2 Simple compression experiments on three amorphous polymers

Even though the mechanical behavior of polymers has been studied for a long time, comprehensive, pedigreed stress-strain data: (i) to large strains exceeding 100%, including *loading and unloading*; (ii) a variety of strain rates in the range $\approx 10^{-4}$ to 10^{-1} s^{-1}, achievable in modern servo-hydraulic testing machines; and (iii) a temperature range from room temperature to $\approx 50\,C$ above the glass transition temperature for amorphous polymers, are not readily available, and are scattered in the literature.

In this study we have generated such data by conducting compression experiments on three important amorphous polymeric materials: Zeonex, PC, and PMMA. The nominal glass transition temperatures of these three materials are:

$$\text{Zeonex-690R: } \vartheta_g \approx 136\,C, \qquad \text{PC: } \vartheta_g \approx 145\,C, \qquad \text{and} \qquad \text{PMMA: } \vartheta_g \approx 115\,C.$$

Our cylindrical compression test specimens were 12.7 mm diameter and 12.7 mm tall, and were annealed before and after machining to final shape by heating in a furnace at a temperature about 10 C above the glass transition temperature of each material, and holding at that temperature for two hours, before cooling to room temperature.[2] The experiments were conducted using a servo-hydraulic Instron testing machine, fitted with a high-temperature furnace. Amorphous polymers are poor thermal conductors; accordingly, in order to heat the compression specimens uniformly, we also used heated steel compression platens in addition to the furnace. The platens were heated with cartridge heaters, and thermocouples inserted into each platen were used to control the temperature. The top compression platen also had an integrated spherical seat to help minimize any effects of misalignment during compression testing. To reduce friction at the platen/specimen interface, the platens were polished, and thin Teflon (PTFE) films were used as lubricating layers between the specimen and the platens.[3] Before a given experiment, each specimen was allowed to anneal at the testing temperature for one hour prior to testing. The compression tests were carried out at constant *true strain-rates* to compressive true strains exceeding $\gtrapprox 100\%$; all strain measurements were made using an extensometer. The temperature and strain-rate ranges for each material were as follows:

(i) **Zeonex**: Temperature range: 25 C to 180 C. Strain-rates: 3×10^{-4}, 3×10^{-3}, 3×10^{-2}, and 3×10^{-1} s^{-1}.

(ii) **PC**: Temperature range: 25 C to 175 C. Strain-rates: 10^{-3}, 10^{-2}, and 10^{-1} s^{-1}.

(iii) **PMMA**: Temperature range: 25 C to 170 C. Strain-rates: 3×10^{-4}, 10^{-3}, 10^{-2}, and 10^{-1} s^{-1}.

Fig. 1 shows representative true stress-strain curves[4] for Zeonex at strain-rate of 3×10^{-4} s^{-1} at temperatures ranging from 25 C through 160 C, while Fig. 2 shows a more extensive set of stress-strain curves for Zeonex at strain rates of 3×10^{-4}, 3×10^{-3}, 3×10^{-2}, and 3×10^{-1} s^{-1} and temperatures of 25 C through 180 C.

Referring to Fig. 1a, that is for temperatures less than $\vartheta_g \approx 136\,C$, we see that in the glassy region:

(i) The stress-strain curves exhibit a well-defined yield-peak, followed by strain-softening, and eventual strain-hardening at large strains due to the limited extensibility of the polymer chains.

(ii) As the temperature increases in the glassy region from 25 C to 130 C, the magnitude of the yield-peak diminishes, the yield strength decreases with temperature from $\approx$ 65 MPa to $\approx$ 15 MPa, and the amount of strain-hardening observed at large strains diminishes.

(iii) Upon unloading after compression to strains exceeding 125%, approximately 5% of the strain is recovered, and there is permanent-set.

In contrast, referring to Fig. 1b, we see that above the glass transition temperature:

[2] After annealing, the PMMA and PC specimens were slowly cooled in the furnace to room temperature over a period of several hours, while the Zeonex was quenched in water.

[3] For true strains up to 100% our compression specimens showed very little or no bulging; however, for larger strain levels, in spite of our precautions to minimize friction, some bulging did occur.

[4] As is customary, in order to calculate the deformed cross-sectional area (and thence the true stress), we have assumed plastic incompressibility to estimate the stretch in the lateral direction of the compression specimens.

(i) The initial stiffness of the material has dropped dramatically.

(ii) The yield-peak has disappeared.

(iii) The stress-strain response during the loading-phase is highly non-linear and exhibits strain-hardening. However, the stress levels at large strains are below 3 MPa at 140 C, and no more than 0.5 MPa at 160 C.

(iv) Upon unloading after compression to strains exceeding 125%, the material exhibits a highly non-linear unloading response and significant permanent-set. The amount of permanent-set increases dramatically as the temperature increases from 140 C to 160 C.

Referring to Fig. 2 which shows stress-strain curves for Zeonex at various fixed temperatures and four different strain rates, we see obvious strain-rate dependent features of the material response. In the low-temperature glassy region, $\vartheta < 136\,\mathrm{C}$, the yield strength of the material increases by about 10% for a one-decade increase in strain-rate at any given temperature. Another important strain-rate dependent feature is the softening observed at large strains at the highest strain rate of 3×10^{-1} s $^{-1}$ at temperatures of 25 C, 70 C and 120 C. This softening is attributable to (near) "adiabatic" heating at the high strain rates.[5] Significant strain rate sensitivity can also be observed at temperatures above the glass transition temperature, and similar to the behavior below glass transition, the stress levels are higher for higher strain rates.

An important feature of the stress-strain behavior of amorphous polymers is their strain-rate sensitive response in a temperature range slightly above their "nominal glass transition temperature." Consider the stress-strain curves for Zeonex at 140 C in Fig. 2: at the lowest strain rate of $3\times10^{-4}\,\mathrm{s}^{-1}$ the material responds as if it were "above" its glass transition temperature, as discussed in Fig. 1b. However, at the highest strain rate of $3\times10^{-1}\,\mathrm{s}^{-1}$, the material exhibits a glassy-response with a significantly higher stress magnitude, a yield-peak, strain-softening and subsequent strain-hardening due to chain-locking. Thus, in accordance with well-known results from frequency-dependent dynamic-mechanical-tests on amorphous polymers, this result clearly shows that the "glass transition temperature" is *not a constant* for a material, and increases as the strain rate increases.

Stress-strain curves for PC and PMMA will be presented in §5, where we compare experimentally-measured stress-strain curves against those resulting from our constitutive theory. In the next section §3 we summarize our theory, and in §4 we specialize the theory for applications. In §5 we show results of the fit of the specialized constitutive theory to the experimental stress-strain data from our experiments on Zeonex, PC, and PMMA.

3 Theory

An essential kinematical ingredient of elastic-viscoplastic constitutive theories for amorphous polymers *below their glass transition temperatures*, is the classical Kröner (1960) – Lee (1969) multiplicative decomposition[6]

$$\mathbf{F} = \mathbf{F}^e\mathbf{F}^p, \qquad \text{with} \qquad \det\mathbf{F}^e > 0 \quad \text{and} \quad \det\mathbf{F}^p > 0, \tag{3.1}$$

of the deformation gradient $\mathbf{F}$ into elastic and plastic parts $\mathbf{F}^e$ and $\mathbf{F}^p$ (e.g., Boyce et al., 1988; Govaert et al, 2000; Anand and Gurtin, 2003; Anand et al., 2009). Since we wish to model the behavior of glassy polymers in the technologically important temperature range which *spans their glass transition temperatures*, and since the number of *microscopic relaxation mechanisms* in these polymers increases as the temperature is increased, we base our theory on a "multimechanism" generalization of the decomposition (3.1),

$$\mathbf{F} = \mathbf{F}^{e\,(\alpha)}\mathbf{F}^{p\,(\alpha)}, \qquad \text{with} \qquad \det\mathbf{F}^{e\,(\alpha)} > 0 \quad \text{and} \quad \det\mathbf{F}^{p\,(\alpha)} > 0, \qquad \alpha = 1,\dots,M, \tag{3.2}$$

[5] While we did not measure the actual temperature rise in our specimens, Arruda et al. (1995) have shown that the surface temperature of a compression specimen of an amorphous polymer, for a test carried out at 20 C, could increase by as much $\approx 20\,\mathrm{C}$ after a 100% compressive strain at a strain rate of 10^{-1} s^{-1}.

[6] Notation: We use standard notation of modern continuum mechanics (e.g., Gurtin, Fried, and Anand, 2009). Specifically: ∇ and Div denote the gradient and divergence with respect to the material point $\mathbf{X}$ in the reference configuration; grad and div denote these operators with respect to the point $\mathbf{x} = \boldsymbol{\chi}(\mathbf{X}, t)$ in the deformed body; a superposed dot denotes the material time-derivative. Throughout, we write $\mathbf{F}^{e-1} = (\mathbf{F}^e)^{-1}$, $\mathbf{F}^{p-\top} = (\mathbf{F}^p)^{-\top}$, etc. We write $\mathrm{tr}\,\mathbf{A}$, $\mathrm{sym}\,\mathbf{A}$, $\mathrm{skw}\,\mathbf{A}$, $\mathbf{A}_0$, and $\mathrm{sym}_0\mathbf{A}$ respectively, for the trace, symmetric, skew, deviatoric, and symmetric-deviatoric parts of a tensor $\mathbf{A}$. Also, the inner product of tensors $\mathbf{A}$ and $\mathbf{B}$ is denoted by $\mathbf{A}:\mathbf{B}$, and the magnitude of $\mathbf{A}$ by $|\mathbf{A}| = \sqrt{\mathbf{A}:\mathbf{A}}$.

where each α denotes a local micromechanism of deformation.[7] Such a multi-mechanism generalization forms the basis of the work of Buckley, Boyce, and their co-workers (e.g., Buckley and Jones, 1995; Boyce et al., 2000; Dooling et al., 2002; Dupaix and Boyce, 2007). For each micromechanism indexed by α, we refer to $\mathbf{F}^{p\,(\alpha)}$ and $\mathbf{F}^{e\,(\alpha)}$ as the *plastic and elastic parts* of $\mathbf{F}$.[8]

Restrict attention to a prescribed *material point* $\mathbf{X}$, and let $\mathbf{x}$ denote its place in the deformed configuration at a fixed time t. Then, bearing in mind that (for $\mathbf{X}$ fixed) the linear transformations $\mathbf{F}^{e\,(\alpha)}(\mathbf{X})$ and $\mathbf{F}^{p\,(\alpha)}(\mathbf{X})$ at $\mathbf{X}$ are invertible, we let

$$\mathcal{M}_{\mathbf{X}}{}^{(\alpha)} \stackrel{\text{def}}{=} \text{range of } \mathbf{F}^{p\,(\alpha)}(\mathbf{X}) = \text{domain of } \mathbf{F}^{e\,(\alpha)}(\mathbf{X}), \tag{3.3}$$

and refer to $\mathcal{M}_{\mathbf{X}}{}^{(\alpha)}$ as the *intermediate structural space* at $\mathbf{X}$ for the α-th micromechanism. Even though we use this terminology, *there is no actual physical space* that may be associated with an "intermediate structural space" — such spaces are purely mathematical constructs.

Also, it is important to note from the outset, that each $\mathbf{F}^{p\,(\alpha)}$ is to be regarded as an internal variable of the theory which is defined as a solution of the differential equation (the *flow rule* to be discussed shortly)

$$\dot{\mathbf{F}}^{p\,(\alpha)} = \mathbf{D}^{p\,(\alpha)}\mathbf{F}^{p\,(\alpha)} \quad \text{with} \quad \det \mathbf{F}^{p\,(\alpha)} = 1, \quad \text{and with initial condition} \quad \mathbf{F}^{p\,(\alpha)}(\mathbf{X}, 0) = \mathbf{1}. \tag{3.4}$$

The corresponding $\mathbf{F}^{e\,(\alpha)}$ is then defined by $\mathbf{F}^{e\,(\alpha)} \stackrel{\text{def}}{=} \mathbf{F}\mathbf{F}^{p\,(\alpha)-1}$. Hence the decompositions (3.2) are not purely kinematical in nature as they are not defined independently of constitutive equations; they are to be viewed as *kinematical constitutive equations*.

For brevity we do not give a detailed development of our theory, but only summarize the major governing constitutive and field equations. The details are easily worked out by using the kinematical decomposition (3.2) instead of (3.1), and mimicking the development of the below-ϑ_g theory detailed in Anand et al. (2009).

Our theory relates the following basic fields:

$\mathbf{x} = \boldsymbol{\chi}(\mathbf{X}, t)$,	motion;
$\mathbf{F} = \nabla\boldsymbol{\chi}, \quad J = \det \mathbf{F} > 0$,	deformation gradient;
$\mathbf{F} = \mathbf{F}^{e\,(\alpha)}\mathbf{F}^{p\,(\alpha)}, \quad \alpha = 1, \ldots, M$,	elastic-plastic decomposition of $\mathbf{F}$;
$\mathbf{F}^{e\,(\alpha)}, \quad J^{e\,(\alpha)} = \det \mathbf{F}^{e\,(\alpha)} = J > 0$,	elastic distortions;
$\mathbf{F}^{p\,(\alpha)}, \quad J^{p\,(\alpha)} = \det \mathbf{F}^{p\,(\alpha)} = 1$,	inelastic distortions;
$\mathbf{F}^{e\,(\alpha)} = \mathbf{R}^{e\,(\alpha)}\mathbf{U}^{e\,(\alpha)}$,	polar decomposition of $\mathbf{F}^{e\,(\alpha)}$;
$\mathbf{C}^{e\,(\alpha)} = \mathbf{F}^{e\,(\alpha)\top}\mathbf{F}^{e\,(\alpha)}$,	elastic right Cauchy-Green tensors;
$\mathbf{B}^{p\,(\alpha)} = \mathbf{F}^{p\,(\alpha)}\mathbf{F}^{p\,(\alpha)\top}$,	plastic left Cauchy-Green tensors;
$\mathbf{T} = \sum_\alpha \mathbf{T}^{(\alpha)}, \qquad \mathbf{T}^{(\alpha)} = \mathbf{T}^{(\alpha)\top}$,	Cauchy stress;
$\mathbf{T}_{\text{R}} = J\mathbf{T}\mathbf{F}^{-\top}$,	Piola stress;
$\psi_{\text{R}} = \sum_\alpha \bar{\psi}^{(\alpha)}$,	free energy density per unit reference volume;
$\eta_{\text{R}} = \sum_\alpha \bar{\eta}^{(\alpha)}$,	entropy density per unit reference volume;
$\vartheta > 0$,	absolute temperature;
$\nabla\vartheta$,	referential temperature gradient;
$\mathbf{q}_{\text{R}}$,	referential heat flux vector;
q_{R},	scalar heat supply.

In order to account for the major strain-hardening and softening characteristics of polymeric materials observed during viscoplastic deformation, we introduce macroscopic *internal variables* to represent important aspects of the microstructural resistance to plastic flow. Specifically, we introduce

[7] In what follows, when summing quantities over the M micro-mechanisms, we used the shorthand $\sum_\alpha \equiv \sum_{\alpha=1}^{M}$.

[8] In a one-dimensional theory of linear viscoelasticity, which is based on a widely-used mechanical analog of M Maxwell-elements assembled in parallel, the one-dimensioinal strain ϵ is decomposed as

$$\epsilon = \epsilon^{e(\alpha)} + \epsilon^{p(\alpha)}, \qquad \alpha = 1, \ldots, M;$$

the decomposition (3.2) is a three-dimensional, large-deformation, generalization of such a decomposition.

- A list of m scalar *internal state-variables*

$$\boldsymbol{\xi}^{(\alpha)} = (\xi_1^{(\alpha)}, \xi_2^{(\alpha)}, \ldots, \xi_m^{(\alpha)})$$

for each α.

- A list of *symmetric and unimodular* tensor fields

$$\mathbf{A}^{(\alpha)}(\mathbf{X}, t), \quad \mathbf{A}^{(\alpha)} = \mathbf{A}^{(\alpha)\top}, \quad \det \mathbf{A}^{(\alpha)} = 1.$$

Each such tensor field represents a dimensionless *squared stretch-like* quantity, which as a linear transformation, maps vectors in the intermediate structural space for each α, into vectors in the same space.

Further,

- we limit our attention to situations under which the material may be idealized to be *isotropic*.

3.1 Constitutive equations

1. **Free energy:**

   We assume that the free energy has the separable form

$$\psi_{\mathrm{R}} = \sum_{\alpha} \bar{\psi}^{e\,(\alpha)}(\mathcal{I}_{\mathbf{C}^{e\,(\alpha)}}, \vartheta) + \sum_{\alpha} \bar{\psi}^{p\,(\alpha)}(\mathcal{I}_{\mathbf{A}^{(\alpha)}}, \vartheta), \tag{3.5}$$

   with $\bar{\psi}^{e\,(\alpha)}$ an elastic energy, and $\bar{\psi}^{p\,(\alpha)}$ a defect energy associated with plastic flow, for each α. Also, $\mathcal{I}_{\mathbf{C}^{e\,(\alpha)}}$ and $\mathcal{I}_{\mathbf{A}^{(\alpha)}}$ represent lists of the principal invariants of $\mathbf{C}^{e\,(\alpha)}$ and $\mathbf{A}^{(\alpha)}$, respectively.

   The "defect energies" $\bar{\psi}^{p\,(\alpha)}$ associated with local microscopic plastic strain incompatibilities, and introduced via the internal variables $\mathbf{A}^{(\alpha)}$, lead to the development of important *back-stresses*, and allow one to phenomenologically account for Bauschinger-like phenomena on unloading and reverse loading. In addition, they contribute in an important manner to the plastic source term in the balance of energy.

2. **Cauchy stress:**

   The Cauchy stress in the deformed body is the sum of the contributions from each micromechanism,

$$\mathbf{T} = \sum_{\alpha} \mathbf{T}^{(\alpha)}, \tag{3.6}$$

   with

$$\mathbf{T}^{(\alpha)} \stackrel{\text{def}}{=} J^{-1} \left(\mathbf{F}^{e\,(\alpha)} \mathbf{S}^{e\,(\alpha)} \mathbf{F}^{e\,(\alpha)\top} \right), \qquad \mathbf{T}^{(\alpha)} = \mathbf{T}^{(\alpha)\top}, \tag{3.7}$$

   where

$$\mathbf{S}^{e\,(\alpha)} = 2\, \frac{\partial \bar{\psi}^{e\,(\alpha)}(\mathcal{I}_{\mathbf{C}^{e\,(\alpha)}}, \vartheta)}{\partial \mathbf{C}^{e\,(\alpha)}}\,. \tag{3.8}$$

   is a symmetric second Piola stress defined with respect to the local intermediate structural space for each α.

3. **Driving stresses for plastic flow:**

   With

$$\mathbf{M}^{e\,(\alpha)} = \mathbf{C}^{e\,(\alpha)} \mathbf{S}^{e\,(\alpha)} \tag{3.9}$$

   denoting the *symmetric* Mandel stress,

$$\mathbf{M}^{(\alpha)}_{\text{back}} = 2 \left(\frac{\partial \bar{\psi}^{p\,(\alpha)}(\mathcal{I}_{\mathbf{A}^{(\alpha)}}, \vartheta)}{\partial \mathbf{A}^{(\alpha)}}\, \mathbf{A}^{(\alpha)} \right)_0 \tag{3.10}$$

a *symmetric deviatoric* back stress, and

$$\mathbf{M}^{e\,(\alpha)}_{\text{eff}} \stackrel{\text{def}}{=} \mathbf{M}^{e\,(\alpha)} - \mathbf{M}^{(\alpha)}_{\text{back}}, \tag{3.11}$$

an *effective Mandel stress*, the driving stress for plastic flow for each α is taken as

$$(\mathbf{M}^{e\,(\alpha)}_{\text{eff}})_0 = \mathbf{M}^{e\,(\alpha)}_0 - \mathbf{M}^{(\alpha)}_{\text{back}}, \tag{3.12}$$

which is symmetric and deviatoric.

For each α, we define an *equivalent shear stress* by

$$\bar{\tau}^{(\alpha)} \stackrel{\text{def}}{=} \frac{1}{\sqrt{2}}\,|(\mathbf{M}^{e\,(\alpha)}_{\text{eff}})_0|. \tag{3.13}$$

4. **Flow rules:**

The evolution equation for each $\mathbf{F}^{p\,(\alpha)}$, with $\mathbf{W}^{p\,(\alpha)} = \mathbf{0}$,[9] is

$$\dot{\mathbf{F}}^{p\,(\alpha)} = \mathbf{D}^{p\,(\alpha)}\,\mathbf{F}^{p\,(\alpha)}, \tag{3.14}$$

with the plastic stretching given by

$$\mathbf{D}^{p\,(\alpha)} = \nu^{p\,(\alpha)}\,\Big(\frac{(\mathbf{M}^{e\,(\alpha)}_{\text{eff}})_0}{2\,\bar{\tau}^{(\alpha)}}\Big), \tag{3.15}$$

where

$$\nu^{p\,(\alpha)} \stackrel{\text{def}}{=} \sqrt{2}\,|\mathbf{D}^{p\,(\alpha)}|\,, \tag{3.16}$$

is an *equivalent plastic shear strain rate*. With

$$\mathbf{\Lambda}^{(\alpha)} = (\mathbf{C}^{e\,(\alpha)}, \mathbf{B}^{p\,(\alpha)}, \mathbf{A}^{(\alpha)}, \boldsymbol{\xi}^{(\alpha)}, \vartheta) \tag{3.17}$$

denoting a list of constitutive variables, the equivalent plastic shear strain rate $\nu^{p\,(\alpha)}$ is obtained by solving the scalar strength relation

$$\bar{\tau}^{(\alpha)} = Y^{(\alpha)}(\mathbf{\Lambda}^{(\alpha)}, \nu^{p\,(\alpha)}), \tag{3.18}$$

for given $\bar{\tau}^{(\alpha)}$ and $\mathbf{\Lambda}^{(\alpha)}$, with the strength function $Y^{(\alpha)}(\mathbf{\Lambda}^{(\alpha)}, \nu^{p\,(\alpha)})$ an isotropic function of its arguments.

5. **Evolution equations for internal variables:**

The internal variables $\boldsymbol{\xi}^{(\alpha)}$ and $\mathbf{A}^{(\alpha)}$ are presumed to evolve according to the differential equations

$$\left.\begin{aligned} \dot{\xi}^{(\alpha)}_i &= \underbrace{h^{(\alpha)}_i(\mathbf{\Lambda}^{(\alpha)})\,\nu^{p\,(\alpha)}}_{\text{dynamic evolution}} - \underbrace{\mathcal{R}^{(\alpha)}_i(\mathbf{\Lambda}^{(\alpha)})}_{\text{static recovery}}, \\ \overset{\cdot}{\overline{\mathbf{A}^{(\alpha)}}} &= \underbrace{\mathbf{D}^{p\,(\alpha)}\mathbf{A}^{(\alpha)} + \mathbf{A}^{(\alpha)}\mathbf{D}^{p\,(\alpha)} - \mathbf{G}^{(\alpha)}(\mathbf{\Lambda}^{(\alpha)})\,\nu^{p\,(\alpha)}}_{\text{dynamic evolution}} - \underbrace{\mathbf{G}^{(\alpha)}_{\text{static}}(\mathbf{\Lambda}^{(\alpha)})}_{\text{static recovery}}, \end{aligned}\right\} \tag{3.19}$$

with the functions $h^{(\alpha)}_i$, $\mathcal{R}^{(\alpha)}_i$, $\mathbf{G}^{(\alpha)}$, and $\mathbf{G}^{(\alpha)}_{\text{static}}$ isotropic functions of their arguments.

The evolution equations for $\mathbf{F}^{p\,(\alpha)}$, $\boldsymbol{\xi}^{(\alpha)}$ and $\mathbf{A}^{(\alpha)}$ need to be accompanied by initial conditions. Typical initial conditions presume that the body is initially (at time $t = 0$, say) in a **virgin state** in the sense that

$$\mathbf{F}(\mathbf{X}, 0) = \mathbf{F}^{p\,(\alpha)}(\mathbf{X}, 0) = \mathbf{A}^{(\alpha)}(\mathbf{X}, 0) = \mathbf{1}, \qquad \xi^{(\alpha)}_i(\mathbf{X}, 0) = \xi^{(\alpha)}_{i,\,0}\ (= \text{constant}), \tag{3.20}$$

[9] For a detailed discussion and justification of the $\mathbf{W}^p = \mathbf{0}$ assumption in a single micro-mechanism isotropic theory see Boyce et al. (1989) and Gurtin and Anand (2005); we adopt it here as well.

so that by $\mathbf{F} = \mathbf{F}^{e\,(\alpha)}\mathbf{F}^{p\,(\alpha)}$ we also have $\mathbf{F}^{e\,(\alpha)}(\mathbf{X}, 0) = \mathbf{1}$.

Remark 1: In the evolution equation (3.19) for the internal variables $\xi_i^{(\alpha)}$ and $\mathbf{A}^{(\alpha)}$, the terms $\mathcal{R}_i^{(\alpha)}(\mathbf{\Lambda}^{(\alpha)})$ and $\mathbf{G}^{(\alpha)}_{\text{static}}(\mathbf{\Lambda}^{(\alpha)})$ represent *static recovery* (or time recovery, or thermal recovery), since they do not depend on $\mathbf{D}^{p\,(\alpha)}$. Also, in $(3.19)_2$, the term $\mathbf{G}^{(\alpha)}(\mathbf{\Lambda}^{(\alpha)})\,\nu^{p\,(\alpha)}$ represents a *dynamic recovery* term. If both the dynamic and static recovery terms were to vanish, then we may associate each $\mathbf{A}^{(\alpha)}$ with the corresponding left Cauchy-Green tensor $\mathbf{B}^{p\,(\alpha)} = \mathbf{F}^{p\,(\alpha)}\mathbf{F}^{p\,(\alpha)\top}$, since then, for a constitutive theory with $\mathbf{W}^{p\,(\alpha)} = \mathbf{0}$,

$$\dot{\mathbf{B}}^{p(\alpha)} = \mathbf{D}^{p\,(\alpha)}\mathbf{B}^{p\,(\alpha)} + \mathbf{B}^{p\,(\alpha)}\mathbf{D}^{p\,(\alpha)}. \tag{3.21}$$

In the theory considered here, as in the classical small deformation theory of metal plasticity with non-linear kinematic-hardening (e.g., Chaboche, 2008), we allow for *recovery*, that is we allow for $\mathbf{G}^{(\alpha)}(\mathbf{\Lambda}^{(\alpha)})\,\nu^{p\,(\alpha)} \neq \mathbf{0}$ as well as $\mathbf{G}^{(\alpha)}_{\text{static}}(\mathbf{\Lambda}^{(\alpha)}) \neq \mathbf{0}$, and thus, in general, the internal variables $\mathbf{A}^{(\alpha)}$ are not the same as $\mathbf{B}^{p\,(\alpha)}$.

6. **Entropy relation. Fourier's Law:**

   Finally, we have the entropy relation

$$\eta_{\text{R}} = \sum_\alpha \eta^{(\alpha)}, \qquad \eta^{(\alpha)} = -\left[\frac{\partial \bar{\psi}^{e\,(\alpha)}(\mathcal{I}_{\mathbf{C}^{e\,(\alpha)}}, \vartheta)}{\partial \vartheta} + \frac{\partial \bar{\psi}^{p\,(\alpha)}(\mathcal{I}_{\mathbf{A}^{(\alpha)}}, \vartheta)}{\partial \vartheta}\right], \tag{3.22}$$

   together with Fourier's law

$$\mathbf{q}_{\text{R}} = -\kappa\,\nabla\vartheta, \tag{3.23}$$

   with $\kappa(\vartheta) > 0$ the thermal conductivity.

3.2 Partial differential equations for the deformation and temperature fields

The partial differential equation for the deformation is obtained from the local force balance

$$\text{Div}\,\mathbf{T}_{\text{R}} + \mathbf{b}_{0\text{R}} = \rho_{\text{R}}\,\ddot{\boldsymbol{\chi}}, \tag{3.24}$$

where $\mathbf{b}_{0\text{R}}$ is the non-inertial body force per unit volume of the reference body, $\rho_{\text{R}} > 0$ is the mass density, and

$$\mathbf{T}_{\text{R}} = J\mathbf{T}\mathbf{F}^{-\top} \tag{3.25}$$

is the standard first Piola stress, with $\mathbf{T}$ given by (3.6) through (3.8).

The specific heat in the theory is given by

$$c \overset{\text{def}}{=} -\vartheta\left[\sum_\alpha \frac{\partial^2 \bar{\psi}^{e\,(\alpha)}(\mathcal{I}_{\mathbf{C}^{e\,(\alpha)}}, \vartheta)}{\partial \vartheta^2} + \sum_\alpha \frac{\partial^2 \bar{\psi}^{p\,(\alpha)}(\mathcal{I}_{\mathbf{A}^{(\alpha)}}, \vartheta)}{\partial \vartheta^2}\right], \tag{3.26}$$

and balance of energy gives the following partial differential equation for the temperature

$$\begin{aligned} c\dot{\vartheta} = -\text{Div}\,\mathbf{q}_{\text{R}} + q_{\text{R}} + \sum_\alpha \left(\bar{\tau}^{(\alpha)} + \frac{\partial \bar{\psi}^{p\,(\alpha)}}{\partial \mathbf{A}^{(\alpha)}} : \mathbf{G}^{(\alpha)}\right)\nu^{p\,(\alpha)} + \sum_\alpha \frac{\partial \bar{\psi}^{p\,(\alpha)}}{\partial \mathbf{A}^{(\alpha)}} : \mathbf{G}^{(\alpha)}_{\text{static}} \\ + \underbrace{\vartheta \sum_\alpha \frac{\partial^2 \bar{\psi}^{e(\alpha)}}{\partial \vartheta\,\partial \mathbf{C}^{e\,(\alpha)}} : \dot{\mathbf{C}}^{e\,(\alpha)} + \vartheta \sum_\alpha \frac{\partial^2 \bar{\psi}^{p(\alpha)}}{\partial \vartheta\,\partial \mathbf{A}^{(\alpha)}} : \dot{\mathbf{A}}^{(\alpha)}}_{\text{“thermoelastic” coupling terms}}, \end{aligned} \tag{3.27}$$

with $\mathbf{q}_{\text{R}}$ given by (3.23).[10]

[10] Classically, only the term $\vartheta \sum_\alpha \frac{\partial^2 \bar{\psi}^{e(\alpha)}}{\partial \vartheta\,\partial \mathbf{C}^{e\,(\alpha)}} : \dot{\mathbf{C}}^{e\,(\alpha)}$ in (3.27) is called the "thermoelastic coupling" term. Here, for lack of better terminology, we use this terminology to also include the term $\vartheta \sum_\alpha \frac{\partial^2 \bar{\psi}^{p(\alpha)}}{\partial \vartheta\,\partial \mathbf{A}^{(\alpha)}} : \dot{\mathbf{A}}^{(\alpha)}$.

4 Specialization of the theory

The fewer the "number of micromechanisms," M, which are needed to phenomenologically describe the response of a material, then the fewer the number of "material parameters" that are needed to flesh-out the constitutive theory delineated above. In our previous study on modeling the response of amorphous polymers below ϑ_g, we found that a theory with $M = 2$ was quite adequate (Anand et al., 2009; Ames et al., 2009). In order to model the response of these materials, which extends to temperatures which are approximately 50 C above ϑ_g, we find that we need to increase the number of micromechanisms to $M = 3$. Although no real material is composed of springs and dashpots, as a visual aid, Fig. 3 shows a schematic "spring-dashpot"- representation of these three micromechanisms:

(i) **The first micromechanism ($\alpha = 1$)**: (a) The nonlinear spring represents an "elastic" resistance to intermolecular (and perhaps intramolecular) energetic bond-stretching. (b) The dashpot represents thermally-activated plastic flow due to "inelastic mechanisms," such as chain-segment rotation and relative slippage of the polymer chains between neighboring mechanical cross-linkage points. (c) The nonlinear spring in parallel with the dashpot represents an "energy storage" mechanism due to the local elastic incompatibilities caused by the viscoplastic flow mechanisms. We introduce a defect energy only for micromechanism $\alpha = 1$, via an internal variable $\mathbf{A}$; even for this micromechanism, the role of such a stored energy decreases as the molecular mobility increases when the temperatures approach and exceed ϑ_g.

(ii) **The second and third micromechanisms ($\alpha = 2, 3$)**: (a) The nonlinear springs represent resistances due to changes in the free energy upon stretching of the molecular chains between the mechanical cross-links. (b) The dashpots represent thermally-activated plastic flow due to slippage of the "mechanical" cross-links, which are relatively strong below ϑ_g, but are progressively destroyed at temperatures above ϑ_g. The fact that we employ two such mechanisms is necessitated by the experimentally-observed increased complexity of the response of amorphous polymers as the temperature transitions across the range of temperatures from below ϑ_g to sufficiently above ϑ_g. We neglect any defect energies associated with mechanisms $\alpha = 2, 3$.

Our strategy to phenomenologically model the response of the material as the temperature is increased to ϑ_g and beyond, is as follows:

- For temperatures $\vartheta < \vartheta_g$, *we do not allow any plastic flow in the dashpots associated with micromechanisms* $\alpha = 2$ and $\alpha = 3$. Thus, since the springs in $\alpha = 2$ and $\alpha = 3$ are in parallel, for all practical purposes the three-micromechanism model reduces to a simpler two-micromechanism model, which we have recently successfully used to model the response of amorphous polymers for temperatures $\vartheta < \vartheta_g$ (Anand et al., 2009; Ames et al., 2009).

  A schematic of the individual contributions from each micromechanism, to an overall stress-strain curve in compression at a temperature $\vartheta < \vartheta_g$ is shown in Fig. 4a.

- For temperatures $\vartheta > \vartheta_g$, we allow for plastic flow in the dashpots associated with micromechanisms $\alpha = 2$ and $\alpha = 3$, but *quickly drop the plastic flow resistance in mechanism* $\alpha = 2$ *to a very small value*, so that for all practical purposes in this temperature range, only mechanisms $\alpha = 1$ and $\alpha = 3$ contribute to the macroscopic stress.

  A schematic of the individual contributions from each micromechanism, to an overall stress-strain curve in compression at a temperature $\vartheta > \vartheta_g$ is shown in Fig. 4b.

Remark 2: At first blush it might appear possible to combine mechanisms $\alpha = 2$ and $\alpha = 3$ into a single micromechanism, say $\alpha = 2$, and simply make the modulus associated with the spring in this single branch to be strongly *temperature-dependent* — taking on high values below ϑ_g and low values above ϑ_g. However, this would lead to *incorrect* predictions concerning the amount of "elastic recovery" in circumstances where the polymer is first heated to a temperature above ϑ_g, subjected to a large deformation which includes large stretching of the spring, and then cooled to below ϑ_g under traction boundary conditions. Thus, since by assumption the modulus associated with spring in the single additional branch $\alpha = 2$ increases with decreasing temperature, the amount of "elastic recovery" (spring-back) upon cooling under traction

boundary conditions would be unphysically too large. Conversely, cooling under displacement boundary conditions, would result in large residual stresses.

In our discussion above, we have implicitly assumed that the glass transition temperature ϑ_g is a *constant* for each material. However, the "glass transition" actually occurs over a narrow range of temperatures, and whatever the means that are used to define *a glass transition temperature*,[11] such a glass transition temperature is not a constant, but depends strongly on the strain rate to which the material is subjected. With $\mathbf{D}_0 = \mathrm{sym}_0(\dot{\mathbf{F}}\mathbf{F}^{-1})$ denoting the total deviatoric stretching tensor, let

$$\nu \stackrel{\text{def}}{=} \sqrt{2}|\mathbf{D}_0| \tag{4.1}$$

denote an *equivalent shear strain rate*.[12] As a simple model for the variation of the glass transition temperature with strain rate, we assume that

$$\vartheta_g = \begin{cases} \vartheta_r & \text{if} \quad \nu \le \nu_r, \\ \vartheta_r + n\,\log\left(\dfrac{\nu}{\nu_r}\right) & \text{if} \quad \nu > \nu_r, \end{cases} \tag{4.2}$$

where ϑ_r a *reference glass transition temperature* at a *reference strain rate* ν_r, and n is a material parameter. The change in glass transition temperature with strain rate modeled by (4.2) is qualitatively shown in Fig. 5.

In the following subsections we present special constitutive equations for the three micromechanisms. We only present the major results of our specialization; the reader is referred to Ames et al. (2009) for the intermediate steps of continuum-mechanical arguments and derivations.

4.1 Constitutive equations for micromechanism $\alpha = 1$

1. **Free energy**

   The free energy is given by

$$\psi^{(1)} = \underbrace{\bar{\psi}^{e\,(1)}(\mathcal{I}_{\mathbf{C}^{e\,(1)}}, \vartheta)}_{\text{elastic energy}} + \underbrace{\tilde{\psi}^{p\,(1)}(\mathcal{I}_{\mathbf{A}}, \vartheta)}_{\text{defect energy}}. \tag{4.3}$$

   The elastic energy $\bar{\psi}^{e\,(1)}$:

   Let

$$\mathbf{C}^{e(1)} = \sum_{i=1}^{3} \omega_i^e\, \mathbf{r}_i^e \otimes \mathbf{r}_i^e, \quad \text{with} \quad \omega_i^e = {\lambda_i^e}^2, \tag{4.4}$$

   denote the spectral representation of $\mathbf{C}^{e(1)}$, where $(\lambda_1^e, \lambda_2^e, \lambda_3^e)$ are the positive eigenvalues of $\mathbf{U}^{e(1)}$, and $(\mathbf{r}_1^e, \mathbf{r}_2^e, \mathbf{r}_3^e)$ are the orthonormal eigenvectors of $\mathbf{C}^{e(1)}$ and $\mathbf{U}^{e(1)}$. Instead of using the invariants $\mathcal{I}_{\mathbf{C}^{e\,(1)}}$, the free energy $\bar{\psi}^{e\,(1)}$ for isotropic materials may be alternatively expressed in terms of the principal stretches, or functions thereof. With

$$\mathbf{E}^{e(1)} = \sum_{i=1}^{3} E_i^e\, \mathbf{r}_i^e \otimes \mathbf{r}_i^e, \qquad E_i^e = \ln \lambda_i^e, \tag{4.5}$$

   denoting an elastic logarithmic strain measure, we adopt the following special form for the free energy $\bar{\psi}^{e(1)}$:[13]

$$\bar{\psi}^{e\,(1)} = G|\mathbf{E}_0^{e\,(1)}|^2 + \tfrac{1}{2}K(\mathrm{tr}\,\mathbf{E}^{e(1)})^2 - 3\,K\,(\mathrm{tr}\,\mathbf{E}^{e(1)})\alpha^{\mathrm{th}}(\vartheta - \vartheta_0) + \tilde{f}(\vartheta), \tag{4.6}$$

[11] Such as the peak in the tan-δ curve in a DMA experiment.

[12] We emphasize that throughout our paper ν, ν^p etc., *do not* denote Poisson's ratios, but denote *equivalent shear strain rates*. The Poisson's ratio is explicitly denoted by ν^{poi}.

[13] This is a useful free energy function for *moderately large elastic stretches*, Anand (1979, 1986).

where $\tilde{f}(\vartheta)$ is an entropic contribution to the free energy related to the temperature-dependent specific heat of the material. The temperature-dependent parameters

$$G(\vartheta) > 0, \quad K(\vartheta) > 0, \quad \alpha^{\rm th}(\vartheta) > 0, \tag{4.7}$$

are the shear modulus, bulk modulus, and coefficient of thermal expansion, respectively, and ϑ_0 is a reference temperature.

For polymeric materials the magnitude of the elastic shear modulus G decreases drastically as the temperature increases through the glass transition temperature ϑ_g of the material. Following Dupaix and Boyce (2007), we assume that the temperature dependence of the shear modulus may be adequately approximated by the following function:

$$G(\vartheta) = \tfrac{1}{2}(G_{gl} + G_r) - \tfrac{1}{2}(G_{gl} - G_r)\tanh\Big(\frac{1}{\Delta}(\vartheta - \vartheta_g)\Big) - M(\vartheta - \vartheta_g), \tag{4.8}$$

where ϑ_g is the glass transition temperature, G_{gl} and G_r ($< G_{gl}$) are values of the shear modulus in the glassy and rubbery regions, and Δ is a parameter related to the temperature range across which the glass transition occurs. The parameter M represents the slope of the temperature variation of G beyond the transition region, with

$$M = \begin{cases} M_{gl} & \vartheta \le \vartheta_g, \\ M_r & \vartheta > \vartheta_g. \end{cases} \tag{4.9}$$

Next, the temperature dependence of Poisson's ratio $\nu^{\rm poi}$ of the material is assumed to be

$$\nu^{\rm poi}(\vartheta) = \frac{1}{2}(\nu^{\rm poi}_{gl} + \nu^{\rm poi}_{r}) - \frac{1}{2}(\nu^{\rm poi}_{gl} - \nu^{\rm poi}_{r})\tanh\Big(\frac{1}{\Delta}(\vartheta - \vartheta_g)\Big), \tag{4.10}$$

with $\nu^{\rm poi}_{gl}$ and $\nu^{\rm poi}_{r}$ representing values below and above ϑ_g, respectively. The temperature dependence of the bulk modulus K is then obtained by using the standard relation for isotropic materials

$$K(\vartheta) = G(\vartheta) \times \frac{2(1 + \nu^{\rm poi}(\vartheta))}{3(1 - 2\,\nu^{\rm poi}(\vartheta))}. \tag{4.11}$$

The temperature dependence of the shear modulus G, the Poisson's ratio $\nu_{\rm poi}$, and the bulk modulus K are schematically shown in Fig. 6.

The coefficient of thermal expansion is taken to have a bilinear temperature dependence, with the following contribution to the thermal expansion term $\alpha^{\rm th}(\vartheta - \vartheta_0)$ in the free energy relation (4.6):

$$\alpha^{\rm th}(\vartheta - \vartheta_0) = \begin{cases} \alpha_{gl}(\vartheta - \vartheta_0) & \text{if} \quad \vartheta \le \vartheta_g, \\ \alpha_{gl}(\vartheta - \vartheta_0) + (\alpha_r - \alpha_{gl})(\vartheta - \vartheta_g) & \text{if} \quad \vartheta > \vartheta_g. \end{cases} \tag{4.12}$$

The defect energy $\bar{\psi}^{p\,(1)}$:

With

$$\mathbf{A} = \sum_{i=1}^{3} a_i\, \mathbf{l}_i \otimes \mathbf{l}_i, \tag{4.13}$$

denoting the spectral representation of $\mathbf{A}$, and with

$$\ln \mathbf{A} = \sum_{i=1}^{3} \ln a_i\, \mathbf{l}_i \otimes \mathbf{l}_i, \tag{4.14}$$

denoting a defect logarithmic strain measure, we assume a free energy $\bar{\psi}^{p\,(1)}$ of the form

$$\bar{\psi}^{p\,(1)} = \frac{1}{4} B\, \left[(\ln a_1)^2 + (\ln a_2)^2 + (\ln a_3)^2\right], \tag{4.15}$$

where the positive-valued temperature-dependent parameter

$$B(\vartheta) \geq 0, \tag{4.16}$$

is a back-stress modulus. The back-stress modulus B is assumed to be a linearly decreasing function of temperature, with B vanishing above ϑ_g:

$$B(\vartheta) = \begin{cases} -X(\vartheta - \vartheta_g) & \text{if} \quad \vartheta \leq \vartheta_g, \\ 0 & \text{if} \quad \vartheta > \vartheta_g, \end{cases} \tag{4.17}$$

where $X > 0$ is a constant.

2. **Cauchy stress. Mandel stress. Back-stress. Effective stress**

Corresponding to the special free energy functions considered above, the contribution $\mathbf{T}^{(1)}$ to the Cauchy stress is given by

$$\mathbf{T}^{(1)} \stackrel{\text{def}}{=} J^{-1}\, \mathbf{R}^{e\,(1)}\, \mathbf{M}^{e(1)}\, \mathbf{R}^{e\,(1)\top}, \tag{4.18}$$

where

$$\mathbf{M}^{e(1)} = \frac{\partial \tilde{\psi}^{e\,(1)}(\mathbf{E}^{e(1)}, \vartheta)}{\partial \mathbf{E}^{e(1)}} = 2G\mathbf{E}_0^{e\,(1)} + K\,(\operatorname{tr}\mathbf{E}^{e(1)})\mathbf{1} - 3K\alpha^{\text{th}}(\vartheta - \vartheta_0)\mathbf{1}, \tag{4.19}$$

is the corresponding symmetric Mandel stress.

The symmetric and deviatoric back-stress is

$$\mathbf{M}_{\text{back}} = 2\Big(\frac{\partial \tilde{\psi}^{p\,(1)}}{\partial \mathbf{A}}\mathbf{A}\Big)_0 = B \ln \mathbf{A}. \tag{4.20}$$

Further, the driving stress for plastic flow is the effective stress given by

$$(\mathbf{M}_{\text{eff}}^{e\,(1)})_0 = \mathbf{M}_0^{e\,(1)} - \mathbf{M}_{\text{back}}. \tag{4.21}$$

The corresponding *equivalent shear stress* and *mean normal pressure* are given by

$$\bar{\tau}^{(1)} \stackrel{\text{def}}{=} \frac{1}{\sqrt{2}}\,|(\mathbf{M}_{\text{eff}}^{e\,(1)})_0|, \quad \text{and} \quad \bar{p} \stackrel{\text{def}}{=} -\frac{1}{3}\operatorname{tr}\mathbf{M}^{e(1)}, \tag{4.22}$$

respectively.

3. **Flow rule**

The evolution equation for $\mathbf{F}^{p(1)}$ is

$$\dot{\mathbf{F}}^{p\,(1)} = \mathbf{D}^{p(1)}\, \mathbf{F}^{p(1)}, \tag{4.23}$$

with $\mathbf{D}^{p(1)}$ given by

$$\mathbf{D}^{p(1)} = \nu^{p(1)} \left(\frac{(\mathbf{M}_{\text{eff}}^{e\,(1)})_0}{2\bar{\tau}^{(1)}} \right), \qquad \text{where} \qquad \nu^{p(1)} \stackrel{\text{def}}{=} \sqrt{2}|\mathbf{D}^{p(1)}|. \tag{4.24}$$

The equivalent plastic shear strain rate $\nu^{p(1)}$ is obtained by solving the scalar strength relation

$$\bar{\tau}^{(1)} = Y^{(1)}(\mathbf{\Lambda}^{(1)}, \nu^{p(1)}), \tag{4.25}$$

where

$$\mathbf{\Lambda}^{(1)} \stackrel{\text{def}}{=} \Big(\mathbf{C}^{e(1)}, \mathbf{B}^{p(1)}, \mathbf{A}, \boldsymbol{\xi}^{(1)}, \vartheta\Big) \tag{4.26}$$

denotes a list of constitutive variables. With the mean normal pressure defined by $(4.22)_2$ and a (total) *effective stretch* defined by

$$\bar{\lambda} \stackrel{\text{def}}{=} \sqrt{\operatorname{tr}\mathbf{C}/3} \equiv \sqrt{\mathbf{C}^{e(1)} : \mathbf{B}^{p\,(1)}/3}, \tag{4.27}$$

as a simplification of the theory, we assume henceforth that the strength function $Y^{(1)}$ is independent of $\mathbf{A}$, and depends on $\mathbf{C}^{e(1)}$ and $\mathbf{B}^{p(1)}$ only through $\bar{p}$ and $\bar{\lambda}$, so that

$$\bar{\tau}^{(1)} = Y^{(1)}(\bar{p}, \bar{\lambda}, \boldsymbol{\xi}^{(1)}, \vartheta, \nu^{p(1)}). \tag{4.28}$$

We assume further that at a fixed state $(\bar{p},\bar{\lambda}, \boldsymbol{\xi}^{(1)}, \vartheta)$ the strength relation (4.28) is *invertible*, with inverse

$$\nu^{p(1)} = f(\vartheta, \bar{\tau}^{(1)}, \bar{p}, \bar{\lambda}, \boldsymbol{\xi}^{(1)}) \geq 0. \tag{4.29}$$

Next, we restrict the list of the internal variables $\boldsymbol{\xi}^{(1)}$ to three positive-valued scalars,

$$\boldsymbol{\xi}^{(1)} = \Big(\varphi, S_a, S_b\Big),$$

where

- $\varphi \geq 0$ is an "order-parameter" representing the local change in molecular-packing due to deformation-induced disordering.
- $S_a \geq 0$ represents a transient resistance to plastic flow coupled to the disordering of material. The internal variables φ and S_a are introduced to model the "yield-peak" which is widely-observed in the intrinsic stress-strain response of glassy polymers.
- $S_b \geq 0$ represents a dissipative resistance to plastic flow introduced to model "isotropic hardening" at large strains as the chains are pulled taut between entanglements at large strains, and there is increasing frictional interaction between the pendant side-groups; this is in addition to any entropic or energetic contribution from network chain-stretching.

Thus, the constitutive equation for the equivalent plastic strain rate (4.29) becomes

$$\nu^{p(1)} = f(\vartheta, \bar{\tau}^{(1)}, \bar{p}, \bar{\lambda}, \varphi, S_a, S_b) \geq 0. \tag{4.30}$$

Finally, guided by the literature (e.g., Eyring, 1936; Fotheringham and Cherry, 1976, 1978; Povolo and Hermida, 1995, 1996; Richeton et al., 2005, 2006, 2007) and our own recent paper Ames et al. (2009), for the flow function f in (4.30) we choose a thermally-activated relation in the specific form

$$\nu^{p(1)} = \begin{cases} 0 & \text{if} \quad \tau_{\mathrm{e}}^{(1)} \leq 0, \\ \nu_0^{(1)} \, \exp\Big(-\dfrac{Q}{k_B\,\vartheta}\Big) \, \Big[\sinh\Big(\dfrac{\tau_{\mathrm{e}}^{(1)}\, V}{2k_B\vartheta}\Big)\Big]^{1/m^{(1)}} & \text{if} \quad \tau_{\mathrm{e}}^{(1)} > 0, \end{cases} \tag{4.31}$$

where

$$\tau_{\mathrm{e}}^{(1)} \stackrel{\mathrm{def}}{=} \bar{\tau}^{(1)} - (S_a + S_b + \alpha_p\,\bar{p}), \tag{4.32}$$

denotes a *net shear stress for thermally-activated flow*; here $\alpha_p \geq 0$ is a parameter introduced to account for the *pressure sensitivity* of plastic flow. The parameter $\nu_0^{(1)}$ is a *pre-exponential factor* with units of 1/time, Q is an *activation energy*, k_B is Boltzmann's constant, V is an activation volume, and $m^{(1)}$ is a *strain rate sensitivity parameter*. In order to model the plastic flow response of polymers over a wide range of temperatures spanning the glass transition, we take the activation energy Q *to be temperature-dependent*. We assume that it varies as

$$Q(\vartheta) = \tfrac{1}{2}(Q_{gl} + Q_r) - \tfrac{1}{2}(Q_{gl} - Q_r)\tanh\Big(\frac{1}{\Delta}(\vartheta - \vartheta_g)\Big), \tag{4.33}$$

where, $Q = Q_{gl}$ in the glassy regime, and $Q = Q_r < Q_{gl}$ in the rubbery regime, and as in (4.8), Δ is a parameter related to the temperature range across which the glass transition occurs. The variation of activation energy Q with temperature is schematically shown in Fig. 7.

Remark 3: There are many models for the rate and temperature-dependent yield strength of polymers in the literature which consider plastic flow as a thermally-activated process (e.g., Eyring, 1936;

Robertson, 1966; Argon, 1973). Most of these models give a reasonably acceptable representation of the variation of the yield strength with temperature and strain rate, but over limited ranges of these variables. The equation for the plastic shear strain rate (4.31) used here is motivated by the recent work of (Richeton et al., 2005, 2006, 2007), who in turn base their model on the so-called "cooperative"-model of Fotheringham and Cherry (1976, 1978), and Povolo and Hermida (1995, 1996). Richeton et al. have shown that a flow function of the form (4.31) may be used to satisfactorily represent the variation of the yield strength of amorphous polymers over a wide range of strain rates and temperatures. The major difference between the flow function proposed by Richeton et al. and the one considered here, is that instead of a tensorial back-stress $\mathbf{M}_{\text{back}}$ (cf., (4.20)) to define an effective stress which drives plastic flow (cf. (4.21)), they consider a temperature-dependent scalar internal stress in their theory. This results in a profound difference between their model and the one considered here, specially in the ability of the two models to capture unloading and cyclic loading phenomena, as well as in a proper accounting of the energy dissipated during plastic flow (below ϑ_g). Also, the three-dimensional theory that they present in § 3 of their 2007 paper is substantially different in its *mathematical structure* from that considered here.

4. Evolution equations for internal variables

We consider next the evolution equations for the internal variables $\boldsymbol{\xi}^{(1)} = (\varphi, S_a, S_b)$ and $\mathbf{A}$. In (3.19), the functions $\mathcal{R}_i^{(\alpha)}$ and $\mathbf{G}^{(\alpha)}_{\text{static}}$ represent *static recovery* (or time recovery, or thermal recovery), since they do not depend on the plastic strain rate. The static recovery terms are important in *long time* situations such as creep experiments over a period of hours and days at high temperatures. Here, we focus our attention on thermal forming processes that occur in relatively shorter periods of time (typically less than 5 to 20 minutes), in which case the slow static recovery effects may be neglected. Accordingly, in what follows, as a simplification, we neglect the effects of any static recovery in the evolution of the internal variables.

Evolution of φ and S_a:

The order-parameter φ and resistance S_a are introduced to model the "yield-peak" observed in amorphous polymers below the glass transition. We assume that the material disorders, and is accompanied by a microscale dilatation as plastic deformation occurs, resulting in an increase of the order-parameter φ,[14] and this increase in disorder leads to a change in the resistance S_a, causing a transient change in the flow stress of the material as plastic deformation proceeds. Accordingly, the evolution of the resistance S_a is coupled to the evolution of the order-parameter φ. Specifically, we take the evolution of S_a to be governed by[15]

$$\left.\begin{aligned} &\dot{S}_a = H_a\, \nu^{p(1)}, \qquad \text{with initial value} \qquad S_a(\mathbf{X},0) = 0, \\ &H_a = h_a\, (S_a^* - S_a)\,, \qquad \text{and} \qquad S_a^* = \hat{S}_a^*(\nu^{p(1)}, \vartheta, \varphi), \end{aligned}\right\} \tag{4.34}$$

and assume that

$$\left.\begin{aligned} &\dot{\varphi} = \beta \nu^{p(1)}, \qquad \text{with initial value} \qquad \varphi(\mathbf{X},0) = 0, \\ &\beta = g\, (\varphi^* - \varphi)\,, \qquad \text{with} \qquad \varphi^* = \hat{\varphi}^*(\nu^{p(1)}, \vartheta) \geq 0; \end{aligned}\right\} \tag{4.35}$$

here β is a *shear-induced disordering function.*

In the coupled evolution equations for S_a and φ, the parameters h_a, g, S_{a0} and φ_0 are constants (possibly temperature-dependent). The function H_a represents the strain-hardening/softening function for the resistance S_a during plastic flow: the material hardens if $S_a < S_a^*$, and softens if $S_a > S_a^*$. The critical value S_a^* of S_a controlling such hardening/softening transitions is assumed to depend on the

[14] The microscale dilatation is extremely small, and at the macroscopic level we presume the plastic flow to be incompressible.

[15] Coupled differential evolution equations of this type have previously been used to model yield peaks in granular materials (Anand and Gu, 2000), as well as amorphous polymeric materials (Anand and Gurtin, 2003; Anand et al., 2009), and amorphous metallic glasses (Henann and Anand, 2008).

current values of the plastic strain rate, temperature, and the order-parameter φ. The function S_a^*, which controls the magnitude of the stress-overshoot, is taken as

$$S_a^* = b\,(\varphi^* - \varphi)\,. \tag{4.36}$$

In the disordering function β, the parameter φ^* represents a strain-rate and temperature dependent critical value for the order-parameter: the material disorders when $\varphi < \varphi^*$, and becomes less disordered when $\varphi > \varphi^*$. Considering the temperature and strain-rate dependence of φ^*, it is expected to decrease with increasing temperature at a fixed strain-rate, and increase with strain-rate at a fixed temperature. We model this temperature and strain rate dependence of φ^* using the following phenomenological equation

$$\varphi^*(\nu^{p(1)}, \vartheta) = \begin{cases} z\left(1 - \dfrac{\vartheta}{\vartheta_g}\right)^r \left(\dfrac{\nu^{p(1)}}{\nu_r}\right)^s & \text{if} \quad (\vartheta \le \vartheta_g) \ \text{ and } \ (\nu^{p(1)} > 0), \\ 0 & \text{if} \quad (\vartheta > \vartheta_g) \ \text{ or } \ (\nu^{p(1)} = 0), \end{cases} \tag{4.37}$$

with constants (z, r, s).

Thus, gathering the number of material parameters introduced to phenomenologically model the yield-peak, we have the following list

$$\big(h_a, b, g, z, r, s\big).$$

The evolution of the order parameter φ with strain, and corresponding evolution of internal resistance S_a is schematically shown in Fig. 8a. By suitable choice of material constants, the coupled evolution equations for the internal variables φ and S_a may be used to model the "yield-peak" in the stress-strain response of glassy polymers.

Remark 4: Modeling the temperature and rate-sensitivity of the yield-peak over a wide-range of temperatures and strain rates is known to be complex. If a simpler theory with fewer material parameters is desired, and if it is deemed that modeling the yield-peak is not of interest, then there is no need to introduce the internal variables φ and S_a, and thereby also the attendant constants in their evolution equations.

Evolution of S_b:

In most of the literature on amorphous polymers, the rapid increase in stress levels at large deformations below ϑ_g has been attributed to entropic-elasticity and the limited-extensibility of the polymer chains. However, our experience with experiments that involve both loading to large strains and *subsequent unloading*, indicate that if in a corresponding theoretical model the rapid increase in stress levels during loading is attributed entirely to the limited chain-extensibility and entropic-elasticity effects, then the unloading response is incorrectly predicted — there is too much "elastic recovery" upon unloading. It is for this reason that we have introduced the internal variable S_b to model a *dissipative* resistance to plastic flow which arises at large strains as the chains are pulled taut between entanglements, and there is increasing frictional interaction between the pendant side-groups; this resistance is *in addition* to any entropic contribution from network chain-stretching.

The evolution of the internal variable S_b is taken to be governed by the differential equation

$$\dot{S}_b = h_b\,(\bar{\lambda} - 1)\,(S_b^* - S_b)\,\nu^{p(1)}, \quad \text{with initial value} \quad S_b(\mathbf{X}, 0) = 0. \tag{4.38}$$

In (4.38) the material parameters are h_b and S_b^*. We take h_b to be a temperature independent constant, while the saturation value S_b^* is taken to have the following temperature dependence

$$S_b^*(\vartheta) = \frac{1}{2}\,(S_{gl} + S_r) - \frac{1}{2}\,(S_{gl} - S_r)\tanh\Big(\frac{1}{\Delta}(\vartheta - \vartheta_g)\Big), \tag{4.39}$$

where S_{gl} and S_r $(< S_{gl})$ are values of S_b^* in the glassy and rubbery regions respectively. A schematic of the evolution of S_b with an equivalent strain in a monotonic isothermal experiment is shown in Fig. 8b.

Evolution of A:

Finally, the evolution equation for $\mathbf{A}$ is taken as

$$\dot{\mathbf{A}} = \mathbf{D}^{p\,(1)}\mathbf{A} + \mathbf{A}\mathbf{D}^{p\,(1)} - \gamma\,\mathbf{A}\,\ln\mathbf{A}\,\nu^{p\,(1)}, \qquad \mathbf{A}(\mathbf{X},0) = \mathbf{1}, \tag{4.40}$$

where $\gamma \geq 0$ is a constitutive parameter which governs the dynamic recovery of $\mathbf{A}$; we take it to be independent of temperature. This evolution equation is a generalization of the non-linear kinematic-hardening rule of the small deformation theory of classical metal viscoplasticity (e.g., Chaboche, 2008), but here, as in Ames et al. (2009), applied to large deformation polymer-viscoplasticity. Note that on account of the assumed temperature dependence of the back stress modulus B in (4.17), the back-stress $\mathbf{M}_{\rm back}$ decreases as ϑ approaches ϑ_g, and vanishes for all $\vartheta > \vartheta_g$.

4.2 Constitutive equations for micromechanism $\alpha = 2$

1. **Free energy**

Let

$$\mathbf{F}^{e\,(2)}_{\rm dis} \stackrel{\rm def}{=} J^{-1/3}\,\mathbf{F}^{e\,(2)}, \quad \det\mathbf{F}^{e\,(2)}_{\rm dis} = 1, \tag{4.41}$$

denote the distortional part of $\mathbf{F}^{e\,(2)}$. Correspondingly, let

$$\mathbf{C}^{e\,(2)}_{\rm dis} \stackrel{\rm def}{=} (\mathbf{F}^{e\,(2)}_{\rm dis})^{\top}\mathbf{F}^{e\,(2)}_{\rm dis} = J^{-2/3}\mathbf{C}^{e\,(2)}, \tag{4.42}$$

denote the distortional right Cauchy-Green tensor and consider a free energy function in the special form [16]

$$\psi^{(2)} = \bar{\psi}^{e\,(2)}(\mathbf{C}^{e\,(2)}_{\rm dis}, \vartheta). \tag{4.43}$$

As discussed by Ames et al. (2009), there is a conceptual difficulty with using statistical-mechanical ideas of the theory of entropic rubber elasticity to describe the strain hardening due to chain-stretching at temperatures below the glass transition temperature, because at these temperatures the chains do not have sufficient mobility to sample all possible molecular conformations. For this reason, we employ a simple *phenomenological* form for the free energy function $\psi^{(2)}$ proposed by Gent (1996):

$$\psi^{(2)} = -\tfrac{1}{2}\mu^{(2)}\,I^{(2)}_m\,\ln\Big(1 - \frac{I^{(2)}_1 - 3}{I^{(2)}_m}\Big), \qquad \text{with} \qquad I^{(2)}_1 \stackrel{\rm def}{=} \operatorname{tr}\mathbf{C}^{e\,(2)}_{\rm dis}, \tag{4.44}$$

where

$$\mu^{(2)}(\vartheta) > 0 \qquad \text{and} \qquad I^{(2)}_m(\vartheta) > 3 \tag{4.45}$$

are two temperature-dependent material constants, with $\mu^{(2)}$ representing the ground state rubbery shear modulus of the material, and $I^{(2)}_m$ representing maximum value of $(I^{(2)}_1 - 3)$, associated with the limited extensibility of the polymer chains.

The Gent free energy function has been shown by Boyce (1996) to yield predictions for the stress-strain response similar to the entropic-network model of Arruda and Boyce (1993). However, since the Gent free-energy function is phenomenological, we are free to specify a temperature variation of the moduli $\mu^{(2)}(\vartheta) > 0$ and $I^{(2)}_m(\vartheta)$ to fit experimentally-observed trends, rather than those dictated by statistical mechanics theories of entropic elasticity. The material parameter $\mu^{(2)}$ in (4.44) is strongly temperature dependent — experimental results indicate that $\mu^{(2)}$ *decreases* with increasing temperature. The empirical function chosen to fit the experimentally-observed temperature dependence of $\mu^{(2)}$ is

$$\mu^{(2)}(\vartheta) = \mu^{(2)}_g\,\exp\Big(-N(\vartheta - \vartheta_g)\Big), \tag{4.46}$$

[16] Since $J^{e\,(\alpha)} = J$, and we have already accounted for a volumetric elastic energy for $\psi^{(1)}$, we do not allow for a volumetric elastic energy for $\psi^{(2)}$ or $\psi^{(3)}$.

where $\mu_g^{(2)}$ is the value of $\mu^{(2)}$ at the glass transition temperature (ϑ_g), and N is a parameter that represents the slope of temperature variation on a logarithmic scale. The parameter $I_m^{(2)}$ is taken to be temperature-independent constant

$$I_m^{(2)}(\vartheta) \approx \text{constant}. \tag{4.47}$$

2. **Cauchy stress. Mandel stress**

Using (3.8), the free energy (4.44) yields the corresponding second-Piola stress as

$$\mathbf{S}^{e(2)} = J^{-2/3}\mu^{(2)}\left(1 - \frac{I_1^{(2)} - 3}{I_m^{(2)}}\right)^{-1}\left[\mathbf{1} - \frac{1}{3}\left(\operatorname{tr}\mathbf{C}_{\text{dis}}^{e\,(2)}\right)\mathbf{C}_{\text{dis}}^{e(2)\,-1}\right], \tag{4.48}$$

and use of (3.7) gives the contribution $\mathbf{T}^{(2)}$ to Cauchy stress as

$$\mathbf{T}^{(2)} = J^{-1}\left[\mu^{(2)}\left(1 - \frac{I_1^{(2)} - 3}{I_m^{(2)}}\right)^{-1}(\mathrm{B}_{\text{dis}}^{e\,(2)})_0\right]. \tag{4.49}$$

Also, from (3.9) and (4.48) the corresponding Mandel stress is

$$\mathbf{M}^{e(2)} = \mu^{(2)}\left(1 - \frac{I_1^{(2)} - 3}{I_m^{(2)}}\right)^{-1}(\mathbf{C}_{\text{dis}}^{e\,(2)})_0, \tag{4.50}$$

which gives the *equivalent shear stress* for plastic flow as

$$\bar{\tau}^{(2)} \stackrel{\text{def}}{=} \frac{1}{\sqrt{2}}\,|\mathbf{M}^{e(2)}|. \tag{4.51}$$

3. **Flow rule. Internal variables**

The evolution equation for $\mathbf{F}^{p(2)}$ is

$$\dot{\mathbf{F}}^{p\,(2)} = \mathbf{D}^{p(2)}\,\mathbf{F}^{p(2)}, \tag{4.52}$$

with the plastic stretching $\mathbf{D}^{p(2)}$ given by

$$\mathbf{D}^{p(2)} = \nu^{p(2)}\left(\frac{\mathbf{M}^{e(2)}}{2\bar{\tau}^{(2)}}\right), \qquad \text{where} \quad \nu^{p(2)} \stackrel{\text{def}}{=} \sqrt{2}|\mathbf{D}^{p(2)}| \tag{4.53}$$

is the corresponding equivalent plastic shear strain rate. For $\vartheta \geq \vartheta_g$, with $S^{(2)}$ a positive-valued stress-dimensioned (constant) shear resistance, we take the corresponding strength relation as a simple power law

$$\bar{\tau}^{(2)} = S^{(2)}\left(\frac{\nu^{p(2)}}{\nu_0^{(2)}}\right)^{m^{(2)}} \qquad \text{for} \quad \vartheta \geq \vartheta_g, \tag{4.54}$$

where $\nu_0^{(2)}$ is a reference plastic shear strain rate with units of 1/time, and $m^{(2)}$ is a positive-valued strain-rate sensitivity parameter. We assume the parameter $\nu_0^{(2)} = \nu_r$, the same as the reference rate used in (4.2). This gives

$$\nu^{p(2)} = \nu_r\left(\frac{\bar{\tau}^{(2)}}{S^{(2)}}\right)^{1/m^{(2)}} \qquad \text{for} \quad \vartheta \geq \vartheta_g. \tag{4.55}$$

In order to model no network slippage below ϑ_g, we require

$$\nu^{p(2)} = 0 \quad \text{for} \quad \vartheta < \vartheta_g. \tag{4.56}$$

We may combine (4.55) and (4.56) as the following single flow rule

$$\nu^{p\,(2)} = \frac{1}{2}\,\nu_r \left(\frac{\bar{\tau}^{(2)}}{S^{(2)}}\right)^{1/m^{(2)}} \Big[1 + \tanh\Big(\frac{1}{\Delta_x}(\vartheta - \vartheta_g)\Big)\Big]. \tag{4.57}$$

Equation (4.57) allows for no slippage of physical entanglements below ϑ_g, and as the temperature increases through the glass transition, the value of $\nu^{p\,(2)}$ smoothly transitions to a positive value. Δ_x is a parameter related to the temperature range across which the transition occurs. To ensure a very rapid transition of $\nu^{p\,(2)}$ near ϑ_g, we take

$$\Delta_x = \frac{\Delta}{10}.$$

Thus, under a macroscopically-imposed deformation history at temperatures greater than a few degrees higher than ϑ_g, micromechanism $\alpha = 2$ freely deforms inelastically by relative chain-slippage, and there is no further increase in the corresponding elastic stretch $\mathbf{U}^{e\,(2)}$, and thereby the corresponding stress; cf. Fig. 4b for $\alpha = 2$.

4.3 Constitutive equations for micromechanism $\alpha = 3$

1. **Free energy**

   Similar to our assumption for micromechanism $\alpha = 2$, we take the free energy in a Gent form:

$$\psi^{(3)} = -\tfrac{1}{2}\mu^{(3)}\, I_m^{(3)}\, \ln\Big(1 - \frac{I_1^{(3)} - 3}{I_m^{(3)}}\Big), \qquad \text{with} \qquad I_1^{(3)} \stackrel{\text{def}}{=} \operatorname{tr} \mathbf{C}_{\text{dis}}^{e\,(3)}, \tag{4.58}$$

   where

$$\mu^{(3)} > 0, \qquad \text{and} \qquad I_m^{(3)} > 3 \tag{4.59}$$

   are two material constants, with $\mu^{(3)}$ representing the ground-state rubbery shear modulus of the material, and $I_m^{(3)}$ representing maximum value of $(I_1^{(3)} - 3)$. For simplicity, these two material constants are assumed to be *temperature-independent*.

2. **Mandel stress. Cauchy stress**

   Using (3.8), the free energy (4.58) yields the corresponding second Piola stress as

$$\mathbf{S}^{e(3)} = J^{-2/3}\mu^{(3)} \left(1 - \frac{I_1^{(3)} - 3}{I_m^{(3)}}\right)^{-1} \left[\mathbf{1} - \frac{1}{3}\left(\operatorname{tr} \mathbf{C}_{\text{dis}}^{e\,(3)}\right)\mathbf{C}_{\text{dis}}^{e(3)\,-1}\right], \tag{4.60}$$

   and use of (3.7) gives the contribution $\mathbf{T}^{(3)}$ to Cauchy stress as

$$\mathbf{T}^{(3)} = J^{-1}\left[\mu^{(3)} \left(1 - \frac{I_1^{(3)} - 3}{I_m^{(3)}}\right)^{-1} (\mathrm{B}_{\text{dis}}^{e\,(3)})_0\right]. \tag{4.61}$$

   Also, from (3.9) and (4.60) the corresponding Mandel stress is

$$\mathbf{M}^{e(3)} = \mu^{(3)} \left(1 - \frac{I_1^{(3)} - 3}{I_m^{(3)}}\right)^{-1} (\mathbf{C}_{\text{dis}}^{e\,(3)})_0, \tag{4.62}$$

   which gives the *equivalent shear stress* for plastic flow for micromechanism $\alpha = 3$ as

$$\bar{\tau}^{(3)} \stackrel{\text{def}}{=} \frac{1}{\sqrt{2}}\,|\mathbf{M}^{e(3)}|. \tag{4.63}$$

3. **Flow rule. Internal variables**

The evolution equation for $\mathbf{F}^{p(3)}$ is

$$\dot{\mathbf{F}}^{p\,(3)} = \mathbf{D}^{p(3)}\,\mathbf{F}^{p(3)}, \tag{4.64}$$

with the plastic stretching $\mathbf{D}^{p(3)}$ given by

$$\mathbf{D}^{p(3)} = \nu^{p(3)}\left(\frac{\mathbf{M}^{e(3)}}{2\bar{\tau}^{(3)}}\right), \qquad \text{where} \quad \nu^{p(3)} \stackrel{\text{def}}{=} \sqrt{2}|\mathbf{D}^{p(3)}| \tag{4.65}$$

is the corresponding equivalent plastic shear strain rate. We assume that $\nu^{p(3)} = 0$ when $\vartheta < \vartheta_g$, and for $\vartheta \geq \vartheta_g$, with $S^{(3)}$ a positive-valued stress-dimensioned shear resistance, we take the corresponding strength relation as a simple power law

$$\bar{\tau}^{(3)} = S^{(3)}\left(\frac{\nu^{p(3)}}{\nu_0^{(3)}}\right)^{m^{(3)}}, \tag{4.66}$$

where $\nu_0^{(3)}$ is a reference plastic shear strain rate with units of 1/time, and $m^{(3)}$ is a positive-valued strain-rate sensitivity parameter. We assume the parameter $\nu_0^{(3)} = \nu_r$, the same as the reference rate used in (4.2). Thus, as in (4.57), the scalar flow rate may be written as

$$\nu^{p(3)} = \frac{1}{2}\,\nu_r\left(\frac{\bar{\tau}^{(3)}}{S^{(3)}}\right)^{1/m^{(3)}}\Big[1 + \tanh\Big(\frac{1}{\Delta_x}(\vartheta - \vartheta_g)\Big)\Big]. \tag{4.67}$$

4. **Evolution equations for internal variable $S^{(3)}$**

The internal variable $S^{(3)}$ models the dissipative resistance caused by the sliding polymer chains during the tortuous process of molecular disengagement that has come to be know as "reptation" at temperatures above ϑ_g. The evolution of $S^{(3)}$ is taken to be governed by

$$\dot{S}^{(3)} = h_3\,(\bar{\lambda}_{\text{dis}} - 1)\,\nu^{p(3)}, \quad \text{with initial value} \quad S^{(3)}(\mathbf{X}, 0) = S_0^{(3)} \geq 0. \tag{4.68}$$

Here $h_3(\vartheta)$ and $S_0^{(3)}(\vartheta)$ are temperature dependent material parameters, and

$$\bar{\lambda}_{\text{dis}} \stackrel{\text{def}}{=} \sqrt{\text{tr}\,\mathbf{C}_{\text{dis}}/3} = \sqrt{\text{B}^{p\,(3)} : \mathbf{C}_{\text{dis}}^{e\,(3)}/3} \tag{4.69}$$

is an effective *distortional stretch*. The temperature dependence of $S_0^{(3)}$ and h_3 is taken to obey the following simple forms

$$S_0^{(3)} = S_g^{(3)}\,\exp\Big(-Y(\vartheta - \vartheta_g)\Big), \tag{4.70}$$

$$h_3 = h_{3g}\,\exp\Big(-Z(\vartheta - \vartheta_g)\Big). \tag{4.71}$$

4.4 Fourier's Law

The heat flux is taken to be given by Fourier's law

$$\mathbf{q}_{\text{R}} = -\kappa\,\nabla\vartheta, \tag{4.72}$$

with $\kappa(\vartheta) > 0$ the thermal conductivity. The temperature dependence of the thermal conductivity for the three polymers is shown in Fig. 9a.[17]

[17]For Zeonex, the data was obtained from Zeon chemicals. For PC and PMMA, the data was obtained from the material database of the commercial software program Moldflow.

4.5 Partial differential equations for the deformation and temperature fields

The partial differential equation for the deformation is obtained from the local force balance (3.24) and (3.25), with $\mathbf{T}$ given by the sum of (4.18), (4.49) and (4.61).

At this stage of the development of the theory and the concomitant experimental database, the "thermoelastic coupling" terms in (3.27) which give rise to a temperature change due to variations of $\mathbf{C}^{e\,(\alpha)}$ and $\mathbf{A}$ are not well-characterized, nor is the dependence of the specific heat c, defined in (3.26), on these quantities. *Much work needs to be done to characterize these dependencies.* Here, as *approximations*, (i) we assume that $c \approx \hat{c}(\vartheta)$ (independent of $\mathbf{C}^{e\,(\alpha)}$ and $\mathbf{A}$), and may be obtained from experimental measurements; and (ii) we neglect the thermoelastic coupling terms, and assume instead that only a fraction $0 \lessapprox \omega \lessapprox 1$ of the rate of plastic dissipation contributes to the temperature changes. Under these approximative assumptions, and since we have neglected static recovery of $\mathbf{A}$, (3.27) reduces to

$$c\dot{\vartheta} = -\mathrm{Div}\,\mathbf{q}_{\mathrm{R}} + q_{\mathrm{R}} + \omega\,\left(\bar{\tau}^{(1)}\,\nu^{p\,(1)} + \tfrac{1}{2}\,B\,\gamma\,|\ln\mathbf{A}|^2\,\nu^{p\,(1)} + \bar{\tau}^{(2)}\,\nu^{p\,(2)} + \bar{\tau}^{(3)}\,\nu^{p\,(3)}\right). \tag{4.73}$$

We take $\omega \approx 0.7$. The temperature dependence of specific heat for the three polymers is shown in Fig. 9b.[18]

5 Material parameters for Zeonex, PC, and PMMA

The material parameters appearing in our model were calibrated by fitting the experimental stress-strain data for Zeonex, PC, and PMMA with the help of a MATLAB implementation of a one-dimensional version of our model which is detailed in the Appendix §8, as well as three-dimensional finite element simulations using a single element. Under certain circumstances, when it became necessary to account for heat generation due to plastic dissipation and thermal conduction in the simple compression experiments, fully thermo-mechanically-coupled multi-element simulations were required.[19] Our material parameter calibration procedure is described in the Appendix. The material parameters for Zeonex, PC, and PMMA determined by using this procedure are listed in Table 1.

The fit of the constitutive model to the experimental stress-strain curves for Zeonex, at various temperatures ranging from 25 C to 180 C and strain rates ranging from 3×10^{-4} to $3 \times 10^{-1}\,\mathrm{s}^{-1}$, is shown in Fig. 10. The fit of the constitutive model to our experimental stress-strain curves for PC, at various temperatures ranging from 25 C to 175 C and strain rates ranging from 10^{-3} to $10^{-1}\,\mathrm{s}^{-1}$, is shown in Fig. 11. Finally, Fig. 12 shows the fit of the constitutive model to the experimental stress-strain curves for PMMA at various temperatures ranging from 25 C to 170 C and strain rates ranging from 3×10^{-4} to $10^{-1}\,\mathrm{s}^{-1}$.

For all three amorphous polymers (Zeonex, PC, and PMMA) studied in this paper, our specialized constitutive model performs *acceptably* (but not perfectly!) in reproducing the following major features of the macroscopic stress-strain response of these materials:

- **For temperatures** $\vartheta < \vartheta_g$: (a) the strain rate and temperature dependent yield strength; (b) the transient yield-peak and strain-softening which occurs due to deformation-induced disordering; (c) the subsequent rapid strain-hardening due to alignment of the polymer chains at large strains; (d) the unloading response at large strains; and (e) the temperature rise due to plastic-dissipation and the limited time for heat-conduction for the compression experiments performed at strain rates $\gtrapprox 0.01\,\mathrm{s}^{-1}$.

- **For temperatures** $\vartheta > \vartheta_g$: (a) the extreme drop in initial stiffness at these temperatures, relative to those below ϑ_g; (b) the lack of a yield-peak; (c) the significant drop in maximum stress levels to $\lessapprox 5\,\mathrm{MPa}$, relative to $\approx 250\,\mathrm{MPa}$ at temperatures below ϑ_g; (d) the highly non-linear, strain-hardening stress-strain response during the loading-phase; (e) the non-linear unloading response and permanent-set — for Zeonex and PC the amount of permanent-set increases dramatically as the temperature increases, while for PMMA the amount of permanent-set is substantially smaller.

Overall, our model better reproduces the experimentally-observed stress-strain response for the three materials at temperatures below ϑ_g, than it does for those for temperatures above ϑ_g. However, with "only

[18] For Zeonex, data was obtained from Zeon chemicals. For PC and PMMA see Bicerano, J. (1993) and Van Krevelen, D.W. (1990).

[19] Typically to fit the experimental data at strain rates of 0.01 s^{-1} and 0.03 s^{-1}.

three micromechanisms" (but, numerous material parameters!) we feel that the model, as it stands, should be useful for modeling, simulation, and design of various polymer-processing operations, which we turn to next.

6 Validation experiments and simulations

In this section we show the results of some *validation experiments* (which were not used to determine the material parameters of our theory), and compare the results of some key macroscopic features of the experimental results against those from corresponding numerical simulations. The validation experiments include: (a) a plane-strain forging of PC at a temperature below ϑ_g, and another forging at a temperature above ϑ_g; (b) blow-forming of thin-walled semi-spherical shapes of PC above ϑ_g; and (c) micron-scale, hot-embossing of channels in Zeonex and PMMA above ϑ_g.

6.1 Plane-strain forging of PC

Plane-strain forging experiments at 25 C and 160 C, under isothermal conditions, were performed on PC specimens ($\vartheta_g \approx 145$ C). The forging operation, cf. Fig. 13, converts a cylindrical specimen with a circular cross-section into a specimen with a cross-section which is in the shape of a "cruciform." The PC forging specimens had an original diameter of 12.7 mm, and were 12.7 mm deep in the plane-strain direction, which is into the plane of the paper. The split-dies which impart the cruciform shape to the workpiece, were made from hardened tool steel. For the experiment conducted at 25 C the interfaces between the workpiece and the dies were lubricated to minimize frictional effects; however, no lubrication was used for the experiment conducted at 160 C due to degradation of the lubricant at high temperatures. The forging experiments were carried out under displacement control to a relative die-displacement of 4.6 mm at a constant die-closing velocity of 0.02 mm/s, and then the die motion was reversed at the same absolute velocity to unload the specimen. After unloading, the specimen which was forged at 160 C was immediately air-cooled to room temperature.

For the finite element simulation of the forging process we made use of the symmetry of the geometry, and only meshed one-quarter of the geometry, as shown in Fig. 14. The quarter-circle of the workpiece cross-section was meshed using 277 ABAQUS-CPE4HT thermo-mechanically coupled elements, and the cruciform-die was modeled as a rigid surface. For the experiment at 25 C the workpiece was well-lubricated, and therefore the contact between the die and the workpiece was modeled as frictionless. However, since no lubrication was applied in the experiment at 160 C, the contact between the die and the workpiece was modeled as frictional, with a high Coulomb friction coefficient of 0.75.

Fig. 15a and Fig. 15b compare the numerically-predicted and experimentally-measured, load-unload force versus displacement curves for the forging processes at 25 C and 160 C, respectively. The numerical simulations are able to reasonably accurately predict load-displacement behaviors at both 25 C, which is well below ϑ_g, as well as at 160 C, which is 15 C higher than ϑ_g of PC. Note that the maximum force for forging at 25 C is 25 kN, while the maximum force for forging at 160 C is only 0.8 kN.

At the end of the loading process, with the dies still closed, the polycarbonate specimens conform with the shape of the cruciform forging dies. Upon die retraction and unloading, the polycarbonate specimens undergo some shape-recovery. For the forging experiment conducted at 25 C there is only a little shape-recovery after unloading, while for the forging experiment conducted at 160 C there is significant shape-recovery after unloading. After unloading, and cooling down to room temperature, each forged specimen was sectioned, polished, and photographed. Fig. 16a and Fig. 16b compare the experimentally-measured and numerically-predicted deformed shapes after unloading, die removal, and cooling for the forgings conducted at 25 C and 160 C, respectively. For both cases the numerically-predicted final geometry is in reasonably good agreement with that which is experimentally-measured.

6.2 Blow-forming of semi-spherical shapes of PC

Next, we consider blow-forming of flat PC sheets into thin-walled semi-spherical shapes above ϑ_g. The starting circular blanks, 102 mm in diameter, were machined from 3 mm thick PC sheets. The blanks were clamped in a blow-forming fixture; the bottom part of the fixture was essentially a 50 mm diameter

thick-walled cylinder which was attached to a high-pressure regulated air-supply, and the top clamping plate contained a 50 mm diameter hole for the polymer to freely expand under pressure. The experiments were performed under two different processing conditions: (i) at 155 C under a forming pressure of 20 psi (0.14 MPa), and (ii) at 160 C under a pressure of 35 psi (0.24 MPa). A schematic of the temperature-pressure process cycle is shown in Fig. 17a. The forming process consists of three steps: (a) heating from room temperature to the processing-temperature over a period of 10 minutes; (b) ramping the pressure to the processing pressure in 2 minutes; (c) holding at the processing-pressure while simultaneously cooling back to room temperature in 15 minutes; and (d) finally relieving the pressure.

For the finite element simulation of such a process, we make use of the axial-symmetry of the geometry, and mesh only a slice of the geometry as shown in Fig. 17b. The polymer sheet is modeled using 252 ABAQUS-CAX4HT axi-symmetric, thermo-mechanically-coupled elements with 5 elements through the sheet thickness. The clamps are modeled as rigid surfaces, and surface-interaction between the workpiece and the clamps is modeled as frictional, with a high Coulomb friction coefficient of 0.9. The pressure was applied at the surface of the bottom elements, as indicated in Fig. 17b. Fig. 18a shows an image of a sectioned one-half of the specimen for the blow-forming experiment conducted at 155 C and 20 psi, while Fig. 18b shows the corresponding numerically-predicted result. Fig. 18c shows a comparison of the experimentally-measured profiles of the specimen cross-sections (solid lines), against corresponding numerically-predicted profiles (dashed lines): the figure at the top is for blow-forming at 160 C and 35 psi, and that at the bottom is for blow-forming at 155 C and 20 psi. The predictions of the bulged-shapes from the simulations are in good agreement with the experiments.

6.3 Micron-scale hot-embossing of Zeonex and PMMA

Of major importance for creating micron-scale surface features (such as capillary channels for microfluidic chips) in polymeric substrates is the replication method of micro-hot-embossing. The basic process of micro-hot-embossing is as follows: the polymeric substrate is heated to 10–30 C above its glass transition temperature and a rigid stamp containing micron-scale features is pressed into the heated polymer to allow the polymer to flow and fill the cavities, transferring the features in the tool to the polymeric substrate. Pressure is then held and the system is cooled to the demolding temperature (typically 20-60 C below the glass transition temperature), and the tool is removed from the polymer part. Although there are numerous reports on successfully micro-hot-embossed microfluidic chips in the literature (cf., e.g., Billenberg et al, 2005), the field of polymer hot-embossing process modeling is still not well developed because of the complex material modeling challenges, and there are only a few recent reports on numerical process-modeling studies for micro-hot-embossing (cf., e.g., Juang et al., 2002). Here we consider two micro-hot-embossing experiments and corresponding numerical simulations.

6.3.1 Embossing of a series of long micro-channels in a Zeonex substrate

As a simple example of a micro-hot-embossing experiment and simulation, we first consider embossing of a series of long channels into a Zeonex substrate ($\vartheta_g \approx 136$ C). The pattern consists of channels which are 55 μm wide, 43.5 μm deep, and are spaced 92 μm apart. Fig. 19a shows a schematic of the tool-pattern, and Fig. 19b shows a SEM micrograph of a portion of an actual embossing tool made from Zr-based metallic glass. The hot-embossing experiment was carried out on a servo-hydraulic Instron testing machine equipped with heated compression platens. A 25 mm square, 1 mm thick sheet of Zeonex, and a 11.7 mm square patterned metallic glass tool were aligned and placed between the heated compression platens. In the micro-hot-embossing experiment, the polymer and the embossing tool were brought into contact and heated to an embossing temperature 160 C. Once at the embossing temperature, a compressive embossing force was slowly ramped to 0.41 kN to produce a nominal pressure of 3 MPa in 60 seconds, and held for 60 seconds before both the tool and the polymer were cooled down over 10 minutes to the demolding temperature of 85 C, after which the pressure was removed and the tool was separated from the polymer substrate. The temperature-force-cycle for the micro-hot-embossing process is schematically shown in Fig. 20a.

Since the channels are long relative to their width, and there are a large number of them aligned in parallel, we employ a plane-strain idealization in our numerical simulation, and consider only a single half-segment with suitable boundary conditions. Fig. 20b shows the finite element mesh. The Zeonex substrate is modeled

using 742 ABAQUS-CPE4HT plane strain, thermo-mechanically-coupled elements, and the metallic glass tool is modeled using an appropriately shaped rigid surface. Contact between the substrate and tool was modeled as frictional, with a Coulomb friction coefficient of 0.75. The displacement boundary conditions on the portions AD and BC of the mesh boundary are $u_1 = 0$, while on the portion CD of the mesh, $u_1 = u_2 = 0$ are prescribed.

A scanning electron microscope (SEM) image of the embossed pattern is shown in Fig. 21a, and the numerically-predicted pattern is shown in Fig. 21b.[20] We further investigated the quality of the embossed features using an optical profilometer; Fig. 22 compares representative cross-sections of the embossed features in the Zeonex (circles), against the numerically-predicted channel profile (dashed line).[21] The final geometry of the embossed channels predicted by the numerical-simulation agrees well with the results from the micro-hot-embossing experiment.

6.3.2 Embossing of a series of long micro-channels in a PMMA substrate at various pressures

In this example we consider embossing a series of long channels into a PMMA substrate ($\vartheta_g \approx 115\,\mathrm{C}$) at an embossing temperature of 130 C, at three different embossing pressures — 0.48 MPa, 1.12 MPa, and 1.6 MPa. Three different embossing pressures of increasing magnitude were considered in order to compare the numerically-predicted and experimentally-measured partially embossed geometries.

The pattern consists of channels which are 65 μm wide, 27 μm deep, and spaced 123 μm apart. A 25 mm square, 1 mm thick sheet of PMMA, and a slightly larger patterned silicon tool were aligned and placed between the heated compression platens. In the hot-embossing experiments the tool and polymer were brought into contact and then heated to the embossing temperature of 130 C. After reaching the embossing temperature, the load was ramped to produce the desired nominal embossing pressure at a constant rate of 0.15 MPa s^{-1}. After which the polymer and tool were cooled over 10 minutes to the demolding temperature of 90 C and the pressure was removed.

For the corresponding numerical simulations, as in Section 6.3.1, we employ a plane-strain idealization and consider only a single half-segment with suitable boundary conditions. The PMMA substrate is modeled using 492 ABAQUS-CPE4HT plane-strain, thermo-mechanically-coupled elements, while the silicon tool is modeled using an appropriately shaped rigid surface. Contact between the substrate and the tool was modeled as frictional, with a Coulomb friction coefficient of 0.75. The displacement boundary conditions are prescribed similar to 6.3.1 (cf. Fig. 20b).

SEM images of the embossed channels in the PMMA at the three different embossing pressures, along with the corresponding numerical simulations are shown in Fig. 23. This result nicely shows that the numerical simualtions are able to reproduce the *process of die-filling* as the embossing pressure is increased.

6.3.3 Embossing of a micro-mixer pattern for a microfluidic device in a Zeonex substrate

Next, we turn our attention to micro-hot-embossing of a pattern with relevance to microfluidic applications, and consider a simple micro-mixer design shown in Fig. 24 (Hardt et al., 2008). The micro-mixer has two inlets which converge into a single long serpentine mixing channel with a single outlet. In addition to the serpentine micro-mixing channel, the device also has many micron-sized markers and other features for alignment and diagnostics (e.g. rectangular and triangular wells of the order of 100 μm). The mixing channel itself is 50 μm wide and 38.3 μm deep and the overall dimension of the device is 25 mm by 35 mm.

In order to determine suitable temperature and pressure process conditions for hot-embossing this micro-mixer geometry in the Zeonex substrate, we did not attempt to model the full geometry, but considered only the long parallel portions of the serpentine channels, and modeled these channels using a plane-strain idealization and periodic boundary conditions in our finite element simulations. The Zeonex substrate was modeled using a mesh consisting of 443 ABAQUS-CPE4HT plane strain, thermo-mechanically-coupled elements, and the metallic glass embossing-tool is modeled using an appropriately shaped rigid surface; the finite element mesh is shown in Fig. 25. The displacement boundary conditions on the portions AD and BC of the mesh boundary are $u_1 = 0$, while on the portion CD of the mesh, $u_1 = u_2 = 0$ are prescribed.

[20] The numerical pattern has been mirrored and repeated during post-processing to ease comparison with the corresponding experimental result.

[21] The optical profilometry method that we used to measure the channel profile is not capable of providing data for the sharp vertical features.

Contact between the substrate and tool was modeled as frictional, with Coulomb friction coefficient of 0.75. We chose an embossing temperature of 160 C, and sought to determine an appropriate embossing pressure, holding time, and demolding temperature which would result in good replication.

After a few trial simulations, we found that at 160 C, ramping the pressure to 2 MPa in 30 seconds, and holding the pressure at temperature for 60 seconds would result in a completely filled die. Fig. 26 shows two snapshots of the die-filling process: Fig. 26a shows contours of the equivalent plastic strain[22] after 10 s when the nominal pressure is 0.67 MPa and the die is only partially filled, and Fig. 26b shows the contours of equivalent plastic strain at 90 s when the pressure has been held at 2 MPa for 60 seconds and the die has completely filled. Our numerical simulations also showed that further cooling down under pressure to 85 C over a period of 10 minutes, and then demolding, would lock-in the embossed geometry.

After estimating the process conditions from our numerical simulations, we conducted an actual embossing experiment for the complete micro-mixer geometry (cf. Fig. 25) in our servo-hydraulic testing machine equipped with heated compression platens. The temperature of polymer and metallic glass tool was increased to the embossing temperature of 160 C, and a compressive force of 1.75 kN was applied to produce a *nominal* pressure of 2 MPa in 30 seconds. The pressure was then held for another 60 seconds at temperature, followed by cooling down under pressure to 85 C over a period of 10 minutes, after which the pressure was removed and the tool was quickly removed from the substrate.

SEM images of several different features in the metallic glass tool, along with the corresponding images of the embossed features in the Zeonex, are shown in Fig. 27. As seen in this figure, the micro-hot-embossing process determined from the numerical simulations, when actually executed, was able to successfully reproduce all the major micron-scale features of the metallic glass tool onto the polymeric substrate.

7 Concluding remarks

We have developed a thermo-mechanically-coupled large-deformation isotropic elastic-viscoplastic theory for amorphous polymers in a temperature range which spans their glass transition temperature. The material parameters appearing in the theory have been calibrated for Zeonex-690R, PC, and PMMA using a relatively complete set of data obtained from constant true strain-rate simple compression experiments in a temperature range from room temperature to ≈ 50 C above the glass transition temperature, for a variety of strain rates in the range $\approx 10^{-4}$ to 10^{-1} s^{-1}, achievable in modern servo-hydraulic testing machines. The new constitutive theory has been implemented in the finite element program ABAQUS/Standard (2009) by writing a user material subroutine. The predictive capabilities of the constitutive theory and its numerical implementation have been validated by comparing the results from a suite of validation experiments against corresponding results from numerical simulations. As demonstrated in this paper, our theory should be useful for modeling important polymer processing operations, such as thermoforming and blow-molding for manufacture of various thin-walled containers, and micro-hot-embossing for the manufacture of microfluidic devices.

Acknowledgements

This work was supported by the National Science Foundation under grant number DMI-0517966, and the MST program of the Singapore-MIT Alliance. We are grateful to Mr. David Henann of our Laboratory for providing the metallic-glass micro-hot-embossing dies.

References

Abaqus/Standard, 2009. SIMULIA, Providence, RI.

Ames, N. M., Srivastava, V., Chester, S. A., and Anand, L., 2009. A thermo-mechanically coupled theory for large deformations of amorphous polymers. Part II: applications. *International Journal of Plasticity* 25, 1495-1539.

[22] Defined as $\int_0^t \nu^{p(1)}(\chi) d\chi$ in branch 1.

Anand, L., 1979. On H. Hencky's approximate strain-energy function for moderate deformations. *ASME Journal of Applied Mechanics* 46, 78-82.

Anand, L., 1986. Moderate deformations in extension-torsion of incompressible isotropic elastic materials. *Journal of the Mechanics and Physics of Solids* 34, 293-304.

Anand, L., and Gu, C., 2000. Granular materials: constitutive equations and strain localization. *Journal of the Mechanics and Physics of Solids* 48, 1710-1733.

Anand, L., and Gurtin, M. E., 2003. A theory of amorphous solids undergoing large deformations, with applications to polymeric glasses. *International Journal of Solids and Structures* 40, 1465-1487.

Anand, L., and Ames, N. M., 2006. On modeling the micro-indentation response of an amorphous polymer. *International Journal of Plasticity* 22, 1123-1170.

Anand, L., Ames, N. M., Srivastava, V., and Chester, S. A., 2009. A thermo-mechanically-coupled theory for large deformations of amorphous polymers. Part I: formulation. *International Journal Plasticity* 25, 1474-1494.

Argon, A. S., 1973. A theory for the low temperature plastic deformation of glassy polymers. *Philosophical Magazine* 28, 839-865.

Arruda, E. M., Boyce, M. C., and Jayachandran, R., 1995. Effects of strain rate, temperature and thermomechanical coupling on the finite strain deformation of glassy polymers. *Mechanics of Materials* 19, 193-212.

Arruda, E. M., and Boyce, M. C., 1993. A three-dimensional constitutive model for the large stretch behavior of rubber elastic materials. *Journal of the Mechanics and Physics of Solids* 41, 389-412.

Bicerano, J., 1993. *Prediction of Polymer Properties*. Marcel Dekker Inc., New York.

Billenberg, B., Hansen, M, Johansen, D., Özkapici, V., Jeppessen, C, Szabo, P., Obieta, I. M., Arroyo, O., Tegenfeldt, J. O., and Kristensen, A., 2005. Topas-based lab-on-chip microsystems fabricated by nanoimprint lithography. *Journal of Vacuum Science and Technology B* 23, 2944-2949.

Boyce, M. C., Parks, D. M., and Argon, A. S., 1988. Large inelastic deformation of glassy polymers. Part 1: rate dependent constitutive model. *Mechanics of Materials* 7, 15-33.

Boyce, M. C., Weber, G. G., and Parks, D. M., 1989. On the kinematics of finite strain plasticity. *Journal of the Mechanics and Physics of Solids* 37, 647-665.

Boyce, M. C., 1996. Direct comparison of the Gent and the Arruda-Boyce constitutive models of rubber elasticity. *Rubber Chemistry and Technology* 69, 781-785.

Boyce, M. C., Socrate, S., and Llana, P. G., 2000. Constitutive model for the finite deformation stress-strain behavior of poly(ethylene terephthalate) above the glass transition. *Polymer* 41, 2183-2201.

Buckley, C. P., and Jones, D. C., 1995. Glass-rubber constitutive model for amorphous polymers near the glass transition. *Polymer* 36, 3301-3312.

Chaboche, J. L., 2008. A review of some plasticity and viscoplasticity constitutive theories. *International Journal of Plasticity* 24, 1642-1693.

Crist, B., 1997. Yield processes in glassy polymers. In *The Physics of Glassy Polymers* 2nd Ed. Haward, R. N., Young, R. J., Chapman & Hall, London, pp. 155-212.

Dooling, P. J., Buckley, C. P., Rostami, S., and Zahalan, N., 2002. Hot-drawing of poly(methyl methacrylate) and simulation using a glass-rubber consitutive model. *Polymer* 43, 2451-2465.

Dupaix, R. B. and Boyce, M. C., 2007. Constitutive modeling of the finite strain behavior of amorphous polymers in and above the glass transition. *Mechanics of Materials* 39, 39-52.

Eyring, H., 1936. Viscosity, plasticity, and diffusion as examples of absolute reaction rates. *Journal of Chemical Physics* 4, 283-291.

Fotheringham, D. G., and Cherry, B. W., 1976. Comment on the compression yield behaviour of polymethyl methacrylate over a wide range of temperatures and strain-rates. *Materials Science Letters* 11, 1368-1371.

Fotheringham, D. G., and Cherry, B. W., 1978. The role of recovery forces in the deformation of polyethylene. *Journal of Materials Science* 13, 951-964.

Gent, A. N., 1996. A new constitutive relation for rubber. *Rubber Chemistry and Technology* 69, 59-61.

Govert, L. E., Timmermans, P. H. M., and Brekelmans, W. A. M., 2000. The influence of intrinsic strain softening on strain localization in polycarbonate: modeling and experimental validation. *Journal of Engineering Materials and Technology* 122, 177-185.

Gurtin, M.E., and Anand, L., 2005. The decomposition $\mathbf{F} = \mathbf{F}^e\mathbf{F}^p$, material symmetry, and plastic irrotationality for solids that are isotropic-viscoplastic or amorphous. *International Journal of Plasticity* **21**, 1686-1719.

Gurtin, M.E., Fried, E., and Anand, L., 2009. *The Mechanics and Thermodynamics of Continua*, Cambridge University Press, New York (forthcoming).

Hardt, D. E., Anthony, B., and Tor, S. B., Dec. 2008. A teaching factory for polymer microfabrication - μFac. *Proceedings of the 6th International Symposium on Nano-Manufacturing*, Vouliagmeni, Athens, Greece.

Henann, D., and Anand, L., 2008. A constitutive theory for the mechanical response of amorphous metals at high temperatures spanning the glass transition temperature: application to microscale thermoplastic forming. *Acta Materialia* 56, 3290-3305.

Juang, Y. J., Lee, L. J., and Koelling, K. W., 2002. Hot embossing in microfabrication. Part II: rheological characterization and process analysis. *Polymer Engineering and Science* 42, 551-566.

Kröner, E., 1960. Allgemeine kontinuumstheorie der versetzungen und eigenspannungen. *Archive for Rational Mechanics and Analysis* 4, 273-334.

Lee, E. H., 1969. Elastic plastic deformation at finite strain. *ASME Journal of Applied Mechanics* 36, 1-6.

Parks, D. M., Argon, A. S., and Bagepalli, B., 1985. Large elastic-plastic deformation of glassy polymers. Part 1: Constitutive modelling. Report, MIT, Program in Polymer Science and Technology.

Povolo, F. and Hermida, E. B., 1995. Phenomenological description of the strain rate and temperature-dependent yield stress of PMMA. *Journal of Applied Polymer Science* 58, 55-68.

Povolo, F. and Hermida, E. B., 1996. Temperature and strain rate dependence of the tensile yield stress of PVC. *Journal of Applied Polymer Science* 61, 109-117.

Richeton, J., Ahzi, S., Daridon, L., and Rémond, Y., 2005. A formulation of the cooperative model for the yield stress of amorphous polymers for a wide range of strain rates and temperatures. *Polymer* 46, 6035-6043

Richeton, J., Ahzi, S., Vecchio, K. S., Jiang, F. C., and Adharapurapu, R. R., 2006. Influence of temperature and strain rate on the mechanical behavior of three amorphous polymers: characterization and modeling of the compressive yield stress. *International Journal of Solids and Structures* 43, 2318-2335.

Richeton, J., Ahzi, S., Vecchio, K. S., Jiang, F. C., and Makardi, A., 2007. Modeling and validation of the large deformation inelastic response of amorphous polymers over a wide range of temperatures and strain rates. *International Journal of Solids and Structures* 44, 7938-7954.

Robertson, R. E., 1966. Theory for the plasticity of glassy polymers. *Journal of Chemical Physics* 44, 3950-3956.

Van Krevelen, D. W., 1990. *Properties of Polymers*, Third ed., Elsevier, Amsterdam.

8 Appendix: Calibration of material parameters in the constitutive model

In this appendix we briefly outline our procedure for estimating values of the material parameters in the constitutive model. For an isotropic theory such as the one presented in this paper, it is most convenient to use an implementation of a one-dimensional version of our model in the computer program MATLAB to conduct appropriate simulations to estimate the material parameters. We illustrate our heuristic material parameter calibration procedure for Zeonex; the procedure for PC and PMMA is essentially identical.

From the outset we acknowledge that for any given material, the list of material parameters is rather long, and that the parameter values that we determine are *not unique*. However, having apologized for these features of our list of material parameters in advance, we know of no other theory which is able to phenomenologically (or otherwise) reproduce the complicated response of these materials over the ranges of strains, strain-rates, and temperatures considered in this paper.

8.1 One-dimensional version of the constitutive theory

In this section we present an *approximate* one-dimensional version of the model, which substantially aids in the calibration of material properties from experimental data. The approximation is primarily in that we cannot account for Poisson's-type lateral contractions, and attendant volume changes, in a one-dimensional setting. The underlying constitutive equations relate the following basic fields:

$U > 0$,		stretch,
$U = U^{e\,(\alpha)} U^{p\,(\alpha)}$,	$\alpha = 1, 2, 3$	elastic-plastic decomposition of U,
$U^{e\,(\alpha)}$		elastic part of the stretch for each α,
$U^{p\,(\alpha)}$,		plastic part of the stretch for each α,
$\vartheta > 0$,		absolute temperature,
$\psi = \sum_\alpha \psi^{\,(\alpha)}$		free energy density,
$\sigma = \sum_\alpha \sigma^{(\alpha)}$,		Cauchy stress.

8.1.1 Variation of the glass transition temperature ϑ_g with strain rate

Let

$$\dot{\epsilon} \stackrel{\text{def}}{=} |\dot{U} U^{-1}| \tag{8.1}$$

denote an *equivalent tensile strain rate*. We assume that

$$\vartheta_g = \begin{cases} \vartheta_r & \text{if} \quad \dot{\epsilon} \leq \dot{\epsilon}_r, \\ \vartheta_r + n \, \log \dfrac{\dot{\epsilon}}{\dot{\epsilon}_r} & \text{if} \quad \dot{\epsilon} > \dot{\epsilon}_r, \end{cases} \tag{8.2}$$

where ϑ_r a *reference glass transition temperature* at a *reference strain rate* $\dot{\epsilon}_r$, and n is a material parameter.

8.1.2 Constitutive equations for $\alpha = 1$

1. **Free energy. Cauchy stress. Back-stress. Effective stress**

   With

   $$\epsilon^{e\,(1)} = \ln U^{e\,(1)} \tag{8.3}$$

   denoting a logarithmic elastic strain, we assume that

   $$\psi^{(1)} = \psi^{e\,(1)}(\epsilon^{e\,(1)}, \vartheta) + \psi^{p\,(1)}(A, \vartheta), \tag{8.4}$$

   where $A > 0$, is a squared stretch-like internal variable. For $\psi^{e\,(1)}$ we use a simple linear elastic form for the free energy

   $$\psi^{e\,(1)} = \frac{1}{2} E \, (\epsilon^{e\,(1)})^2 - E \, \alpha^{\text{th}} \, (\vartheta - \vartheta_0) \epsilon^{e\,(1)} + \tilde{f}(\vartheta), \tag{8.5}$$

where $E(\vartheta) > 0$ is a Young's modulus, $\alpha^{\rm th}(\vartheta)$ is a coefficient of thermal expansion, ϑ_0 is a reference temperature, and $\tilde{f}(\vartheta)$ is an entropic contribution to the free energy related to the specific heat of the material. The temperature dependence of the modulus E is taken in the same form as that for G in (4.8), while the temperature dependence of the coefficient of thermal expansion is as in (4.12). This free energy contributes a component

$$\sigma^{(1)} = E\,\epsilon^{e\,(1)} - E\alpha^{\rm th}(\vartheta - \vartheta_0), \tag{8.6}$$

to the total Cauchy stress σ.

Next, for $\psi^{p\,(1)}$, first consider a symmetric positive definite squared-stretch-like tensor $\mathbf{A}$ which satisfies $\det \mathbf{A} = 1$. Let (a_1, a_2, a_3) denote the set of principal values of $\mathbf{A}$, with $a_1 a_2 a_3 = 1$. Then as in (4.15), the defect energy is

$$\psi^{p\,(1)} = \tfrac{1}{4}\,B\left[(\ln a_1)^2 + (\ln a_2)^2 + (\ln a_3)^2\right], \tag{8.7}$$

where $B(\vartheta) \geq 0$ is a back-stress modulus, with temperature dependence given in (4.17). With $\boldsymbol{\sigma}^{(\rm back)}$ denoting a stress from this free energy, standard relations of finite deformation incompressible elasticity give the corresponding principal values of the back-stress as

$$\sigma_i^{(\rm back)} = 2a_i \frac{\partial \psi^{p\,(1)}}{\partial a_i} - P, \tag{8.8}$$

with P an arbitrary "pressure." In simple tension/compression, $\sigma_1^{(\rm back)} \equiv \sigma_{\rm back}$ and $\sigma_2^{(\rm back)} = \sigma_3^{(\rm back)} = 0$, and hence

$$\sigma_{\rm back} = 2a_1 \frac{\partial \psi^{p\,(1)}}{\partial a_1} - 2a_2 \frac{\partial \psi^{p\,(1)}}{\partial a_2} = B\left(\ln a_1 - \ln a_2\right), \tag{8.9}$$

or equivalently, with $a_1 = A$, and $a_2 = a_3 = A^{-1/2}$,

$$\sigma_{\rm back} = \frac{3}{2} B \ln A. \tag{8.10}$$

In a one-dimensional setting, the driving stress for plastic flow is the effective stress given by

$$\sigma_{\rm eff}^{(1)} = \sigma^{(1)} - \sigma_{\rm back}, \tag{8.11}$$

and the *equivalent tensile stress* and the *mean normal pressure* are

$$\bar{\sigma}^{(1)} \stackrel{\rm def}{=} |\sigma_{\rm eff}^{(1)}| \qquad \text{and} \qquad \bar{p} = -\frac{1}{3}\sigma^{(1)}, \tag{8.12}$$

respectively.

2. **Flow rule**

The one-dimensional version of the flow rule (4.24) is that

$$\dot{U}^{p\,(1)} = D^{p\,(1)} U^{p\,(1)}, \qquad D^{p\,(1)} = \dot{\epsilon}^{p(1)} \text{sign}(\sigma^{(1)}), \qquad \text{with} \qquad \dot{\epsilon}^{p(1)} \geq 0. \tag{8.13}$$

With (S_a, S_b) two positive-valued stress-dimensioned internal variables, and α_p a pressure-sensitivity parameter, let

$$\sigma_e \stackrel{\rm def}{=} \bar{\sigma}^{(1)} - (S_a + S_b + \alpha_p \bar{p}) \tag{8.14}$$

define a net equivalent tensile stress, then equivalent tensile plastic strain rate $\dot{\epsilon}^{p(1)}$ is taken to be given by

$$\dot{\epsilon}^{p(1)} = \begin{cases} 0 & \text{if} \quad \sigma_e \leq 0, \\ \dot{\epsilon}_0^{(1)} \exp\left(-\dfrac{Q}{k_B \vartheta}\right) \left[\sinh\left(\dfrac{\sigma_e V}{2\,k_B \vartheta}\right)\right]^{1/m^{(1)}} & \text{if} \quad \sigma_e > 0. \end{cases} \tag{8.15}$$

In the scalar flow rule (8.15), $(\dot\epsilon_0^{(1)}, V, m^{(1)}, \alpha_p)$ are taken to be constants, while Q is assumed to be temperature- dependent, with the dependency given in (4.33). When $\dot\epsilon^{p(1)} > 0$, the scalar flow rule (8.15), using (8.11) and (8.12), may be inverted to give the strength relation

$$|\sigma^{(1)} - \sigma_{\rm back}| + \frac{1}{3}\alpha_p\,\sigma^{(1)} = S_a + S_b + \frac{2k_b\vartheta}{V}\sinh^{-1}\left[\left(\frac{\dot\epsilon^{p(1)}}{\dot\epsilon^*(\vartheta)}\right)^{m^{(1)}}\right], \tag{8.16}$$

where

$$\dot\epsilon^*(\vartheta) \stackrel{\rm def}{=} \dot\epsilon_0^{(1)}\,\exp\left(-\frac{Q}{k_B\vartheta}\right). \tag{8.17}$$

3. **Evolution equations for the internal variables φ, S_a, S_b, and A**

Together with (S_a, S_b, A), we introduce another internal variable φ. The internal variables S_a and φ are taken to obey the coupled evolution equations:

$$\dot S_a = h_a\,(S_a^* - S_a)\,\dot\epsilon^{p(1)}, \quad \text{with} \quad S_a^* = b\,(\varphi^* - \varphi)\,, \quad \text{and} \quad S_a(0) = 0; \tag{8.18}$$

where

$$\left.\begin{aligned} &\dot\varphi = g\,(\varphi^* - \varphi)\,\dot\epsilon^{p(1)}, \qquad \text{with} \qquad \varphi(0) = 0, \qquad \text{where} \\ &\varphi^*(\dot\epsilon^{p(1)}, \vartheta) = \begin{cases} z\left(1 - \dfrac{\vartheta}{\vartheta_g}\right)^r \left(\dfrac{\dot\epsilon^{p(1)}}{\dot\epsilon_r}\right)^s & \text{for} \quad (\vartheta \le \vartheta_g) \ \text{ and } \ (\dot\epsilon^{p(1)} > 0), \\ 0 & \text{for} \quad (\vartheta > \vartheta_g) \ \text{ or } \ (\dot\epsilon^{p(1)} = 0). \end{cases} \end{aligned}\right\} \tag{8.19}$$

Here (h_a, b, g, z, r, s) are taken to be constants.

The evolution of S_b is taken to be governed by

$$\dot S_b = h_b\,(\bar\lambda - 1)\,(S_b^* - S_b)\,\dot\epsilon^{p(1)}, \quad \text{with initial value} \quad S_b(0) = S_{b0} \ge 0, \tag{8.20}$$

where

$$\bar\lambda \stackrel{\rm def}{=} \sqrt{(U + 2U)/3} \tag{8.21}$$

is an effective stretch, h_b a constant, and S_b^* temperature-dependent, cf. (4.38).

The one-dimensional form of (4.40) is the following evolution equation for A:

$$\dot A = 2\,A\,D^{p\,(1)} - \gamma(A\ln A)\,\dot\epsilon^{p(1)}, \qquad A(0) = 1, \tag{8.22}$$

where $\gamma \ge 0$ is a constitutive parameter which governs the dynamic recovery of A.

8.1.3 Constitutive equations for $\alpha = 2$

1. **Free energy. Cauchy stress**

For ease of notation, suppress for the time being the superscript $\alpha = 2$. For ψ, consider first a symmetric positive definite, unimodular stretch tensor $\mathbf{U}^e$. Let (U_1^e, U_2^e, U_3^e) denote the set of principal stretches of $\mathbf{U}^e$, with $U_1^e U_2^e U_3^e = 1$. The first invariant I_1 of $(\mathbf{U}^e)^2$ is

$$I_1 \stackrel{\rm def}{=} U_1^{e\,2} + U_2^{e\,2} + U_3^{e\,2}. \tag{8.23}$$

With $\boldsymbol{\sigma}$ denoting the contribution to the Cauchy stress from free energy ψ, which is presumed to be a function of I_1, standard relations of finite-deformation incompressible elasticity give the principal values of $\boldsymbol{\sigma}$ as

$$\sigma_i = U_i^e\frac{\partial\psi}{\partial U_i^e} - P, \tag{8.24}$$

with P an arbitrary "pressure." In simple tension/compression, with $\sigma_1 \equiv \sigma$ and $\sigma_2 = \sigma_3 = 0$, we get

$$\sigma = U_1^e\frac{\partial\psi}{\partial U_1^e} - U_2^e\frac{\partial\psi}{\partial U_2^e} = \frac{\partial\psi}{\partial I_1}\left(U_1^e\frac{\partial I_1}{\partial U_1^e} - U_2^e\frac{\partial I_1}{\partial U_2^e}\right) = 2\,\frac{\partial\psi}{\partial I_1}\,\left(U_1^{e\,2} - U_2^{e\,2}\right), \tag{8.25}$$

or equivalently, with $U_1^e \equiv U^e$ and $U_2^e = U_3^e = U^{e\,-1/2}$,

$$\sigma = 2\,\frac{\partial \psi}{\partial I_1}\,\left(U^{e\,2} - U^{e\,-1}\right). \tag{8.26}$$

Reinstating the superscript (2) for micromechanism $\alpha = 2$, the Gent (1996) free energy in terms of $I_1^{(2)} \stackrel{\text{def}}{=} \left(U_1^{e(2)}\right)^2 + \left(U_2^{e(2)}\right)^2 + \left(U_3^{e(2)}\right)^2$ is

$$\psi^{(2)} = -\frac{1}{2}\,\mu^{(2)}\,I_m^{(2)}\,\ln\left(1 - \frac{I_1^{(2)} - 3}{I_m^{(2)}}\right), \tag{8.27}$$

which with (8.26) gives the contribution $\sigma^{(2)}$ to total one-dimensional Cauchy stress σ as

$$\sigma^{(2)} = \mu^{(2)}\left(1 - \frac{I_1^{(2)} - 3}{I_m^{(2)}}\right)^{-1}\left(\left(U^{e(2)}\right)^2 - \left(U^{e(2)}\right)^{-1}\right), \tag{8.28}$$

where $\mu^{(2)}(\vartheta) > 0$ and $I_m^{(2)} > 3$ are two material parameters, with the temperature dependency of $\mu^{(2)}$ given in (4.46).

2. **Flow rule**

The evolution equation for $U^{p\,(2)}$ is

$$\left.\begin{aligned} \dot{U}^{p\,(2)} &= D^{p\,(2)}U^{p\,(2)}, \qquad D^{p\,(2)} = \dot{\epsilon}^{p(2)}\text{sign}(\sigma^{(2)}), \\ \dot{\epsilon}^{p(2)} &= \frac{1}{2}\dot{\epsilon}_r\Big(\frac{|\sigma^{(2)}|}{S^{(2)}}\Big)^{1/m^{(2)}}\,\Big[1 + \tanh\Big(\frac{10}{\Delta}(\vartheta - \vartheta_g)\Big)\Big], \end{aligned}\right\} \tag{8.29}$$

with $\dot{\epsilon}^{p(2)}$ the equivalent tensile plastic strain-rate. The parameters $(m^{(2)}, S^{(2)})$ are constants, $\dot{\epsilon}_r$ is same as the reference rate used in (8.2).

8.1.4 Constitutive equations for $\alpha = 3$

1. **Free energy. Cauchy stress**

For a free energy function of the form

$$\psi^{(3)} = -\frac{1}{2}\,\mu^{(3)}\,I_m^{(3)}\,\ln\left(1 - \frac{I_1^{(3)} - 3}{I_m^{(3)}}\right), \tag{8.30}$$

where $I_1^{(3)} \stackrel{\text{def}}{=} \left(U_1^{e(3)}\right)^2 + \left(U_2^{e(3)}\right)^2 + \left(U_3^{e(3)}\right)^2$, analogous to the case $\alpha = 2$, we have the contribution

$$\sigma^{(3)} = \mu^{(3)}\left(1 - \frac{I_1^{(3)} - 3}{I_m^{(3)}}\right)^{-1}\left(\left(U^{e(3)}\right)^2 - \left(U^{e(3)}\right)^{-1}\right) \tag{8.31}$$

to the total one-dimensional Cauchy stress σ. Here $\mu^{(3)} > 0$ and $I_m^{(3)} > 3$ are two temperature-independent material parameters.

2. **Flow rule**

The evolution equation for $U^{p\,(3)}$ is

$$\left.\begin{aligned} \dot{U}^{p\,(3)} &= D^{p\,(3)}U^{p\,(3)} \qquad D^{p\,(3)} = \dot{\epsilon}^{p(3)}\text{sign}(\sigma^{(3)}), \\ \dot{\epsilon}^{p(3)} &= \frac{1}{2}\dot{\epsilon}_r\Big(\frac{|\sigma^{(3)}|}{S^{(3)}}\Big)^{1/m^{(3)}}\,\Big[1 + \tanh\Big(\frac{10}{\Delta}(\vartheta - \vartheta_g)\Big)\Big], \end{aligned}\right\} \tag{8.32}$$

where $\dot{\epsilon}^{p(3)}$ is the equivalent tensile plastic strain-rate, and the parameter $m^{(3)}$ is a constant, while $S^{(3)}$ evolves, as discussed below.

3. **Evolution equations for internal variable $S^{(3)}$:**

   The evolution of $S^{(3)}$ is taken to be governed by

$$\dot{S}^{(3)} = h_3\,(\bar{\lambda} - 1)\,\dot{\epsilon}^{p(3)} \quad \text{with initial value} \quad S^{(3)}(0) = S_0^{(3)} \geq 0, \tag{8.33}$$

   where

$$\bar{\lambda} \stackrel{\text{def}}{=} \sqrt{(U + 2U)/3}, \tag{8.34}$$

   is an effective stretch, and $h_3(\vartheta)$ and $S_0^{(3)}(\vartheta)$ are temperature-dependent material parameters, (4.71).

8.1.5 Evolution equation for temperature

For one-dimensional tests at the highest strain rates, *which may be approximated as adiabatic*, the temperature is taken to evolve according to

$$c\dot{\vartheta} = \omega\,\left(\bar{\sigma}^{(1)}\,\dot{\epsilon}^{p(1)} + \tfrac{1}{2}\,B\,\gamma\,|\ln A|^2\,\dot{\epsilon}^{p(1)} + |\sigma^{(2)}|\,\dot{\epsilon}^{p(2)} + |\sigma^{(3)}|\,\dot{\epsilon}^{p(3)}\right) \tag{8.35}$$

with $\omega = 0.7$.

8.2 Material parameter calibration

We have implemented the one-dimensional version of the constitutive theory in MATLAB using an explicit integration scheme, and we use it to calibrate the material parameters from the experiments described in §2. The one-dimensional calibration process consists of four sequential steps which are outlined in this section. The four steps cover calibration of the following aspects of the stress-strain response: (1) elastic modulus and rate dependence of ϑ_g; (2) initial yield stress; (3) large-strain behavior; and (4) yield-peak and back-stress.

8.2.1 Temperature dependence of E and strain rate dependence of ϑ_g

The temperature dependence of the modulus E is taken in the same form as that for G in (4.8):

$$E(\vartheta) = \tfrac{1}{2}(E_{gl} + E_r) - \tfrac{1}{2}(E_{gl} - E_r)\tanh\left(\frac{1}{\Delta}(\vartheta - \vartheta_g)\right) - M_E(\vartheta - \vartheta_g), \tag{8.36}$$

where

$$M_E = \begin{cases} M_{Egl} & \vartheta \leq \vartheta_g, \\ M_{Er} & \vartheta > \vartheta_g, \end{cases} \tag{8.37}$$

and ϑ_g is the *rate-dependent* glass transition temperature, cf. (8.2). Experimental values of E were estimated from the initial slopes of the experimentally-measured stress-strain curves at small strains, at the various different temperatures and the four different strain ratees. The reference strain rate $\dot{\epsilon}_r$ in (8.2) was chosen as the slowest rate 3×10^{-4} s^{-1} in our experiments, and the elastic modulus data was fit to (8.36) and (8.2). The resulting material parameters for the fit shown in Fig. 28 are

$$\begin{array}{llll} \dot{\epsilon}_r = 3 \times 10^{-4}\ \text{s}^{-1}, & \vartheta_r = 404\ \text{K}, & n = 2.5\ \text{K}, & E_{gl} = 1350\ \text{MPa}, \\ E_r = 10\ \text{MPa}, & \Delta = 2.0\ \text{K}, & M_{Egl} = 0.45\ \text{MPa K}^{-1}, & M_{Er} = 0.1\ \text{MPa K}^{-1}. \end{array}$$

8.2.2 Initial yield stress

1. **Initial yield at temperatures below ϑ_g**

   First we consider the material parameters related to the flow stress at temperatures below ϑ_g. Since the stress-peak is associated with the transient disordering of the material, and the actual level of a peak is very dependent on the initial thermal history of the material, here we follow a different approach. We identify a "yield stress" in a compression experiment as a back-extrapolated value of the intersection of

the initial elastic slope with the tangent to the stress-strain curve at a strain of, say, 0.4, a strain level by which all transients of the yield-peak have died out, and the chain-locking effects giving rise to the stress-strain curve are minimal. Accordingly, at this point in the calibration procedure we ignore the effects of the yield-peak and define the "yield stress" as the intersection of the pre-peak stress-strain curve with the back-extrapolated tangent to the stress-strain curve at approximately 0.4 strain; this is shown schematically in Fig. 29.

Since

$$|\sigma^{(1)} - \sigma_{\rm back}| = (\sigma^{(1)} - \sigma_{\rm back})\,{\rm sign}(\sigma^{(1)} - \sigma_{\rm back})$$

and since in a monotonic compression test

$${\rm sign}(\sigma^{(1)} - \sigma_{\rm back}) = {\rm sign}(\sigma^{(1)}) = {\rm sign}(\sigma_{\rm back}),$$

we have

$$|\sigma^{(1)} - \sigma_{\rm back}| = |\sigma^{(1)}| - |\sigma_{\rm back}|,$$

and hence, from (8.16),

$$\left(1 - \frac{\alpha_p}{3}\right)|\sigma^{(1)}| = S_a + S_b + |\sigma_{\rm back}| + \frac{2k_b\vartheta}{V}\sinh^{-1}\left[\left(\frac{\dot\epsilon^{p(1)}}{\dot\epsilon^*(\vartheta)}\right)^{m^{(1)}}\right]. \tag{8.38}$$

Thus, neglecting the contribution from the internal variables S_a(which is associated with the transient yield peak) and the contribution from S_b (since this only manifests itself at large stretches), for fully-developed flows when $\dot\epsilon^{p(1)} \approx \dot\epsilon$ (taken to be positive in compression) and with $|\sigma^{(1)}| = \sigma_y$, (8.38) gives the following approximate expression for yield stress σ_y as a function of temperature ϑ and strain rate $\dot\epsilon$:

$$\left(1 - \frac{\alpha_p}{3}\right)\sigma_y \approx \sigma^*_{\rm back}(\vartheta) + \frac{2k_B\vartheta}{V}\sinh^{-1}\left[\left(\frac{\dot\epsilon}{\dot\epsilon^*(\vartheta)}\right)^{m^{(1)}}\right], \tag{8.39}$$

where we have introduced the notation

$$\sigma^*_{\rm back}(\vartheta) \stackrel{\rm def}{=} |\sigma_{\rm back}(\vartheta)|. \tag{8.40}$$

Here, $\sigma^*_{\rm back}(\vartheta)$ represents a temperature-dependent *saturation value* of the back-stress in compression.[23] Because of the assumed temperature dependence (4.17) of the back-stress modulus, $\sigma^*_{\rm back}$ decreases linearly with temperature,

$$\sigma^*_{\rm back} = R(\vartheta_g - \vartheta) \quad \text{for} \quad \vartheta \le \vartheta_g, \tag{8.41}$$

where R is a material parameter.[24]

Finally, recalling (8.17) and (4.33),

$$\dot\epsilon^*(\vartheta) = \dot\epsilon_0^{(1)}\,\exp\left(-\frac{Q_{gl}}{k_B\vartheta}\right) \quad \text{for} \quad \vartheta \le \vartheta_g. \tag{8.42}$$

To summarize, from (8.39), (8.41), and (8.42), there is a list of six material parameters

$$\{\,\alpha_p,\, \dot\epsilon_0^{(1)},\, m^{(1)},\, V,\, Q_{gl}, R\,\}$$

[23]For the purpose of obtaining material parameters associated with the "yield stress," we ignore the evolution of the back-stress and use the temperature-dependent *saturation* value for the back-stress as an internal stress in the one-dimensional theory. In order to make connection with the work of Richeton et al. (2005, 2006, 2007), one may identify $\sigma^*_{\rm back}(\vartheta)$ with their internal stress $\sigma_i(\vartheta)$. Note, however, that in the work of Richeton et al., $\sigma_i(\vartheta)$ is always a positive valued scalar internal stress which leads to isotropic hardening, whereas in our more general theory the back-stress may in general be positive or negative, and is not only temperature dependent, but also evolves with strain to give rise to kinematic hardening.

[24]For the purpose of fitting the parameters associated with the yield points in the glassy regime, the rate dependence of the glass transition temperature is neglected and for this step of material parameter calibration procedure, we assume the glass transition temperature to be constant and assume $\vartheta_g = \vartheta_r = 404$ K for Zeonex.

that must be calibrated from the experimental data for σ_y as a function of strain rate $\dot{\epsilon}$ and temperature ϑ for temperatures below ϑ_g. The value of the pressure-sensitivity parameter α_p is not determinable from simple compression experiments alone. As reviewed by Crist (1997), for amorphous polymers the pressure-sensitivity parameter α_p in simple tension/compression for PMMA is ≈ 0.35, that for PC is ≈ 0.2, and for amorphous polymers is generally in the range 0.1 to 0.4. We are not aware of any data for the pressure sensitivity of yield for Zeonex in the literature. Here, we assume that $\alpha_p \approx 0.2$ for Zeonex. The parameter $\dot{\epsilon}_0^{(1)}$, represents an attempt frequency for the plastic flow, and we assume that it has the classical value $10^{12}\,\mathrm{s}^{-1}$ for the three polymers.

Following the back-extrapolation method of Fig. 29, values of the yield stress σ_y as a function of temperature ϑ and strain rate $\dot{\epsilon}$ have been estimated from the compression stress-strain curves for Zeonex in the temperature range 25 C to 130 C at four strain-rates. The ratio of these yield stresses to test temperatures, σ_y/ϑ, as a function of the logarithm of strain-rate, $\log_{10}\dot{\epsilon}$ are shown in the Eyring-plot of Fig. 30a. Estimated isotherms have been drawn to visually connect the yield points for a given test temperature. For a given temperature we have only four data points spanning a relatively narrow strain-rate range, which makes fitting the flow function (8.39) difficult. However, by utilizing the shifting and superposition ideas of Richeton et al. (2005, 2006), we can form a master curve of all 16 data points at a single reference temperature that covers a much wider range of strain rates. To obtain the master curve, the experimental data is shifted along both axes by temperature-dependent shift factors defined below:

$$\left.\begin{aligned} \text{Horizontal shift:} \qquad \Delta(\log_{10}\dot{\epsilon}) &= H_h\left(\frac{1}{\vartheta}-\frac{1}{\vartheta_{\text{shift}}}\right), \\ \text{Vertical shift:} \qquad \Delta\left(\frac{\sigma_y}{\vartheta}\right) &= H_v\left(\frac{1}{\vartheta}-\frac{1}{\vartheta_{\text{shift}}}\right), \end{aligned}\right\} \tag{8.43}$$

where ϑ is the temperature of the experiment, ϑ_{shift} is the temperature that the data is shifted to, and H_h and H_v are shift parameters. Richeton et al. (2005, 2006) have argued that these shift factors may be equated with the material parameters appearing in the cooperative flow model such that

$$\left.\begin{aligned} H_h &= \frac{Q_{gl}}{k_B \ln 10}, \\ H_v &= -\sigma^*_{\text{back}}(\vartheta=0) = -R\theta_g. \end{aligned}\right\} \tag{8.44}$$

The master curve constructed at $\vartheta_{\text{shift}} = \vartheta_r = 404$ K $\approx \vartheta_g$ using the shift factors

$$H_h = 5.85\times 10^3 \text{ K}, \qquad H_v = -70 \text{ MPa},$$

is shown in Fig. 30b, and the values of Q_{gl} and R, calculated using (8.44), are

$$Q_{gl} = 1.86\times 10^{-19} \text{ J}, \qquad \text{and} \qquad R = 0.173 \text{ MPa K}^{-1}.$$

For a master curve constructed at $\vartheta_{\text{shift}} = 404$ K $\approx \vartheta_g$, the back-stress term from the flow function (8.39) vanishes, and (8.39) simplifies to

$$\frac{\sigma_y}{\vartheta_g} = \frac{2k_B}{V}\left(1-\frac{\alpha_p}{3}\right)^{-1}\sinh^{-1}\left[\left(\frac{\dot{\epsilon}}{\dot{\epsilon}^*(\vartheta_g)}\right)^{m^{(1)}}\right], \tag{8.45}$$

with the list of unknown parameters reduced to $\{V,\, m^{(1)}\}$. A non-linear least-squares fitting method was used in MATLAB to obtain these parameters from the shifted experimental data. This gives

$$V = 0.98\times 10^{-27}\,\mathrm{m}^3 \qquad \text{and} \qquad m^{(1)} = 0.16,$$

and the resulting fit of (8.45) to the shifted data at 404 K is shown in Fig. 30b as a solid line.

2. **Initial yield at temperatures above ϑ_g**

   As the temperature is increased through the glass transition region, the yield stress drops off very rapidly to negligibly small values. In our model, as the temperature increases through the glass transition, the characteristic strain rate $\dot{\epsilon}^*$ rapidly increases, leading to a relatively fast drop in the yield stress. At temperatures above ϑ_g, the values for the yield stress σ_y were estimated to be the stress value at ≈ 0.04 strain. For the estimated values of the yield stress, corresponding values for characteristic strain rate $\dot{\epsilon}^*$ were calculated using relation (8.39) for each experiment above ϑ_g. With $\dot{\epsilon}^*$ defined as

$$\dot{\epsilon}^*(\vartheta) \stackrel{\text{def}}{=} \dot{\epsilon}_0^{(1)} \exp\left(-\frac{Q}{k_B\vartheta}\right), \tag{8.46}$$

   where the additional temperature dependence of Q governs the change in characteristic strain-rate $\dot{\epsilon}^*(\vartheta)$ through the glass transition. With (4.33) representing the temperature dependence of Q, we are left to determine Q_r. To determine this parameter, values of $\dot{\epsilon}^*$ that were obtained from the experiments were fit for temperatures near and above ϑ_g. The selected values of $\dot{\epsilon}^*$ along with a fit of function (8.46) are shown in Fig. 31 for $Q_r = 1.0 \times 10^{-20}$ J.

8.2.3 Stress-strain response at large strains

This part of the calibration procedure was divided into two steps: (i) material parameter calibration for temperatures above ϑ_g; and (ii) material parameter calibration for temperatures below ϑ_g.

1. **Large strain response above ϑ_g**

   For temperatures above ϑ_g, we allow for network slippage corresponding to micromechanism $\alpha = 2$ and select material parameters $(S^{(2)},\, m^{(2)})$, such that the flow stress associated with (8.29) is negligibly small. We accomplish this by taking

$$S^{(2)} = 0.02 \text{ MPa}, \qquad m^{(2)} = 0.18,$$

   where the value of $m^{(2)}$ is a suitably large value at these high temperatures. Thus, in the calibration procedure above ϑ_g, we may neglect the small contribution from $\sigma^{(2)}$ and set

$$\sigma \approx \sigma^{(1)} + \sigma^{(3)}.$$

   Thus, for $\vartheta > \vartheta_g$ the nonlinear increase in stress at large stretches depends primarily on (i) the evolution of the internal variable S_b in micromechanism $\alpha = 1$ according to (8.20); and (ii) the values of the elastic parameters $(\mu^{(3)},\, I_m^{(3)})$, the value of the flow parameter $m^{(3)}$, and the evolution of the internal variable $S^{(3)}$ in micromechanism $\alpha = 3$.

   Using the one-dimensional MATLAB implementation of the model, together with the material parameters estimated up to this point, the stress-strain response *at a given strain rate and temperature* can be fit by adjusting values of $(h_b,\, S_r)$ for $\alpha = 1$, and the values $(\mu^{(3)},\, I_m^{(3)},\, m^{(3)},\, h_3,\, S_0^{(3)})$ for $\alpha = 3$. In the lists above $(h_b,\, S_r)$, and $(\mu^{(3)},\, I_m^{(3)},\, m^{(3)})$ are presumed to be temperature-independent, while the temperature-dependence of $S_0^{(3)}(\vartheta)$ and $h_3(\vartheta)$ is presumed to follow

$$S_0^{(3)}(\vartheta) = S_g^{(3)} \exp\Big(-Y(\vartheta - \vartheta_g)\Big), \tag{8.47}$$

$$\text{and} \quad h_3(\vartheta) = h_{3g} \exp\Big(-Z(\vartheta - \vartheta_g)\Big). \tag{8.48}$$

   Estimates of the values of the desired material parameter lists

$$(h_b,\, S_r)$$

   for $\alpha = 1$, and

$$(\mu^{(3)},\, I_m^{(3)},\, m^{(3)},\, S_g^{(3)},\, Y,\, h_{3g},\, Z)$$

for $\alpha = 3$ are obtained by *trial-and-error curve-fitting* both the loading and unloading response at large strains for the stress-strain data at temperatures above ϑ_g. A few trials give the estimate as

$$h_b = 1.0, \qquad S_r = 1.5 \text{ MPa}, \qquad \mu^{(3)} = 0.75 \text{ MPa},$$
$$I_m^{(3)} = 6.5, \qquad m^{(3)} = 0.18, \qquad S_g^{(3)} = 5.3 \text{ MPa},$$
$$Y = 0.19 \text{ K}^{-1}, \qquad h_{3g} = 52.0 \text{ MPa}, \qquad Z = 0.178 \text{ K}^{-1}.$$

2. **Large strain response below ϑ_g**

Here, we focus on estimating the material parameters: (i) $\mu^{(2)}$ and $I_m^{(2)}$ in the expression (8.28), together with the temperature dependence of $\mu^{(2)}$ given in (4.46); and (ii) S_{gl} — parameters which account for the stress increase associated with chain-locking at large stretches.

To begin, we neglect the transient response associated with the yield-peak and correspondingly ignore the evolution equations (8.18) and (8.19) for φ and S_a; we return to determining the material parameters appearing in these coupled evolution equations later. We ignore the evolution of the back-stress, and set it constant, using the temperature-dependent saturation value, such that

$$\sigma_{\text{back}}(\vartheta) = \sigma^*_{\text{back}}(\vartheta)\ \text{sign}(\sigma_{\text{back}}) = \begin{cases} -R(\vartheta_g - \vartheta) & \text{if} \quad \vartheta \leq \vartheta_g, \\ 0 & \text{if} \quad \vartheta > \vartheta_g, \end{cases} \tag{8.49}$$

and determine material parameters associated with the evolution of the back-stress later. The parameter $I_m^{(2)}$ is presumed to be temperature-independent while the temperature dependence of $\mu^{(2)}(\vartheta)$ is presumed to follow

$$\mu^{(2)}(\vartheta) = \mu_g^{(2)}\ \exp\Big(- N(\vartheta - \vartheta_g)\Big), \tag{8.50}$$

(cf., (4.46). Using the one-dimensional MATLAB implementation of the model, together with the material parameters estimated to this point, estimates for the desired parameter list

$$(\mu_g^{(2)},\, N,\, I_m^{(2)},\, S_{gl})$$

are relatively easily obtained by curve-fitting both the loading and unloading response at large strains for the stress-strain data at the lowest strain rate. A few trials give the estimates as

$$\mu_g^{(2)} = 2.8 \text{ MPa}, \qquad N = 12.4 \times 10^{-3} \text{ K}^{-1}, \qquad I_m^{(2)} = 6.2, \qquad S_{gl} = 120 \text{ MPa}.$$

8.2.4 Yield-peak and back-stress evolution

Finally, we calibrate material parameters associated with the yield-peak and the back-stress evolution for temperatures below ϑ_g. Both the back-stress and yield-peak are observed to vanish above the glass transition temperature of the material. This step in the calibration procedure is an iterative process, and requires fitting the transient stress-overshoot in the simple compression stress-strain response together with the creep response, iteratively, several times in order to get a good fit. The steps in the iterative procedure are listed below.

Step 1:

The parameters related to the change of back-stress σ_{back} with strain and temperature are γ and X (cf. (8.22), (4.17)). To begin, we note that for compression

$$D^{p(1)} = -\dot{\epsilon}^{p(1)}, \tag{8.51}$$

and we may then rewrite the evolution equation for A (8.22) as

$$\dot{A} = -(2 + \gamma \ln A)\, A\, \dot{\epsilon}^{p(1)}. \tag{8.52}$$

It follows then that the saturation value of A in compression is

$$A^* = \exp\left(-\frac{2}{\gamma}\right). \tag{8.53}$$

Combining this result with the equation for the back-stress (8.10) gives the saturation value of the back-stress as a function of the material parameters $B(\vartheta)$ and γ

$$\sigma^*_{\text{back}}(\vartheta) = 3\,\frac{B(\vartheta)}{\gamma}\,. \tag{8.54}$$

Equating the saturation value for the back-stress using (4.17) and (8.41) we obtain

$$3\,\frac{X(\vartheta_g - \vartheta)}{\gamma} = R(\vartheta_g - \vartheta) \quad \Rightarrow \quad X = \frac{R}{3}\,\gamma, \tag{8.55}$$

and since R has already been determined, we obtain the fixed value for the ratio X/γ.

Step 2:

In this step we estimate a value for γ, and calculate the corresponding value for X from (8.55) to get an estimate for the parameters involved in the evolution of the back-stress. We assume the material begins in a well-annealed "ground-state," so that we may take the initial value of the order parameter φ and stress-like internal resistance S_a to be zero. This leaves one with a list of parameters $\{h_a, b, g, \varphi^*\}$ in the evolution equations (8.18) and (8.19) for φ and S_a to calibrate the yield-peak.

To find $\{\, h_a,\, b,\, g,\, \varphi^* \,\}$, several simulations are performed using different values of parameters to approximately match the shape of the yield-peak at the various strain rates and temperatures. The parameter h_a controls the initial slope of the yield peak, the parameters b and φ^* control the height of the yield peak, while the parameter g controls the width of the yield-peak.

Step 3:

With the parameters for yield-peak estimated, one returns to refining the values of the material parameters in the back-stress evolution. To get refined estimates for the recovery parameter γ and the temperature sensitivity parameter X for the back-stress modulus B, we first note that γ controls the rate of saturation of the back-stress. As γ increases, the back-stress approaches its saturation value more rapidly.

The parameters γ and B significantly affect the creep response of the material.[25] In order to get more refined estimates for these parameters, we turn to a limited set of available data for room-temperature creep of Zeonex shown in Fig. 32 as solid lines. The value of γ is chosen such that the creep response is adequately represented, as shown by the dashed lines in Fig. 32.

Steps 2 and 3 are iteratively repeated until the yield-peaks in the total stress-strain response of the material, as well as the creep response, are satisfactorily calibrated. Once $\{\, h_a,\, b,\, g,\, \varphi^* \,\}$ are determined for each stress-strain curve, we have found that to a good approximation, the parameters h_a, b and g may be taken as constants and φ^* as both temperature and strain-rate dependent. The temperature and strain rate dependence of φ^* was fit to the functional form (8.19).

The material parameters for Zeonex that give a reasonable fit for the yield-peak for the range of temperatures and strain rates under consideration, and also adequately reproduce the limited creep data, are

$$\begin{aligned} &h_a = 300, && b = 10.13 \times 10^3 \text{ MPa}, && g = 13.0, && z = 0.0057, \\ &r = 0.24, && s = 0.042, && \gamma = 12, && X = 0.7 \text{ MPa K}^{-1}. \end{aligned}$$

[25] Cyclic tension-compression stress-strain curves at different temperatures may also be used to fit the back-stress parameters, but we have not conducted the necessary extensive set of such experiments.

8.3 Parameters for the three-dimensional model

Except for the list of parameters

$$\{\,\nu_r,\,\nu_0^{(1)},\,\alpha_p,\,V,\,h_a,\,b,\,g,\,\gamma,\,h_b,\,S_{gl},\,S_r,\,S^{(2)},\,S_g^{(3)},\,h_{3g}\,\}, \tag{8.56}$$

the values of the one-dimensional material parameters are unchanged when used in the three-dimensional equations. Noting that

$$\tau\nu = \sigma\dot{\epsilon}, \quad \sigma = \sqrt{3}\tau, \quad \dot{\epsilon} = \frac{\nu}{\sqrt{3}} \tag{8.57}$$

the parameters listed in (8.56) may be converted from the one-dimensional compression form to the three-dimensional shear form using

$$\left.\begin{aligned}
\nu_r &= \sqrt{3}\,\dot{\epsilon}_r\,, & \nu_0^{(1)} &= \sqrt{3}\,\dot{\epsilon}_0^{(1)}\,, & \alpha_p^{(\text{shear})} &= \tfrac{1}{\sqrt{3}}\,\alpha_p^{(\text{comp})}\,,\\
V^{(\text{shear})} &= \sqrt{3}\,V^{(\text{comp})}\,, & h_a^{(\text{shear})} &= \tfrac{1}{\sqrt{3}}\,h_a^{(\text{comp})}\,, & b^{(\text{shear})} &= \tfrac{1}{\sqrt{3}}\,,\, b^{(\text{comp})}\,,\\
g^{(\text{shear})} &= \tfrac{1}{\sqrt{3}}\,g^{(\text{comp})}\,, & \gamma^{(\text{shear})} &= \tfrac{1}{\sqrt{3}}\,\gamma^{(\text{comp})}\,, & h_b^{(\text{shear})} &= \tfrac{1}{\sqrt{3}}\,h_b^{(\text{comp})}\,,\\
S_{gl}^{(\text{shear})} &= \tfrac{1}{\sqrt{3}}\,S_{gl}^{(\text{comp})}\,, & S_r^{(\text{shear})} &= \tfrac{1}{\sqrt{3}}\,S_r^{(\text{comp})}\,, & S^{(2)(\text{shear})} &= \tfrac{1}{\sqrt{3}}S^{(2)(\text{comp})}\,,\\
S_g^{(3)(\text{shear})} &= \tfrac{1}{\sqrt{3}}S_g^{(3)(\text{comp})}\,, & h_{3g}^{(\text{shear})} &= \tfrac{1}{3}h_{3g}^{(\text{comp})}\,.
\end{aligned}\right\} \tag{8.58}$$

Further, to convert the temperature dependence parameters for the elastic modulus E to those of the shear modulus G, we use the following standard relations

$$G_{gl} = \frac{E_{gl}}{2\,(1+\nu_{gl}^{\text{poi}})} \quad \text{and} \quad G_r = \frac{E_r}{2\,(1+\nu_r^{\text{poi}})}\,. \tag{8.59}$$

The material parameters for the three-dimensional theory that were determined by following the procedure described in this Appendix are listed for Zeonex, PC, and PMMA in Table 1.

Table 1: Material parameters for Zeonex, PC, and PMMA

Parameter	Zeonex-690R	PC	PMMA
ρ (kg m^{-3})	1010	1200	1200
α_{gl} (K^{-1})	7×10^{-5}	6.5×10^{-5}	7×10^{-5}
α_r (K^{-1})	12×10^{-5}	12×10^{-5}	16×10^{-5}
ν_r (s^{-1})	5.2×10^{-4}	5.2×10^{-4}	5.2×10^{-4}
ϑ_r (K)	404	415	386
n (K)	2.5	2.2	2.6
Δ (K)	2.0	1.6	1.7
G_{gl} (MPa)	482	640	300
G_r (MPa)	3.4	4.0	1.4
M_{gl} (MPa K^{-1})	0.16	0.73	10
M_r (MPa K^{-1})	0.034	0.017	.003
ν_{gl}^{poi}	0.40	0.37	0.35
ν_r^{poi}	0.49	0.49	0.49
X (MPa K^{-1})	0.7	1.5	12.2
γ	6.93	26.0	34.6
α_p	0.116	0.116	0.2
$\nu_0^{(1)}$ (s^{-1})	1.73×10^{12}	1.73×10^{12}	1.73×10^{12}
$m^{(1)}$	0.16	0.14	0.22
V (m^3)	1.7×10^{-27}	1.62×10^{-27}	0.52×10^{-27}
Q_{gl} (J)	1.86×10^{-19}	2.0×10^{-19}	1.3×10^{-19}
Q_r (J)	1×10^{-20}	3×10^{-20}	3×10^{-20}
h_a	173	58	70
b (MPa)	5850	5850	5850
g	7.5	7.4	5.2
z	0.0057	0.0058	0.012
r	0.24	0.2	0.62
s	0.042	0.005	0.052
h_b	0.577	0.577	0.577
S_{gl} (MPa)	69.3	52.0	23.0
S_r (MPa)	0.87	0.46	0.0
$\mu_g^{(2)}$ (MPa)	2.8	3.2	1.3
N (K^{-1})	12.4×10^{-3}	13.5×10^{-3}	31.3×10^{-3}
$I_m^{(2)}$	6.2	6.6	5.0
$m^{(2)}$	0.18	0.18	0.22
$S^{(2)}$ (MPa)	0.01	0.01	0.01
$\mu^{(3)}$ (MPa)	0.75	1.0	0.75
$I_m^{(3)}$	6.5	12.0	9.0
$m^{(3)}$	0.18	0.18	0.22
$S_g^{(3)}$ (MPa)	3.0	2.77	3.1
Y (K^{-1})	0.19	0.2	0.04
h_{3g} (MPa)	17.3	16.7	46.6
Z (K^{-1})	0.178	0.19	0.028

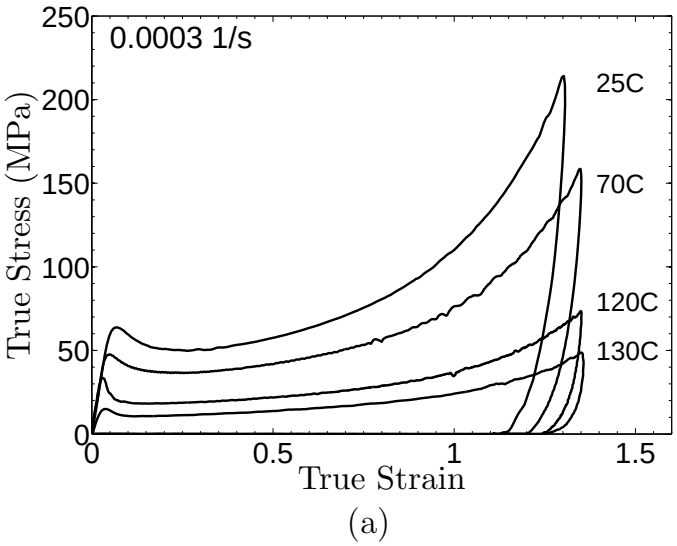

(a)

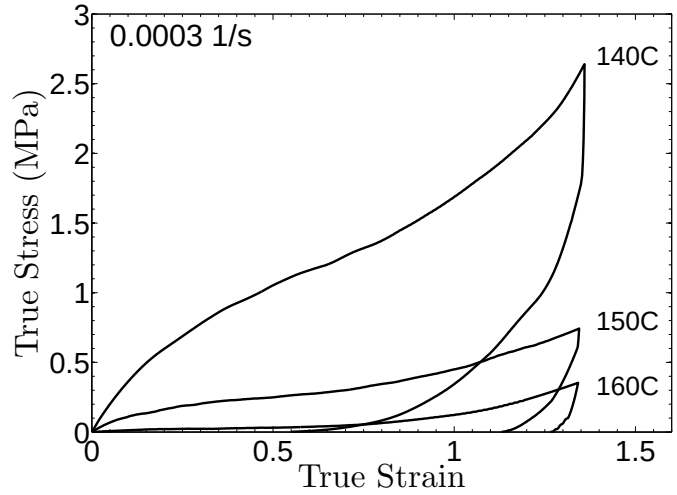

(b)

Figure 1: Stress-strain curves in simple compression for Zeonex at various temperatures ranging from 25 C to 160 C at a strain rate of $3\times10^{-4}\,\mathrm{s}^{-1}$: (a) for temperatures below $\vartheta_g \approx 136\,\mathrm{C}$; (b) for temperatures above ϑ_g. Note the change in scale for the stress axis between the two figures.

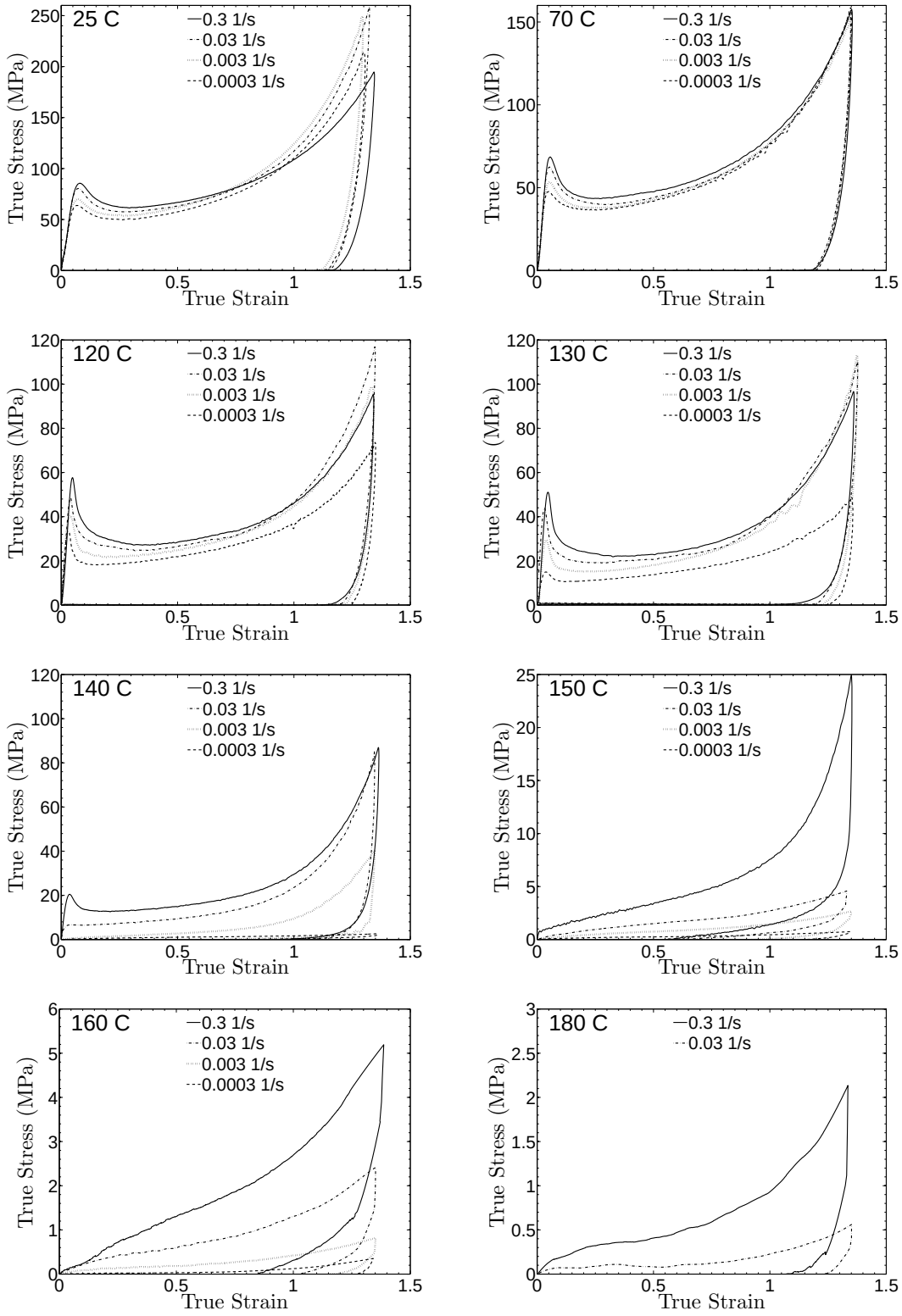

Figure 2: Stress-strain curves in simple compression for Zeonex at strain rates of 3×10^{-1}, 3×10^{-2}, 3×10^{-3}, and $3\times10^{-4}\,\mathrm{s}^{-1}$, and at temperatures of 25 C, 70 C, 120 C, 130 C, 140 C, 150 C, 160 C, and 180 C. Note the change in scale for the stress axis between various figures.

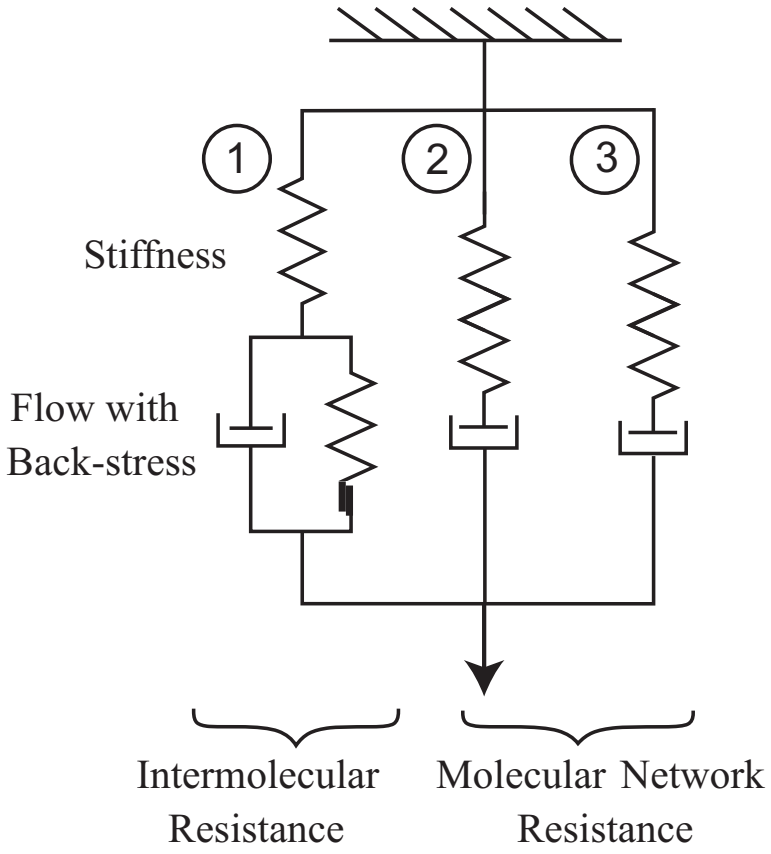

Figure 3: A schematic "spring-dashpot"-representation of the constitutive model.

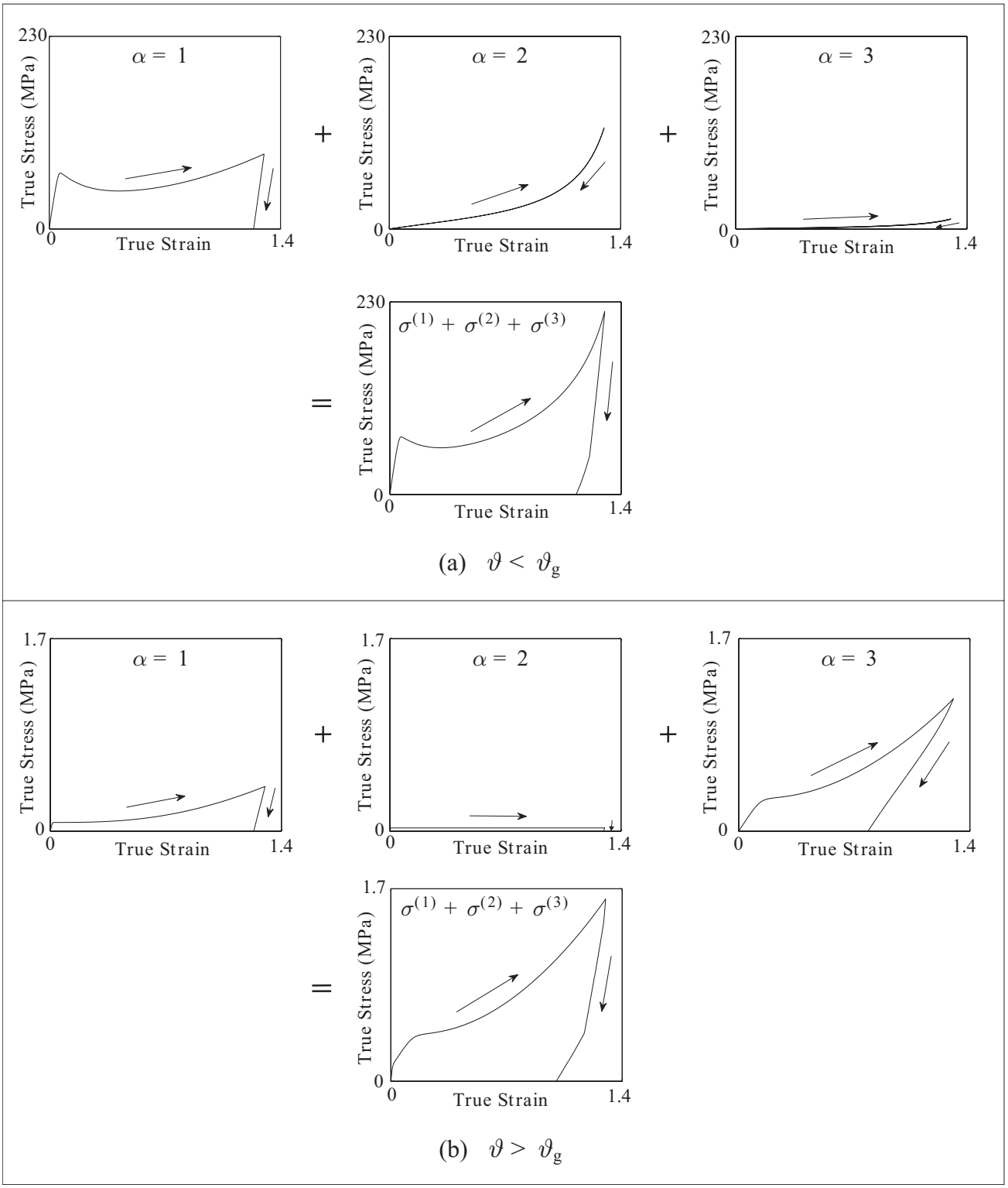

Figure 4: Schematic plots of stress-strain contributions from individual micromechanisms to an overall simple compression stress-strain response for: (a) a temperature below ϑ_g; and (b) a temperature above ϑ_g. Note change in scale for the stress axis between the figures in (a) and (b).

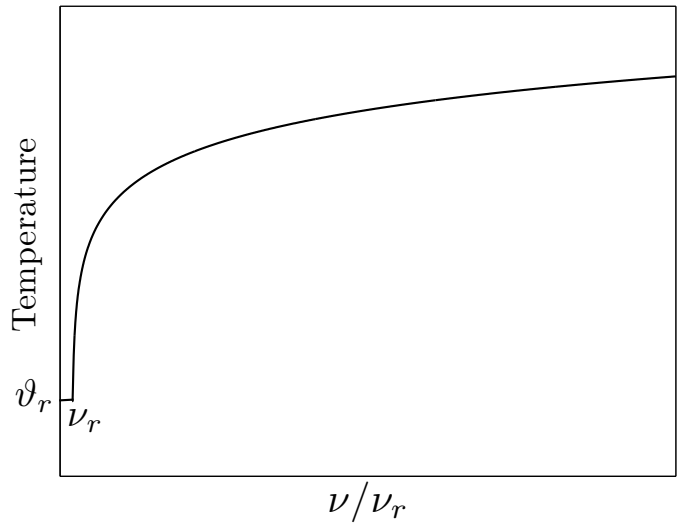

Figure 5: Schematic of dependence of glass transition temperature on the shear strain rate ν. Here ϑ_r is a reference glass transition temperature at a low reference shear strain rate ν_r.

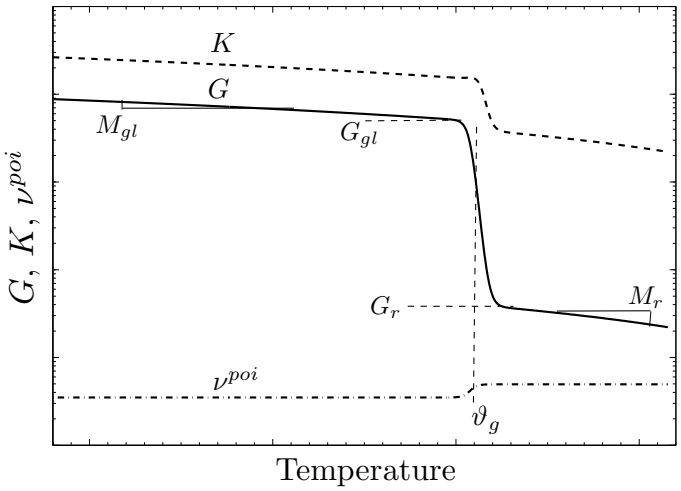

Figure 6: Schematic of temperature-dependence of shear modulus G, bulk modulus K and Poisson's ratio ν^{poi}. Note that the ordinate is plotted on a logarithmic scale.

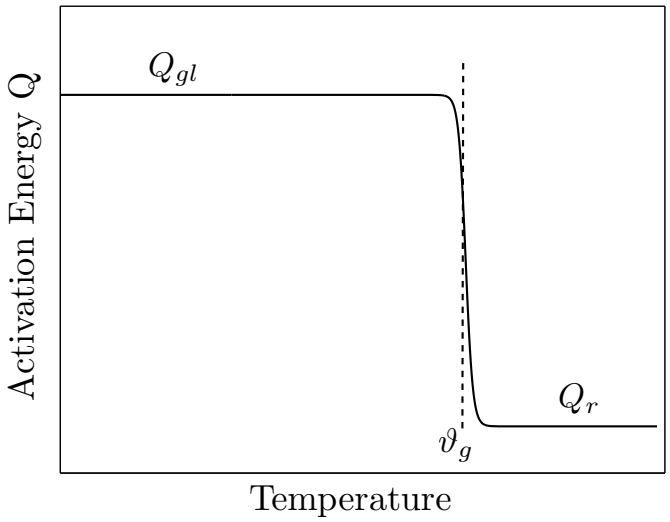

Figure 7: Schematic of temperature dependence of activation energy Q.

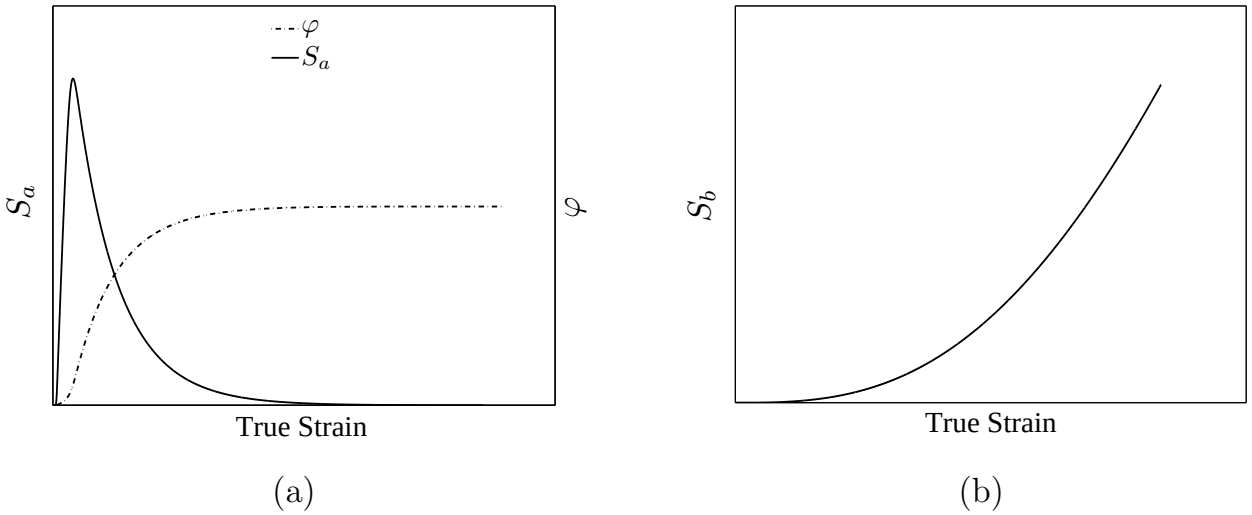

Figure 8: Schematic of the evolution of internal variables (φ, S_a, S_b) with strain: (a) evolution of φ and S_a; and (b) evolution of S_b.

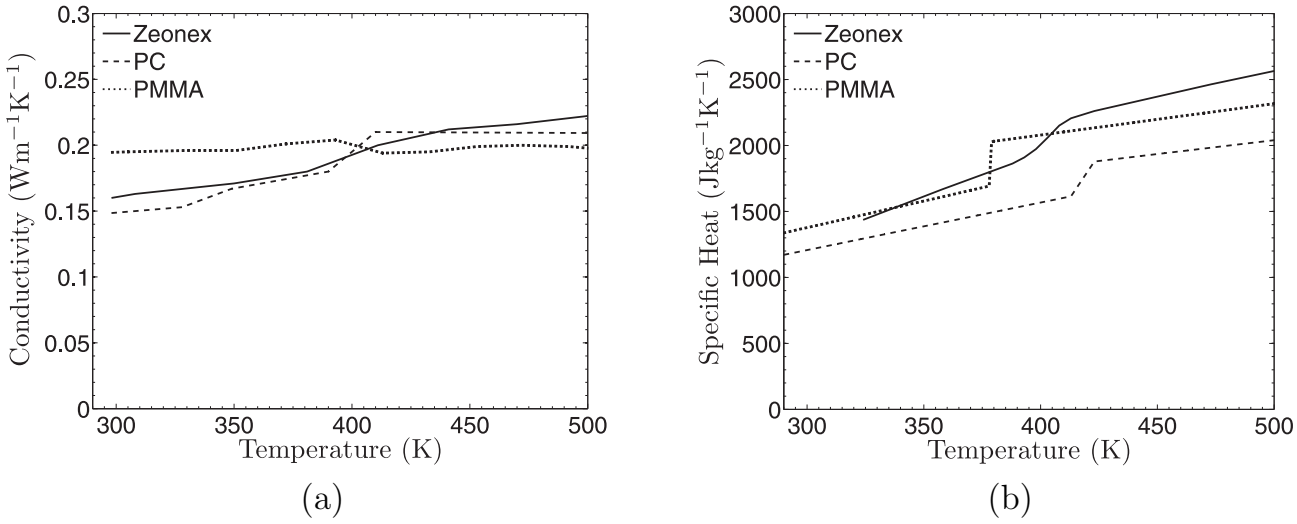

Figure 9: Temperature dependence of (a) thermal conductivity, and (b) specific heat.

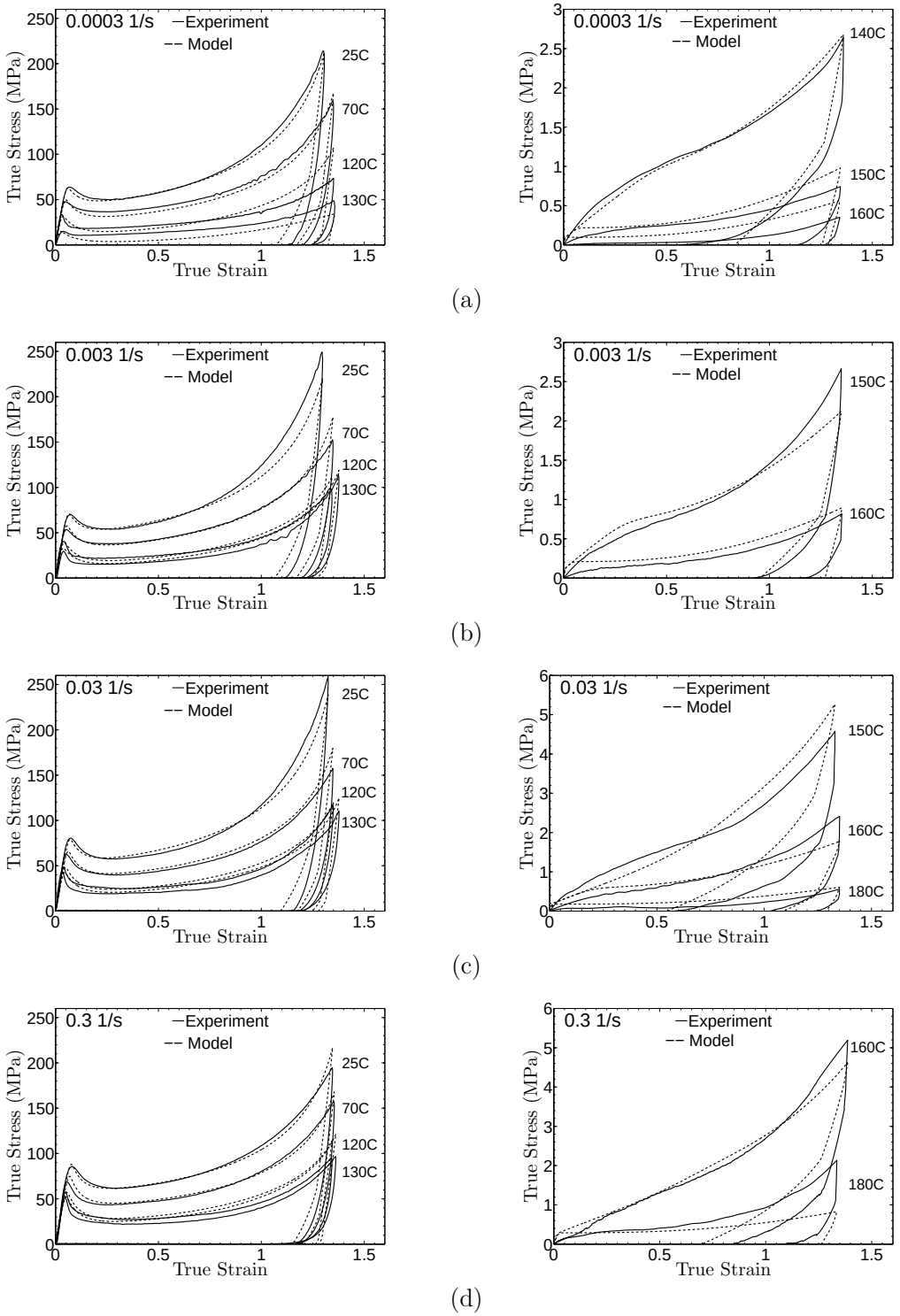

Figure 10: Fit of the model to experimental stress-strain curves for Zeonex at various temperatures ranging from 25 C to 180 C at four strain rates (a) 3×10^{-4} s^{-1}, (b) 3×10^{-3} s^{-1}, (c) 3×10^{-2} s^{-1}, and (d) 3×10^{-1} s^{-1}. The experimental data is plotted as solid lines, while the fit is shown as dashed lines.

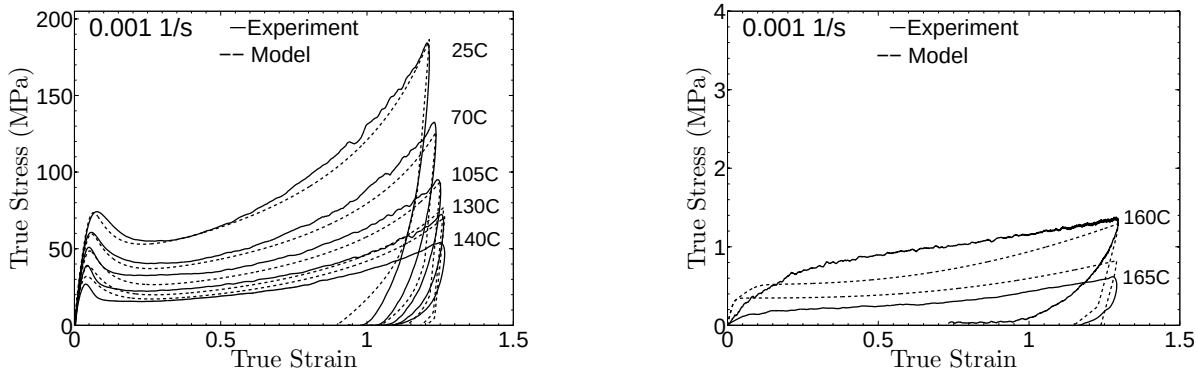

(a)

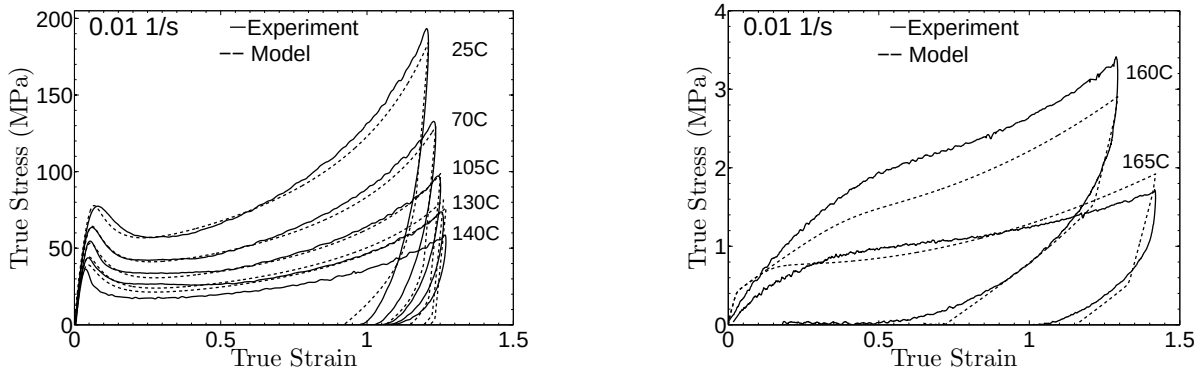

(b)

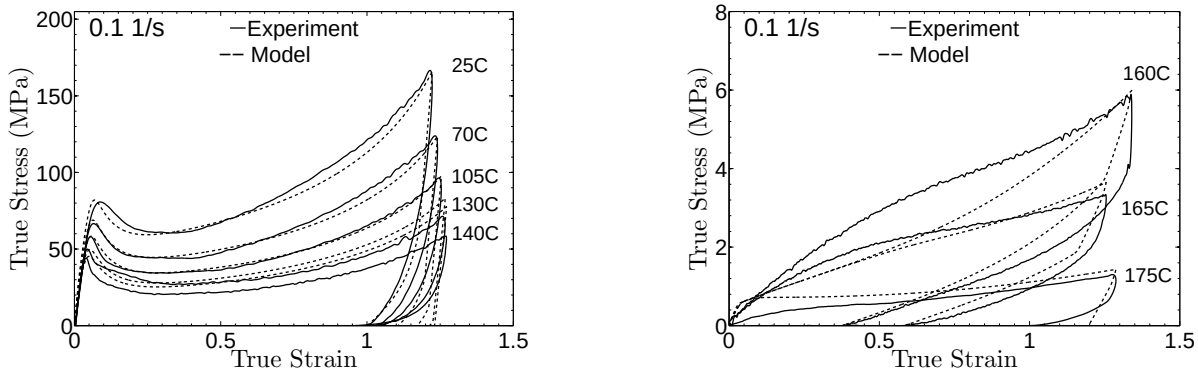

(c)

Figure 11: Fit of the model to experimental stress-strain curves for PC at various temperatures ranging from 25 C to 175 C at three strain rates (a)10^{-3} s^{-1}, (b) 10^{-2} s^{-1}, and (c) 10^{-1} s^{-1}. The experimental data is plotted as solid lines, while the fit is shown as dashed lines.

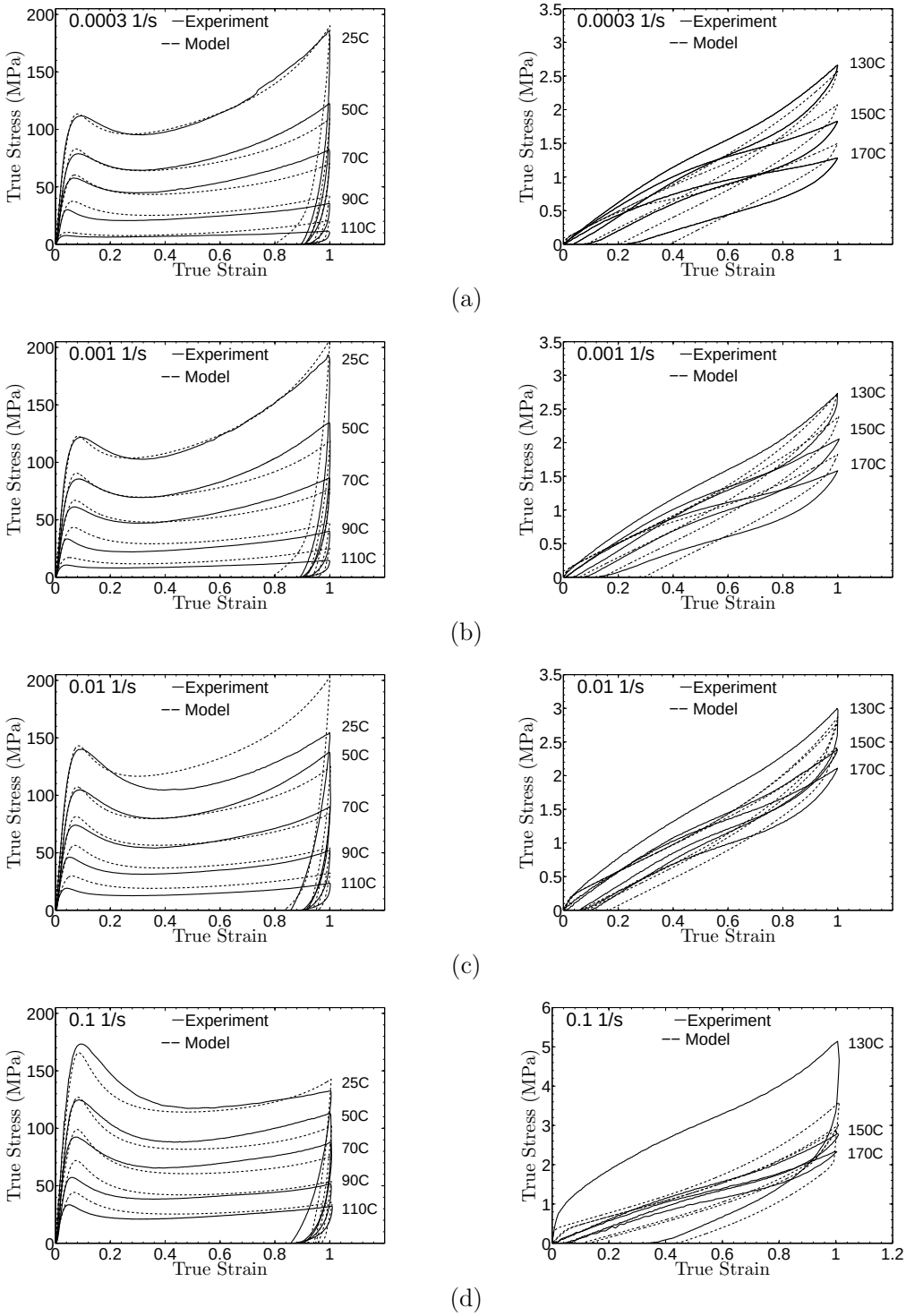

Figure 12: Fit of the model to experimental stress-strain curves for PMMA at various temperatures ranging from 25 C to 170 C at four strain rates (a) 3×10^{-4} s^{-1}, (b) 10^{-3} s^{-1}, (c) 10^{-2} s^{-1}, and (d) 10^{-1} s^{-1}. The experimental data is plotted as solid lines, while the fit is shown as dashed lines.

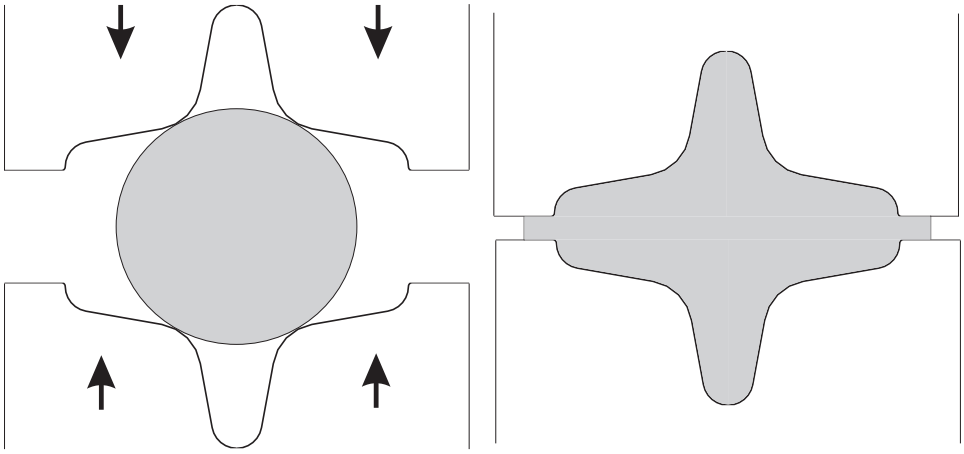

Figure 13: Schematic of the plane-strain cruciform forging experiment.

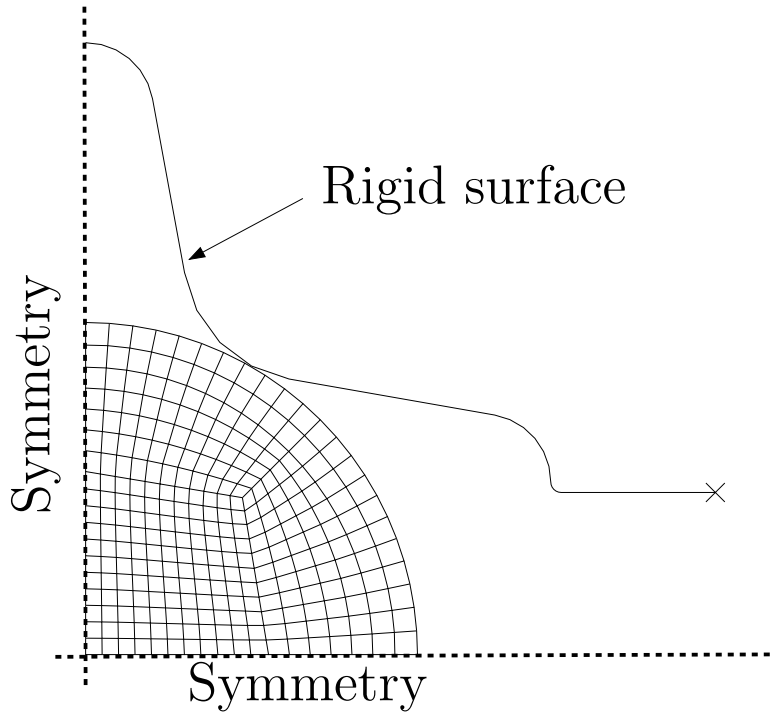

Figure 14: Quarter-symmetry finite element mesh for the workpiece and the rigid surface used in the plane-strain cruciform forging simulations.

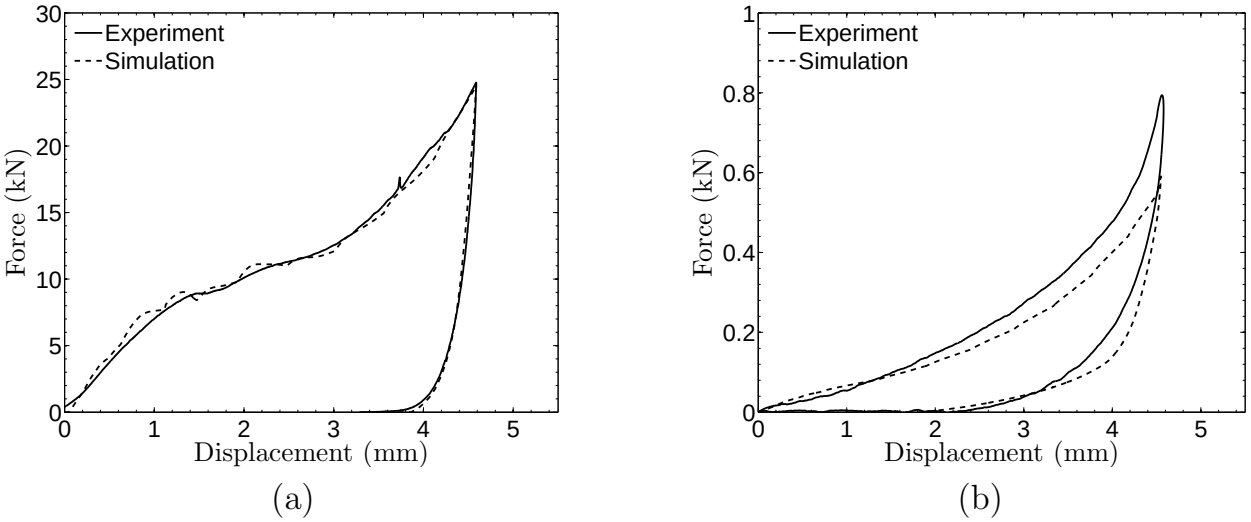

Figure 15: Comparison of the numerically-predicted and experimentally-measured force-displacement curves for forgings of PC at (a) 25 C and (b) 160 C. Note change in scale for the force axis between the two figures.

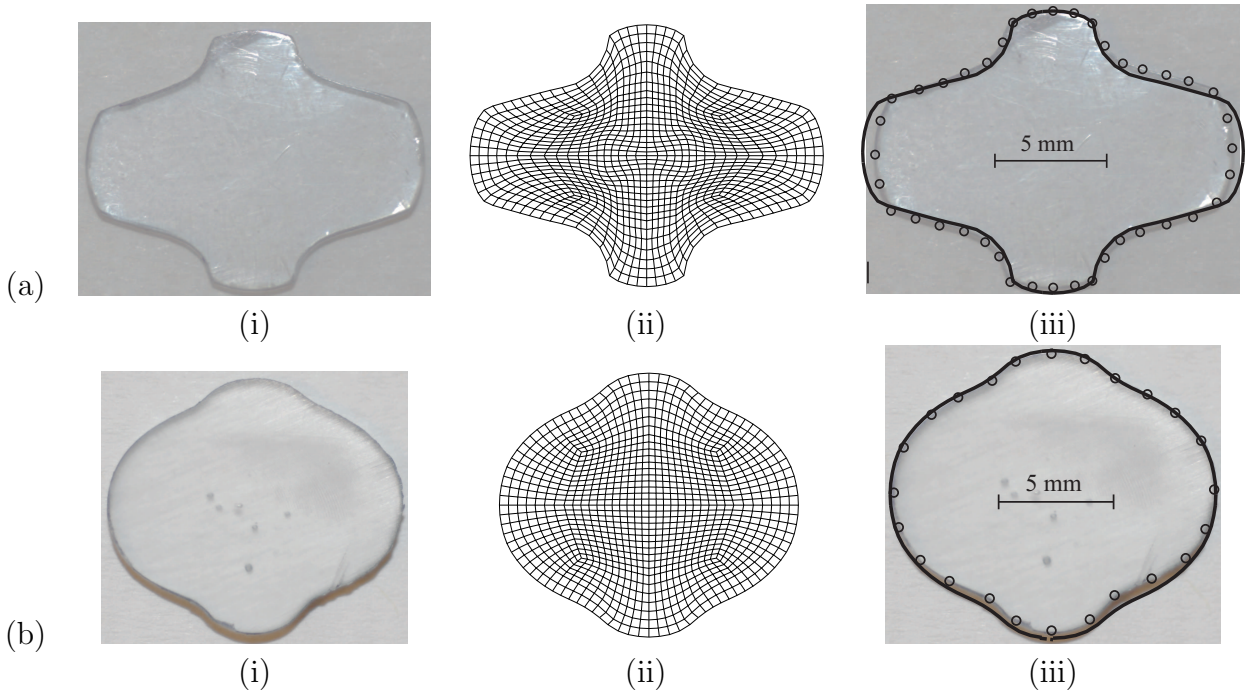

Figure 16: Comparison of the numerically-predicted and experimentally-measured deformed shapes from the cruciform forgings for (a) the forging at 25 C, top row, and (b) the forging at 160 C, bottom row: (i) Experimental macrographs; (ii) deformed meshes after unloading, die removal, and cooling to room temperature; and (iii) outlines of simulated shapes superimposed over the experimentally-measured shapes — the solid lines are the edge-geometries from the numerical simulations, and the circles outline the geometry of the specimens from the experiments.

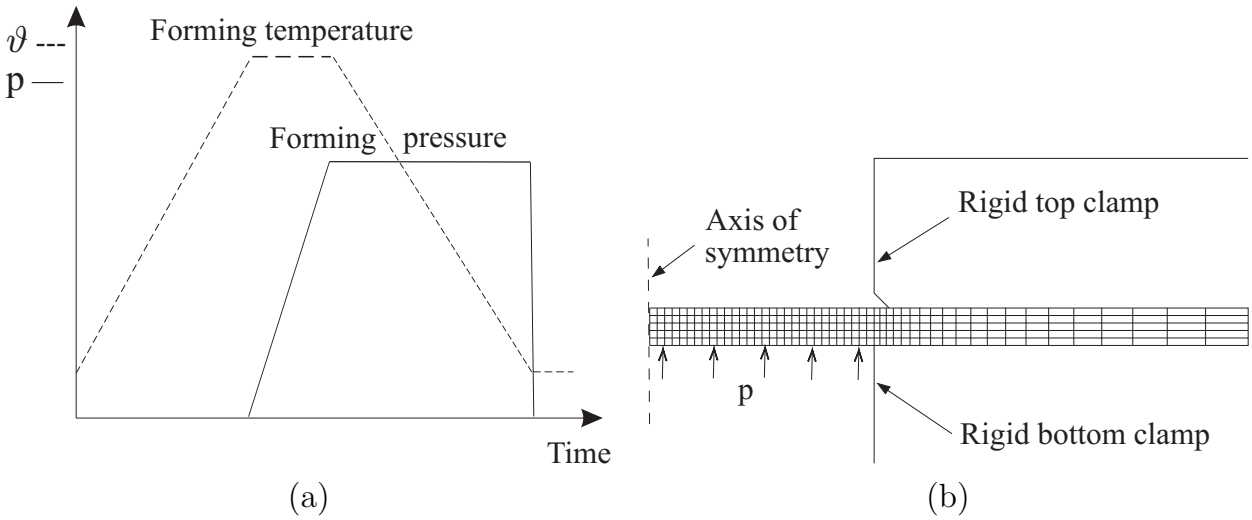

Figure 17: (a) Schematic of the temperature and pressure process history for the blow-forming operation. (b) Half-symmetry finite element mesh used for the axi-symmetric blow-forming simulations.

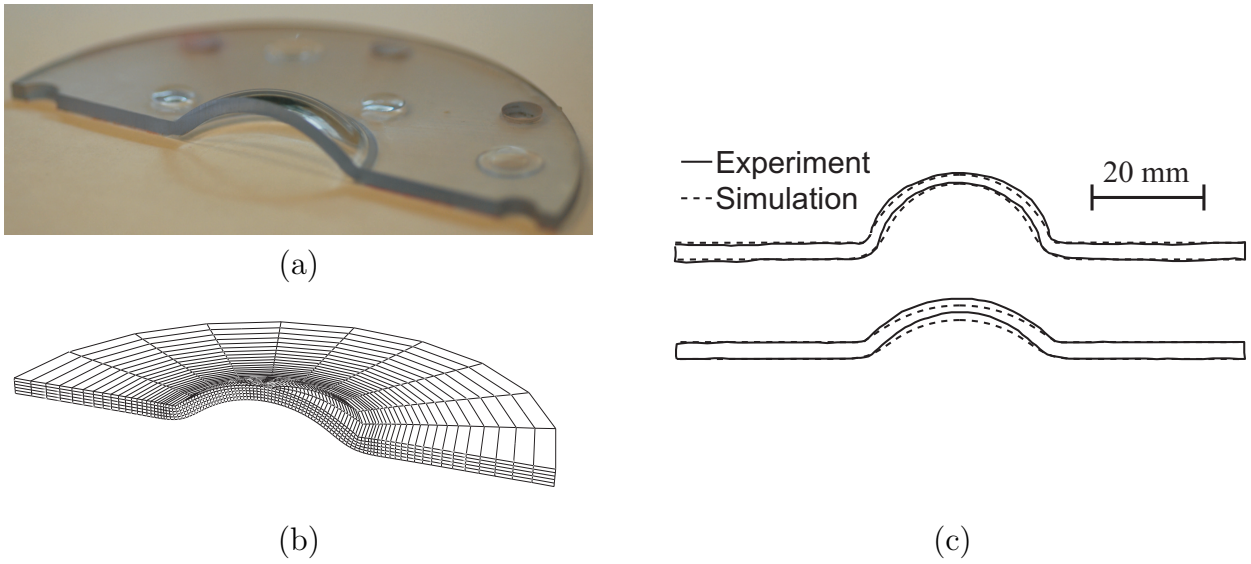

Figure 18: (a) One-half of final shape of the blow-formed PC plate at 155 C and 20 psi. (b) A three-dimensional representation of corresponding numerical prediction. (c) Comparison of the numerically-predicted profiles (dashed lines), against corresponding experimentally-measured traced surface profiles of the specimens (solid lines): the figure at the top is for blow-forming at 160 C and 35 psi (0.24 MPa), and that at the bottom is for blow-forming at 155 C and 20 psi (0.14 MPa).

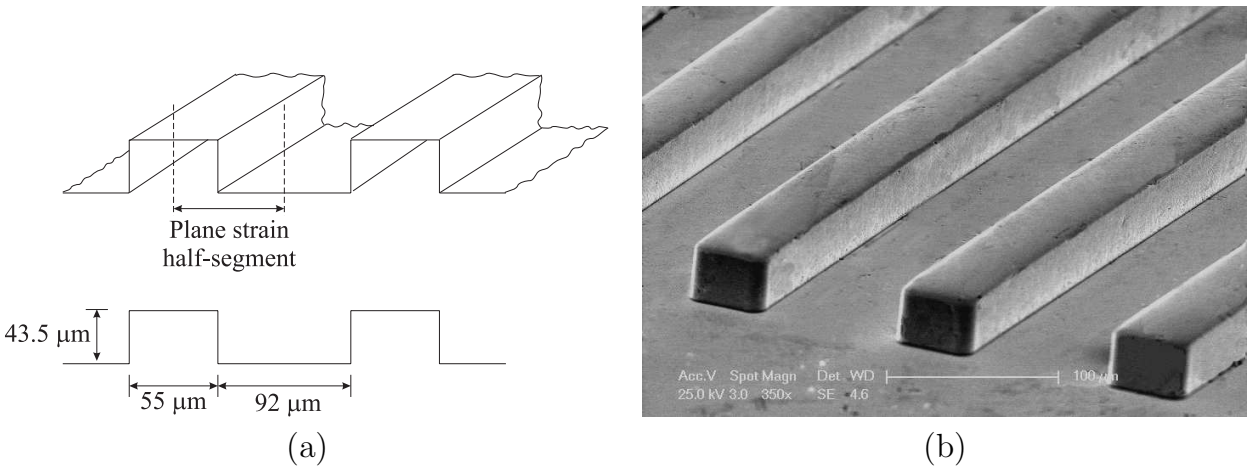

Figure 19: (a) Schematic of the plane-strain tool (not to scale), and (b) SEM micrograph of a portion of the metallic glass tool.

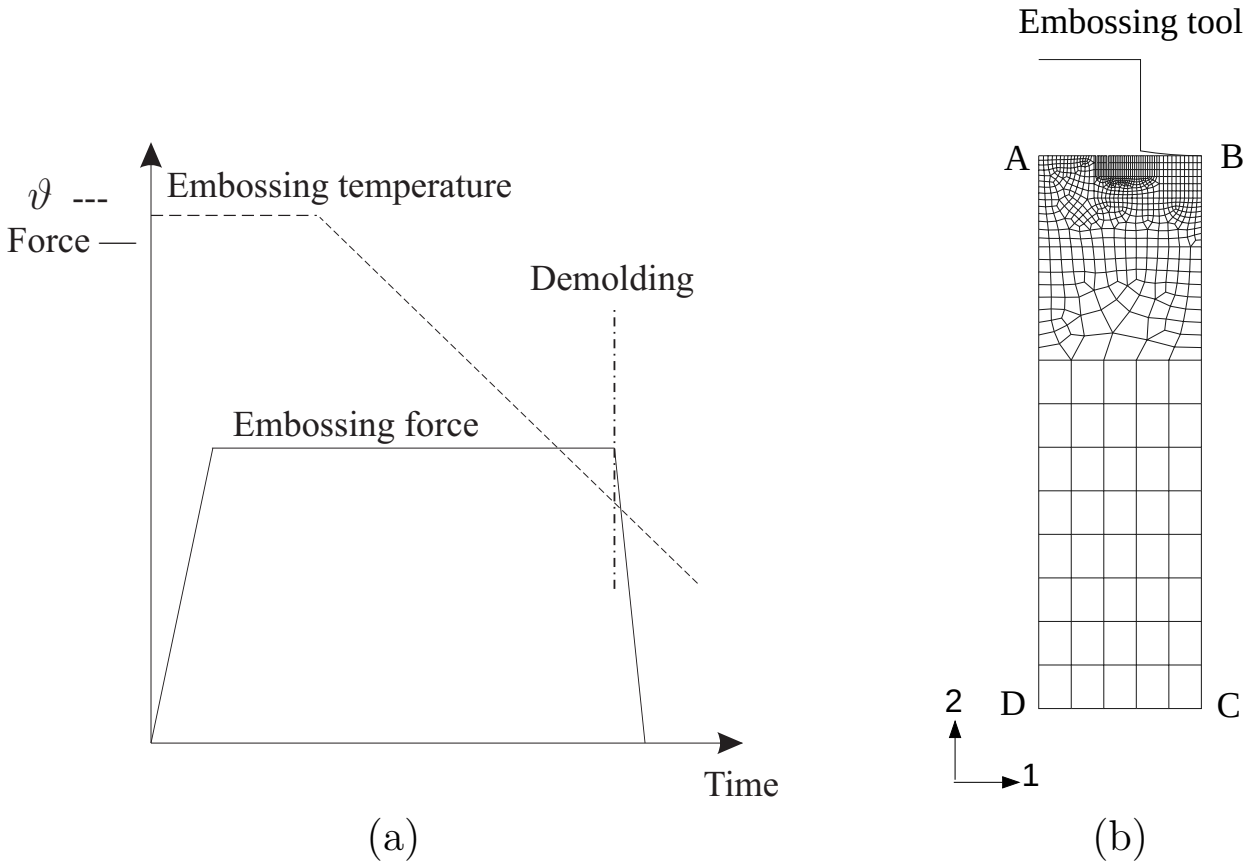

Figure 20: (a) Schematic of the processing conditions for the micro-hot-embossing, and (b) finite element mesh for the plane-strain simulation. The displacement boundary conditions on portions AD and BC of the mesh are u_1=0, while on portion CD, $u_1 = u_2 = 0$ are prescribed.

Figure 21: (a) SEM micrograph of the micro channels hot-embossed in Zeonex, and (b) the corresponding numerical prediction. The plane-strain simulation has been extruded and mirrored to make the comparison more clear.

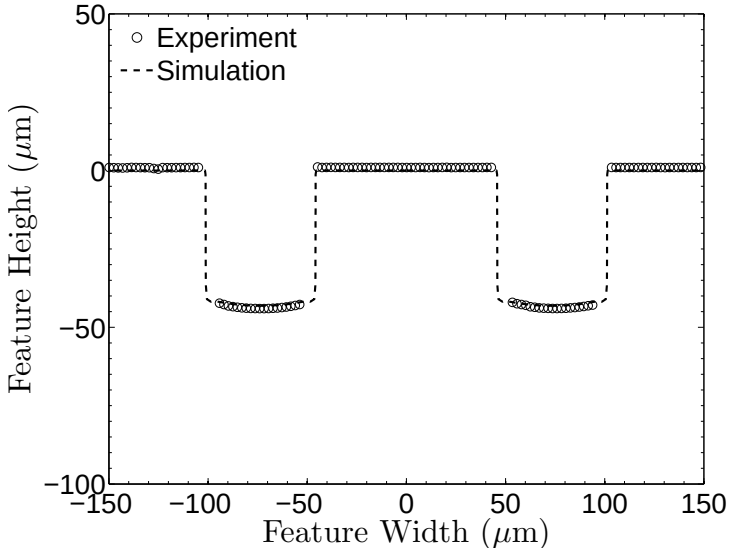

Figure 22: Comparison of the experimentally-measured (circles) and numerically-predicted channel profile (dashed line).

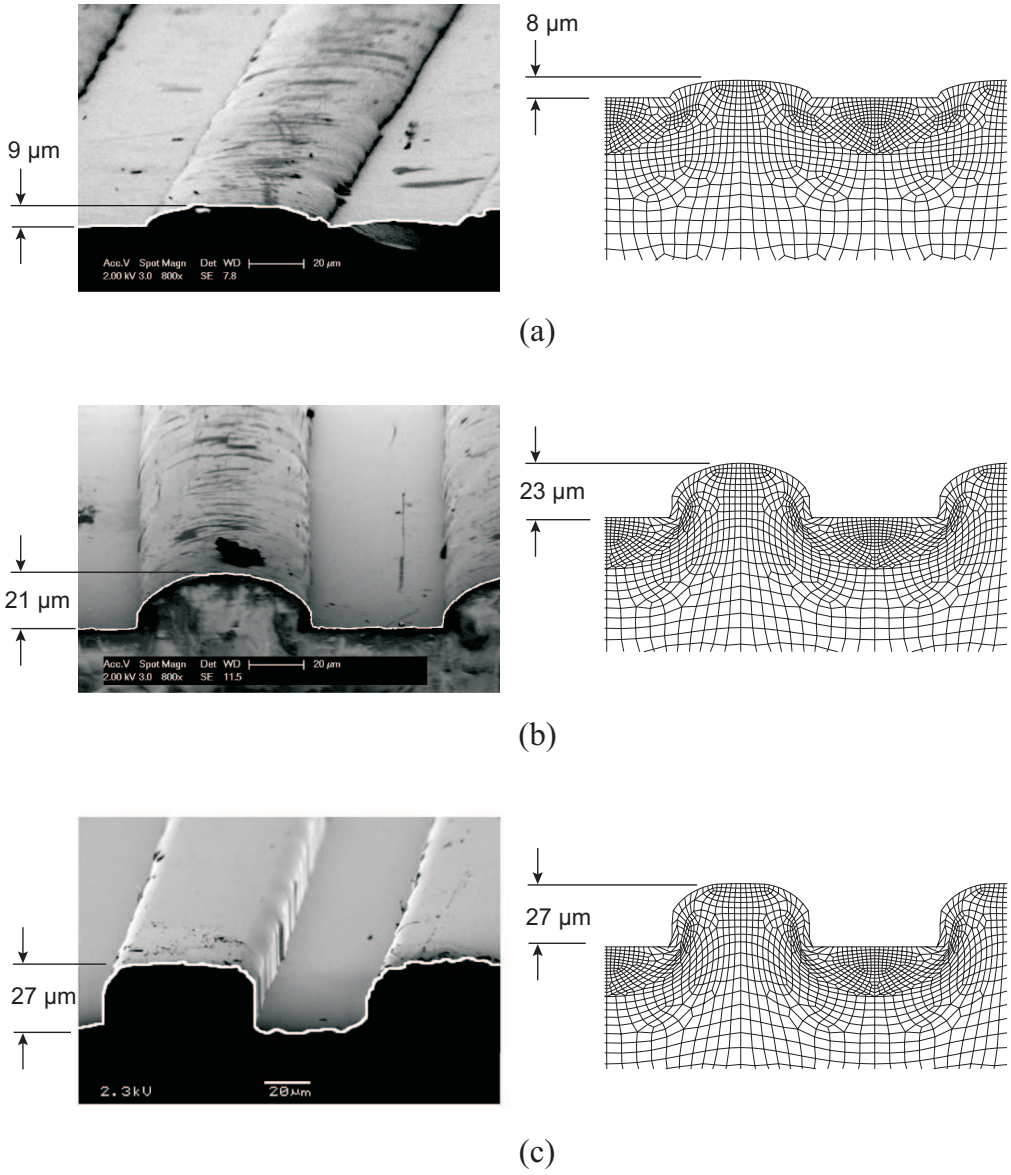

Figure 23: Comparisons of SEM micrographs from micro-hot-embossing experiments on PMMA against corresponding simulations at 130 C, under the following embossing pressures: (a) 0.48 MPa, (b) 1.12 MPa , and (c) 1.6 MPa.

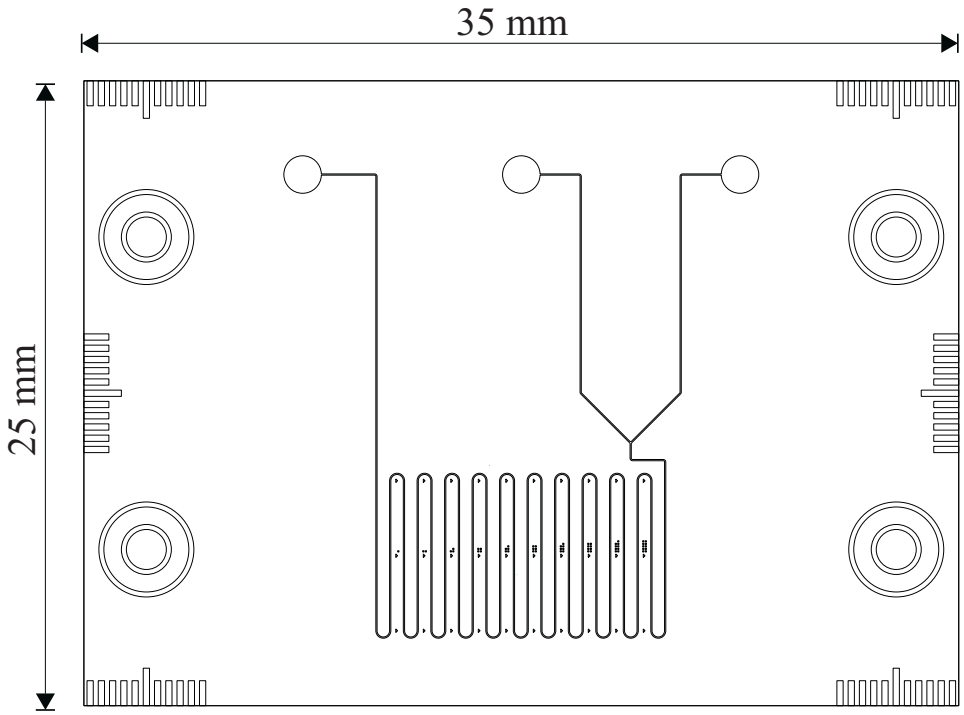

Figure 24: Geometry of the microfluidic mixer.

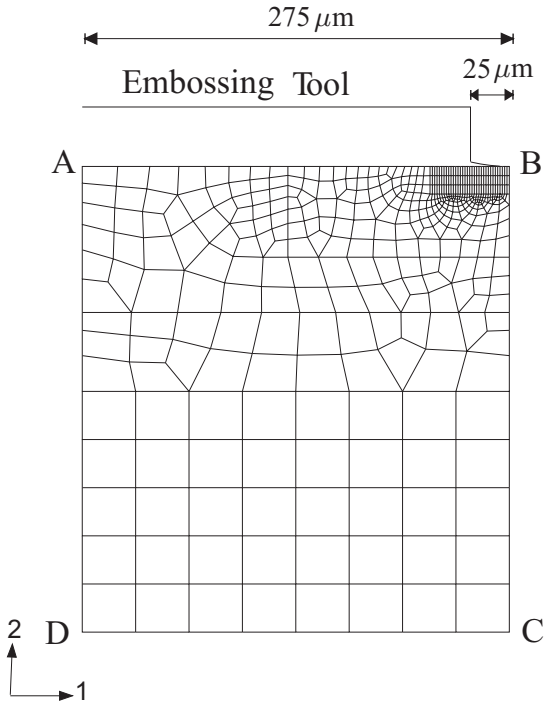

Figure 25: Finite element mesh for a plane-strain simulation showing the meshed substrate and the tool modeled as a rigid surface. The displacement boundary conditions on portions AD and BC of the mesh are $u_1 = 0$, while on portion CD $u_1 = u_2 = 0$ are prescribed.

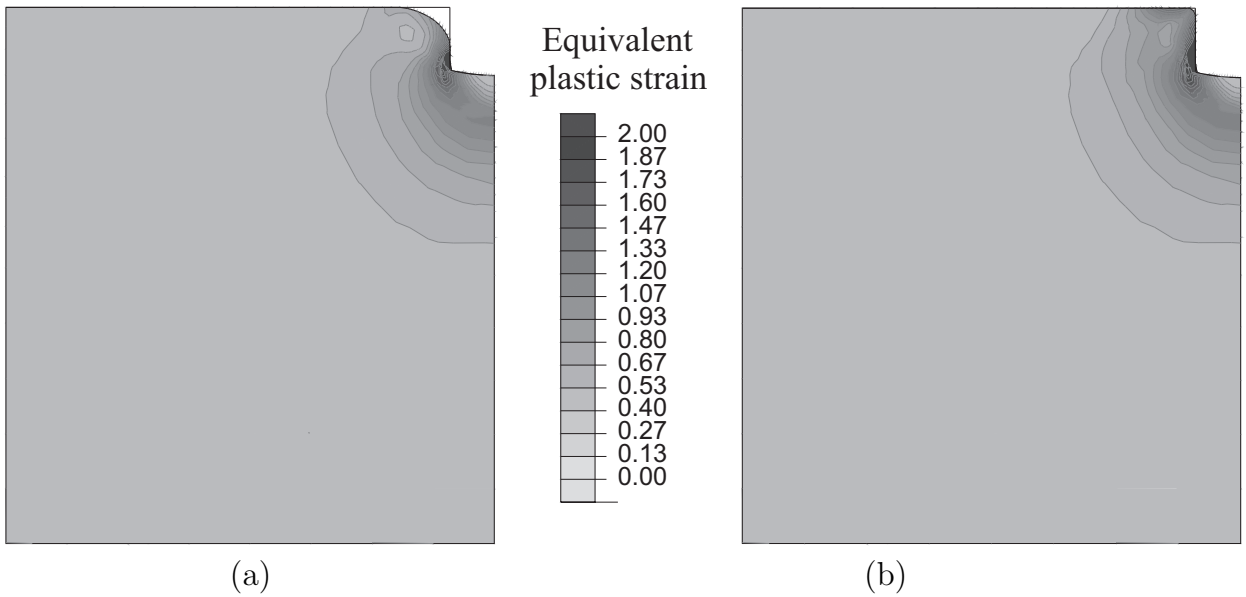

Figure 26: Zeonex deformation history during hot-embossing. (a) Partially-filled die at 10 s, and (b) filled die at 90 s.

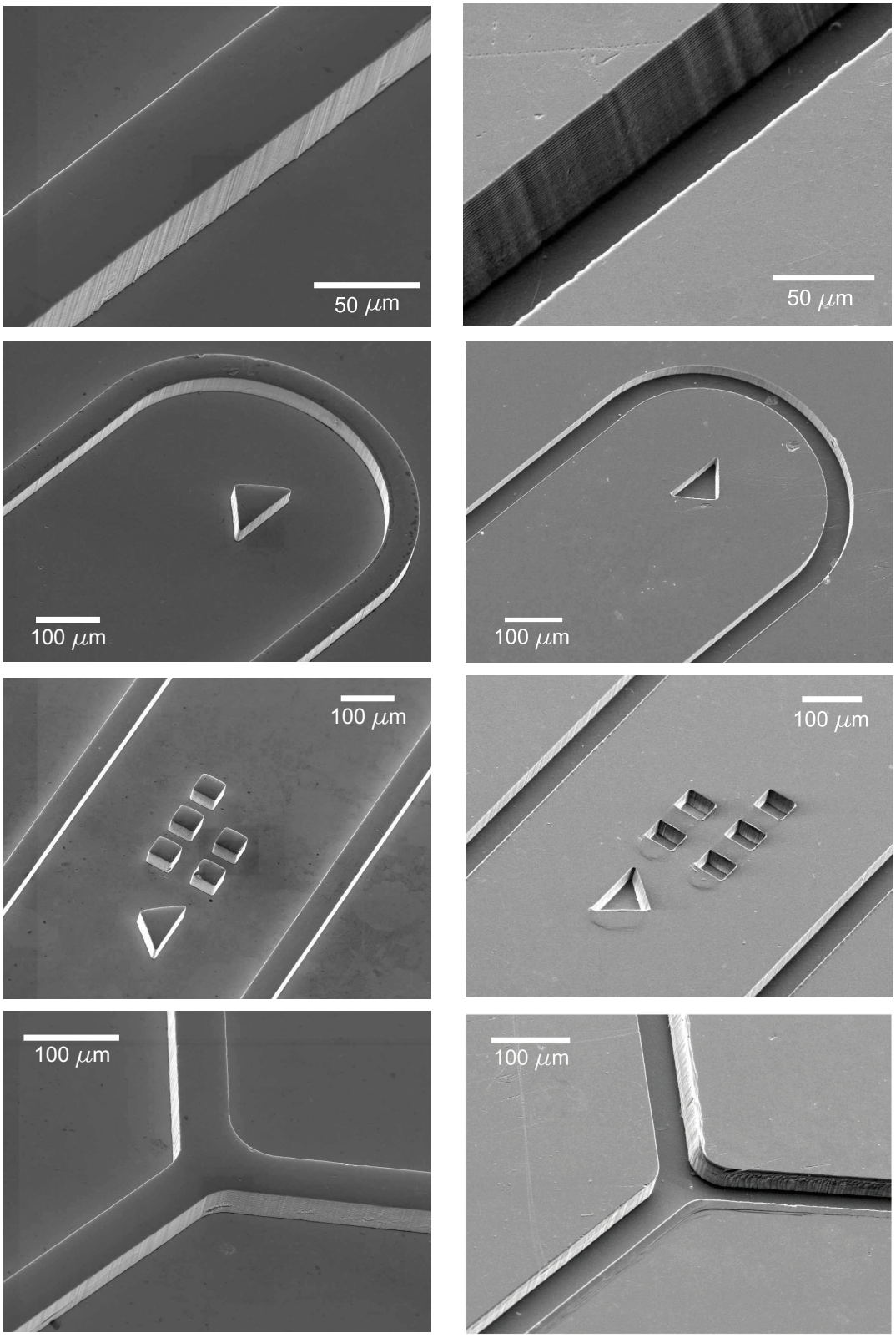

Figure 27: SEM micrographs of (a) features in bulk metallic glass tool, and (b) corresponding features in micro-hot-embossed Zeonex part.

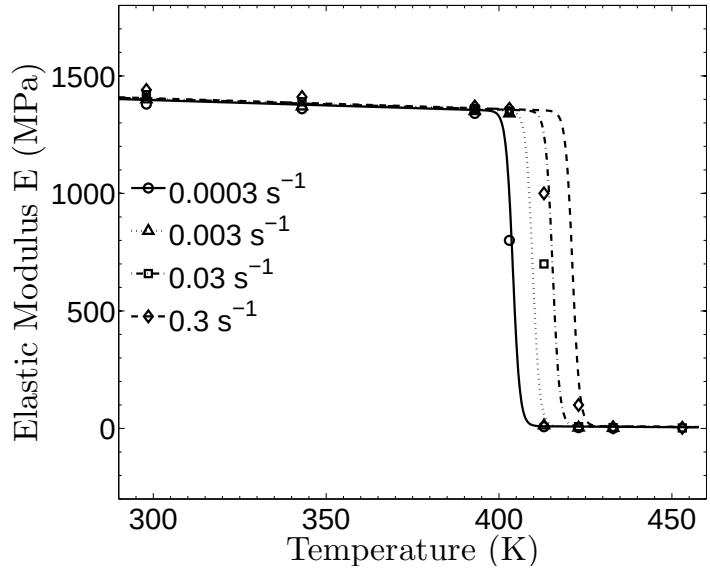

Figure 28: Fit of Elastic modulus E to phenomenological function (8.36).

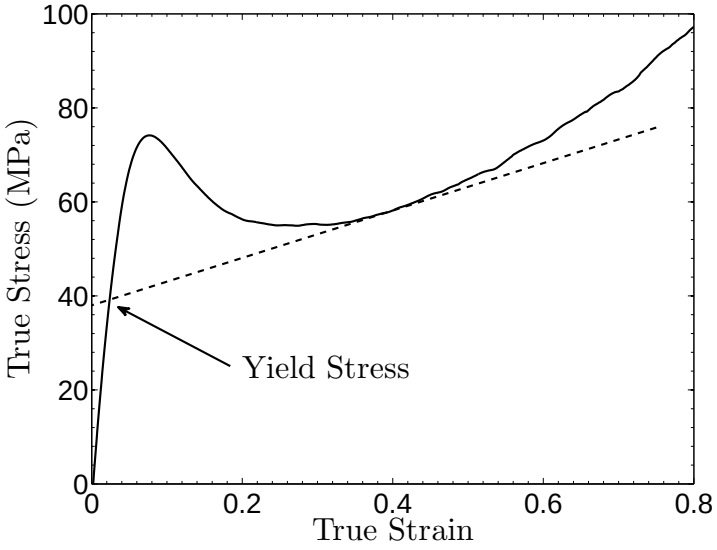

Figure 29: Schematic showing the "yield stress" defined as the intersection of the pre-peak stress-strain curve with the back-extrapolated tangent to the stress-stain curve at 0.4 strain.

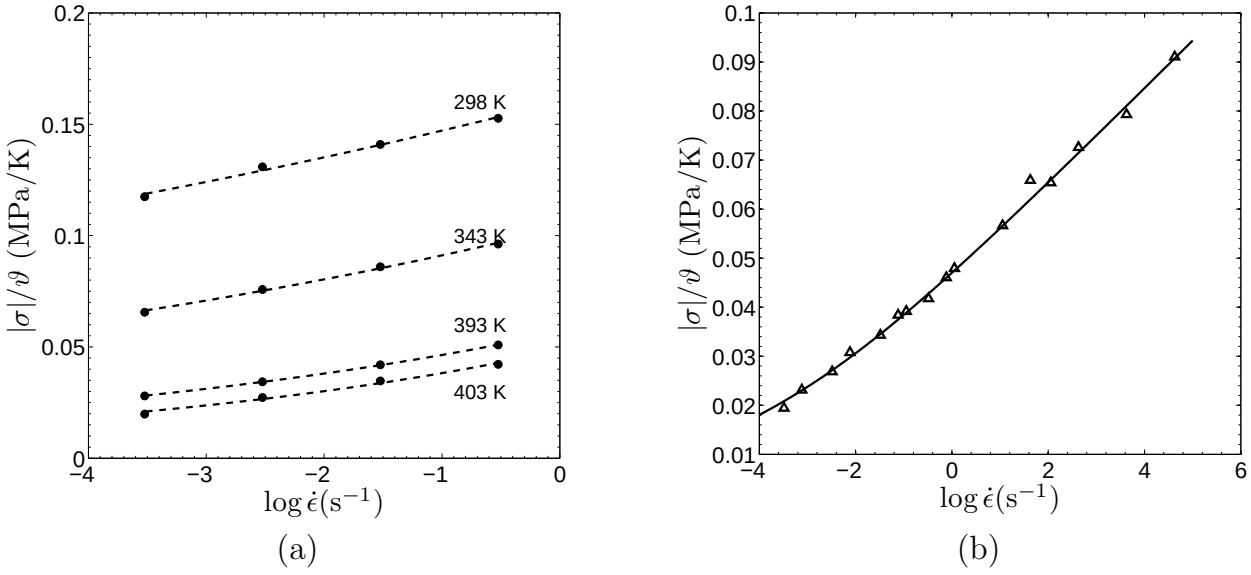

Figure 30: (a) Ratio of compressive yield stress to temperature as a function of logarithm of strain rate. The data plotted as bullets (•) are the yield stress values estimated from the compression experiments, and the dashed lines are estimated isotherms. (b) Master curve constructed at 404 K by shifting the yield stress data. The shifted experimental data is plotted as triangles (△), and the solid line indicates a fit of flow function to the master curve.

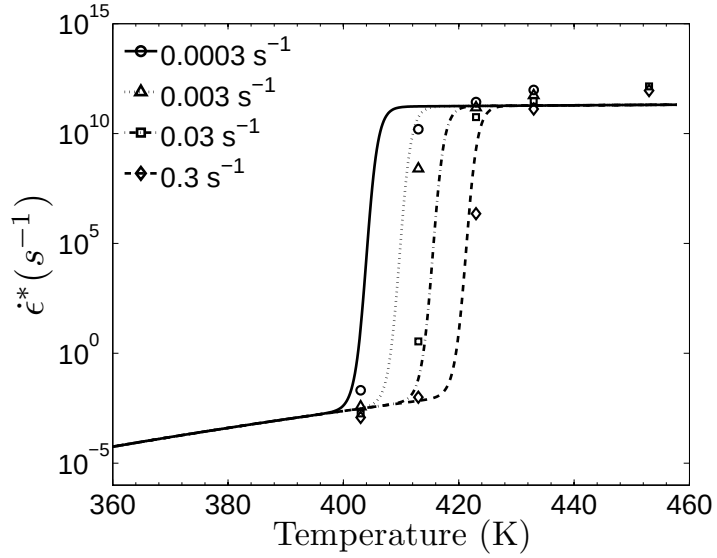

Figure 31: Fit of characteristic strain-rate $\dot{\epsilon}^*$ versus temperature above the glass transition temperature ϑ_g. Symbols indicate selected value for fitting and lines indicate fit of function given in (8.46).

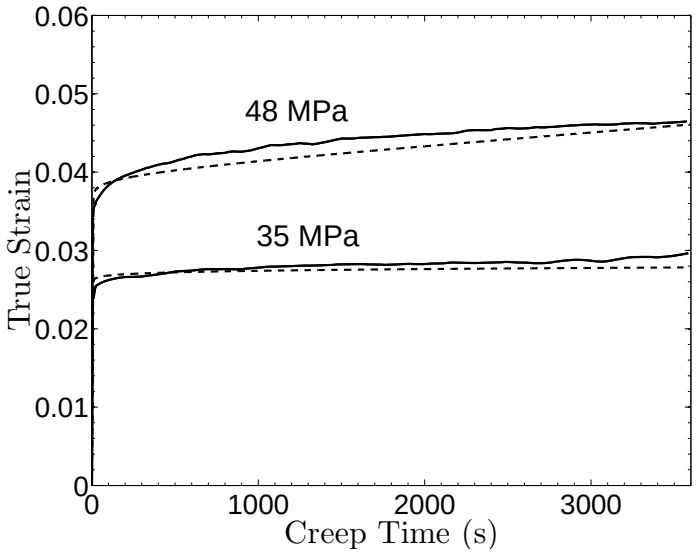

Figure 32: Creep test results under simple compression at two stress levels below the yield-peak (solid lines), together with one-dimensional MATLAB simulations (dashed lines).